UNIVERSIDADE DE LISBOA
FACULDADE DE CIÊNCIAS
DEPARTAMENTO DE FÍSICA

Early stages of star formation in the Rosette Nebula

Daniel Filipe Dias Capela

Mestrado Física
Especialização em Astrofísica e Cosmologia

Dissertação orientada por:
Koraljka Mužić

2024

Abstract

The Rosette Nebula is an emblematic star-forming region, hosting a rich population of young stars, including the ∼2 Myr old cluster NGC 2244 at its center, located at a distance of 1.5 kpc. We investigated the young stellar and substellar populations in the Rosette Nebula to reveal the different evolutionary stages of the young stellar object (YSO) population and map their spatial distribution. We used mid-infrared photometric data from the Infrared Array Camera onboard the Spitzer Space Telescope, complemented by optical and near-infrared data obtained from various instruments. YSO candidates are selected and classified based on colour-colour diagrams and spectral energy distribution fitting. We compiled a catalogue of YSO candidates with 2,576 sources, of which 1,972 are classified as Class II and 604 as Class I. The catalogue also includes 397 sources bellow the hydrogen-burning limit, for an age of 2 Myrs. We examined the distribution of YSOs in different evolutionary stages within various stellar structures present in the complex and reconstructed the star formation history of the Rosette Nebula. While some stellar groups show evidence of star formation triggered by the HII front created by the OB population in the NGC 2244 cluster, the presence of a YSO population beyond the interface region indicates that star formation in the Rosette Nebula occurs independently of NGC 2244 and its expanding HII bubble. Additionally, our age estimates for the stellar groups reveal variations that do not correlate with their positions within the Rosette Molecular Cloud or their distances from NGC 2244, indicating a dynamic evolution of the entire cloud.

Keywords: Stars: pre-main sequence – Stars: formation – Infrared: stars – ISM: individual objects: Rosette molecular cloud

Resumo

A Nebulosa da Roseta é uma região emblemática de formação de estrelas, abrigando uma rica população de estrelas jovens, incluindo o aglomerado NGC 2244 com $\sim$2 milhões de anos no seu centro, e localizado a uma distância de 1.5 kpc. Investigámos as populações estelares e subestelares jovens na Nebulosa da Roseta para revelar os diferentes estágios evolutivos da população de objetos estelares jovens (OEJs) e mapear a sua distribuição espacial. Usámos dados fotométricos do infravermelho médio da Infrared Array Camera a bordo do Telescópio Espacial Spitzer, complementados por dados óticos e de infravermelho próximo obtidos de vários instrumentos. Os candidatos a OEJs são selecionados e classificados com base em diagramas cor-cor e ajuste de modelos da distribuição espetral de energia. Compilámos um catálogo de candidatos a OEJs com 2,576 fontes, das quais 1,972 são classificadas como Classe II e 604 como Classe I. O catálogo também inclui 397 emissões abaixo do limite de queima de hidrogénio, para uma idade de 2 milhões de anos. Examinámos a distribuição de OEJs em diferentes estágios evolutivos dentro de várias estruturas estelares presentes no complexo e reconstruímos o histórico da formação estelar da Nebulosa da Roseta. Enquanto alguns grupos estelares mostram evidências de formação estelar provocada pela frente de HII criada pela população OB do aglomerado NGC 2244, a presença de uma população de OEJs além da região de interface indica que a formação de estrelas na Nebulosa da Roseta ocorre independentemente do aglomerado NGC 2244 e da sua bolha HII em expansão. Além disso, as nossas estimativas de idade para os grupos estelares revelam variações que não se correlacionam com as suas posições dentro da Nuvem Molecular da Roseta ou com as suas distâncias a NGC 2244, indicando uma evolução dinâmica de toda a nuvem.

Palavras Chave: Estrelas: pré-sequência principal – Estrelas: formação – Infravermelho: estrelas – MI: objetos individuais: Nuvem Molecular da Roseta

Resumo Alargado

A Nebulosa da Roseta é uma região emblemática de formação estelar, localizada a aproximadamente 1.5 kpc da Terra (Mužić et al., 2019), e é o lar de uma rica população de estrelas jovens. No seu centro encontrasse o enxame estelar jovem NGC 2244, que compreende uma grande associação OB. Estas estrelas massivas emitem radiação ultravioleta intensa que ioniza o gás envolvente, criando uma região HII em expansão. NGC 2244, com aproximadamente 2 milhões de anos (Mužić et al., 2022), não é a única população estelar na Nebulosa da Roseta. Outros grupos estelares menores foram identificados em estudos anteriores (Phelps and Lada, 1997; Roman-Zuniga, 2006; Poulton et al., 2008; Cambrésy et al., 2013), contribuindo para a estrutura complexa desta região de formação estelar.

Investigámos as populações estelares jovens e, pela primeira vez em toda a região, as populações subestelares (anãs castanhas) na Nebulosa da Roseta. O nosso estudo teve como objetivo revelar os diferentes estágios evolutivos da população de objetos estelares jovens (OEJs), mapear a sua distribuição espacial e reconstruir o histórico de formação estelar na região. Para o conseguir, compilámos um catálogo fotométrico que abrange desde comprimentos de onda óticos até ao infravermelho médio. Os dados fotométricos do infravermelho médio vêm do instrumento IRAC a bordo do Telescópio Espacial Spitzer, servindo de fundação do nosso catálogo, pois o infravermelho médio é crucial para detetar o excesso de infravermelho característico dos OEJs. Através de redução de dados e fotometria aplicada a dados não processados do instrumento NEWFIRM, complementámos o catálogo de infravermelho médio existente. Adicionalmente, incorporámos dados fotométricos ópticos e infravermelho próximo do catálogo descrito no trabalho de Mužić et al. (2022) e de catálogos públicos como o UKIDSS, 2MASS e Pan-STARRS.

Os candidatos a OEJ foram selecionados através de dois métodos, denominados Tier 1 e Tier 2. A seleção Tier 1 depende exclusivamente das fontes detectadas em todas as quatro bandas de IRAC. Nesta abordagem, os candidatos a OEJ são selecionados e classificados com base em diagramas cor-cor descritos na *Fase 1* de classificação no trabalho de Gutermuth et al. (2009). Além disso, para as fontes aplicáveis, uma versão melhorada do critério de corte de QSO proposto por Bouy et al. (2009) foi aplicado.

O processo de seleção Tier 2 foi concebido para abordar o campo de visão limitado e a menor magnitude de completude das bandas IRAC3 e IRAC4. Este processo necessita de fontes com fotometria em H, J, K_S, IRAC1 e IRAC2. A primeira fase da seleção Tier 2 foi realizada utilizando restrições no espaço das cores, com base na posição de fontes classificadas em Tier 1. A seleção Tier 2 é assim influenciada pelos critérios da seleção Tier 1, e como não são usadas restrições em IRAC3 e IRAC4 existe um maior número de contaminantes, difíceis de separar dos OEJs genuínos em comprimentos de onda mais curtos. Os candidatos a OEJ Tier 2 fase 1 passam para uma segunda fase, onde utilizamos o VOSA (Bayo et al., 2008) para realizar ajustes de modelos da distribuição espetral de energia. Estes ajustes permitem a construção de um diagrama Hertzsprung-Russell (HR) e, consequentemente, a estimativa de idades. As fontes com menos de 10 milhões de anos e classificadas como Classe II foram retidas. Além disso, os

OEJs Tier 2 Classe I, que ocupam posições distintas nos diagramas cor-cor, também foram mantidos, independentemente da sua posição no diagrama HR. Após o processo de seleção Tier 1 e Tier 2, refinamos a nossa amostra de candidatos a OEJs ao remover aqueles que se encontravam alinhados com os picos de difração de estrelas brilhantes, pois estes podem influenciar as leituras fotométricas. Além disso, excluímos fontes identificadas noutros estudos como nós de emissão, apesar da nossa classificação inicial como potenciais OEJs.

Obtivemos 1,905 fontes da seleção Tier 1 e 671 da Tier 2, resultando num catálogo de 2,576 candidatos a OEJ. Destes, 1,972 são classificados como Classe II e 604 como Classe I. O catálogo inclui também 397 emissões abaixo do limite de queima de hidrogénio, assumindo uma idade de 2 milhões de anos. Há muito que os investigadores procuravam saber qual o mecanismo de formação de anãs castanhas. A identificação de objetos subestelares no nosso catálogo de candidatos a OEJs apoia a ideia de que as anãs castanhas podem formar-se através dos mesmos processos que as estrelas. Além disso, o nosso catálogo inclui 33 candidatos a OEJs Tier 1 Classe I com massas abaixo do limite de queima de hidrogénio. Isto oferece uma oportunidade para estudos futuros destes objetos na Nebulosa da Roseta, particularmente das fases Classe 0/I que permanecem pouco compreendidas (Morata et al., 2015; Barrado et al., 2018). Também é importante notar que a nossa cobertura de objetos de menor massa é incompleta, e esperamos que muitas mais anãs castanhas existam na região.

Identificámos candidatos a OEJs em todos os grupos estelares destacados por Phelps and Lada (1997); Roman-Zuniga (2006); Poulton et al. (2008); Cambrésy et al. (2013), estando a maioria localizada em NGC 2244 e no complexo PL 04, PL 05 e REFL 08. Comparando as nossas descobertas com as de Broos et al. (2013), que também utilizaram dados fotométricos no infravermelho médio de IRAC e dados fotométricos no infravermelho próximo de 2MASS e UKIDSS para identificar OEJs, recuperámos 457 dos 586 candidatos OEJs identificados, resultando numa elevada taxa de recuperação de 78%. Em contrapartida, outras pesquisas, como a de Cambrésy et al. (2013), que utilizou dados do infravermelho médio do WISE, que tem menor resolução espacial, levando a problemas em regiões de alta densidade de estrelas, onde emissões de múltiplas fontes se misturam ou fundem-se com emissões nebulares, que não são resolvidas pelo WISE, mas são resolvidas pelo IRAC. Apesar destas limitações, conseguimos recuperar 241 dos 508 candidatos a OEJs identificados por Cambrésy et al. (2013), resultando numa taxa de recuperação de 47%.

A população de estrelas OB em NGC 2244 impulsiona a expansão de uma região HII, que interage com regiões de nuvens moleculares próximas, desencadeando a formação estelar e levando à formação de populações de OEJs. O nosso catálogo inclui candidatos OEJs localizados nesta região de interface, incluindo grupos estelares como PL 01, PL 02 e PouC. Este fenómeno também foi observado noutros estudos, servindo de evidência para a formação estelar desencadeada, onde a compressão do gás pela frente expansiva HII leva à formação de aglomerados (Phelps and Lada, 1997; Poulton et al., 2008; Schneider et al., 2010; Cambrésy et al., 2013). No entanto, em regiões localizadas mais afastadas de NGC 2244, para além da região de interface, a formação estelar não pode ser totalmente explicada por estes efeitos desencadeadores. Em vez disso, a evolução dinâmica da nuvem desempenha um papel mais significativo, com influência mínima de NGC 2244 (Heyer et al., 2006; Román-Zúñiga and Lada, 2008; Poulton et al., 2008; Schneider et al., 2010; Cambrésy et al., 2013). Isto indica que embora NGC 2244 tenha provavelmente desencadeado a formação estelar em PL 01, PL 02 e PouC, outras áreas, para além da bolha HII, formaram-se independentemente da sua influência. Ao integrar o nosso catálogo de OEJs com os dados de Mužić et al. (2022), obtivemos os movimentos próprios dos candidatos a OEJs em relação a NGC 2244. Os resultados mostram que os OEJs em PL 01 e PL 02 estão a ser empurrados para fora pela frente HII em expansão, dando ainda mais apoio à hipótese de formação estelar desencadeada

na região de interface.

Analisámos a distribuição dos OEJs em diferentes fases evolutivas em várias grupos estelares e reconstruímos o histórico da formação estelar da Nebulosa da Roseta. Os grupos estelares mais antigos incluem NGC 2244 e outros que provavelmente se formaram na mesma época, como a parte este do complexo PL 04, PL 05 e REFL 08, juntamente com o PouD, NGC 2237, REFL 09 e REFL 10. As regiões mais jovens, algumas ainda com formação estelar, incluem áreas ocupadas por PL 03, PL 06, PL 07 e a parte oeste do complexo PL 04, PL 05 e REFL 08. A região de interface, contendo grupos estelares como o PL 01, PL 02 e PouC, encontram-se algures entre estes dois estágios. Estas descobertas são consistentes com os estudos de Heyer et al. (2006); Román-Zúñiga and Lada (2008); Poulton et al. (2008); Schneider et al. (2010); Cambrésy et al. (2013); Mužić et al. (2022).

Enquanto alguns grupos estelares mostram evidências de formação estelar provocada pela frente de HII criada pela população OB do aglomerado NGC 2244, a presença de uma população de OEJs além da região de interface indica que a formação de estrelas na Nebulosa da Roseta ocorre independentemente do aglomerado NGC 2244 e da sua bolha HII em expansão. Além disso, as nossas estimativas de idade para os grupos estelares revelam variações que não se correlacionam com as suas posições dentro da Nuvem Molecular da Roseta ou com as suas distâncias ao aglomerado NGC 2244, indicando uma evolução dinâmica de toda a nuvem.

Contents

List of Figures

List of Tables

Acronyms

2MASS - Two Micron All-Sky Survey
ADU - Analog-to-Digital Unit
AGN - Active Galactic Nucleus
AllWISE - All Wide-field Infrared Survey Explorer
APASS - AAVSO (American Association of Variable Star Observers) Photometric All-Sky Survey
au - astronomical unit
CDS - Correlated Double Sampling
CFH12K - Canada-France-Hawaii 12K Charge-Coupled Device Mosaic Camera
CFHT - Canada-France-Hawaii Telescope
CTIO - Cerro Tololo Inter-American Observatory
DECam - Dark Energy Camera
FITS - Flexible Image Transport System
FLAMINGOS - Florida Multi-object Imaging Near-infrared Grism Observational Spectrometer
FoV - Field of View
HAWK-I - High Acuity Wide-field K-band Imager
HR - Hertzsprung-Russell (diagram)
INT - Isaac Newton Telescope
IR - Infrared
IRAC - Infrared Array Camera
ISM - Interstellar Medium
KPNO - Kitt Peak National Observatory
MegaCam - A wide-field optical camera at the CFHT
MIR - Mid-Infrared
NEWFIRM - NOAO Extremely Wide-Field Infrared Imager
NGC - New General Catalogue (of Nebulae and Clusters of Stars)
NIR - Near-Infrared
NOIRLab - National Optical-Infrared Astronomy Research Laboratory
NTT - New Technology Telescope
PAH - Polycyclic Aromatic Hydrocarbon
Pan-STARRS - Panoramic Survey Telescope and Rapid Response System
PARSEC - PAdova and TRieste Stellar Evolution Code
PED - Photo-Emissive Defects
PMS - Pre-Main Sequence
PSF - Point Spread Function

QSO - Quasi-Stellar Object (Quasar)
r2r - reset-to-1st-read
SED - Spectral Energy Distribution
SofI - Son of ISAAC (IR Spectrometer and Array Camera)
SVO - Spanish Virtual Observatory
UKIDSS - UKIRT Infrared Deep Sky Survey
UKIRT - United Kingdom Infrared Telescope
VIMOS - VIsible Multi-Object Spectrograph
VLT - Very Large Telescope
VOSA - Virtual Observatory SED Analyzer
WCS - World Coordinate System
WFC - Wide Field Camera
WFCAM - Wide Field Camera for UKIRT
WISE - Wide-field Infrared Survey Explorer
WIRCam - Wide-field InfraRed Camera
YSO - Young Stellar Object
ZP - Zero Point

Chapter 1

Introduction

Star formation is a process in astrophysics capable of shaping the structure and evolution of galaxies, the synthesis of heavy elements in the Universe, allowing for the creation of planetary systems and even life. Stars can shine for billions of years but their formation takes only a few million years. Star formation takes place in the dense areas of the interstellar medium (ISM), identified as molecular clouds. These clouds are composed of molecular hydrogen and other interstellar dust and gas. They are characterized by high densities ranging from 10^2 to 10^6 H_2 molecules per cm³. Along with cold temperatures, with some reaching as cold as 10 K (York, 2003), exhibiting irregular, often filamentary structures with clumps and cores (Schulz, 2005). Clumps are larger formations within the clouds that typically give rise to stellar clusters, while cores are smaller, denser regions where individual stars or binary systems form.

The stability and fragmentation of molecular clouds are governed by a balance of gravity, thermal pressure, turbulence, and their magnetic and rotational properties. Star formation begins when these clouds gain sufficient mass or are influenced by external forces like supernova shock waves or galactic collisions. This leads to the hierarchical fragmentation and collapse of the cloud. These fragments, reaching stellar mass, get heated from gravitational potential energy, which they initially radiate away. As their density increases and they become more opaque, they radiate less efficiently, causing a temperature rise that impedes further fragmentation (Prialnik, 2000). Consequently, this leads to the formation of Young Stellar Objects (YSOs), which are stars in their early stages of evolution. Initially hidden within their natal material, YSOs eventually evolve and shed their envelopes, revealing new stars.

The collapse of molecular clouds give rise to new star clusters. As these clusters form in the densest regions of the cloud, a transformative phase for the cloud itself begins. The formation of stars leads to the ionization of parts of the cloud, causing the gas to evaporate and disperse. This occurs when the energetic radiation from new stars heats the surrounding gas, making it expand rapidly and flow outward in streams (Tenorio-Tagle, 1979). This process, along with stellar winds, significantly contributes to the dispersion of the cloud (Wilson and Johnston, 1994), effectively halting star formation. This limits the cloud to converting only about 2% of its mass into stars. This cycle of cloud formation and destruction continues as the dispersed gas cools and is collected into new clouds by gravitational instability, thereby sustaining the ongoing cycle of star formation. Stars in young star clusters have similar ages and possess nearly identical galactic orbits and initial velocities akin to the molecular cloud from which they were born.

Star clusters serve as the primary sources of both stellar and substellar objects in the Universe (Lada and Lada, 2003; Portegies Zwart et al., 2010). Within young star clusters, objects spanning at least four orders of magnitude in mass are born (Mužić et al., 2019), ranging from high-mass stars, many times the mass of our Sun, to those of lower mass, similar to the Sun itself, and extending to substellar objects like

brown dwarfs and planetary-mass objects.

In this thesis, we employ mid-infrared (MIR) photometric data from the Spitzer Space Telescope, complemented by optical and near-infrared (NIR) data obtained from various instruments. The unprecedented depth of our data provides an opportunity to explore the young stellar and substellar (brown dwarfs) populations in the Rosette Nebula. This study aims to reveal different evolutionary stages of the YSO population and map their spatial distribution within the nebula. The following introductory chapter of the thesis presents an in-depth examination of the fundamental concepts related to YSOs and brown dwarfs. It also offers a overview of the Rosette Nebula and its associated star clusters. Chapter 2 details the processes of data reduction and photometry applied to the retrieved raw data. Chapter 3 focuses on the compilation of a detailed dataset that encompasses photometric data ranging from optical to MIR wavelengths. Our dataset also integrates the photometric data compiled in Chapter 2. In Chapter 4, we explore various methods for identifying and classifying YSOs and delve deeper into the analysis of YSO candidates that are part of the substellar population. This effort aims to compile a catalogue of YSO candidates within the Rosette Nebula. In Chapter 5, we analyze the spatial distribution of various evolutionary stages of the YSO candidates within the nebula. These distribution might be indicative of age, with a higher proportion of sources in earlier evolutionary stages suggesting a lower age in that particular region. Our study aims to provide insights into the age distribution across the Nebula and identify new YSO candidates that are part of the substellar population. Finally, the thesis concludes with a summary presented in Chapter 6, encapsulating the findings and contributions of this research.

1.1 Young Stellar Objects (YSOs)

Regions within molecular clouds undergo collapse, leading to the formation of YSOs. These YSOs are classified into different classes based on their evolutionary stage. Studying YSOs within stellar clusters is a prevalent method for analyzing star forming regions. The existence of YSOs signifies ongoing star formation, and their arrangement in a molecular complex sheds light on the region's star formation chronology (Gutermuth et al., 2011). Identifying YSOs typically involves categorizing them, a process that helps differentiate between the stages of evolution from star formation to the main sequence. This classification offers deeper insights into the structure and evolution of star-forming regions.

The different phases of star formation, along with their respective time scales and sizes, are illustrated in Figure 1.1. This figure also provides a glimpse of the physical processes occurring at each stage of a star's evolution. The process of star formation commences with a molecular cloud clump (Figure 1.1 *a*), the precursor of a star cluster, at time zero, marking the beginning of the star's lifecycle. On average, clumps measure about 1 pc (around 200,000 au) across. As the cloud collapses, it transitions into the Class 0 phase (Figure 1.1 *b*). YSOs in Class 0 are the youngest, still in the process of accumulating mass from their surrounding envelopes. These sources are deeply enshrouded in dust and gas, rendering them observable primarily in submillimeter and radio wavelengths (Figure 1.2). This phase is characterized by sources that are typically aged between 10,000 to 100,000 years, within which the structure is about 10,000 au in size.

In about 100,000 years, the YSO evolves into the Class I stage (Figure 1.1 *c*), shrinking to approximately 1,000 au. YSOs in the Class I stage consist of one or more optically thick stellar cores, called protostars, which are surrounded by an accretion disk and an infalling, dense envelope. Its emission spectrum is noticebly shifted towards the infrared (IR) wavelengths (Figure 1.2).

Subsequently, the YSO reaches the Class II stage (Figure 1.1 *d*), characterized by a reduction in surrounding material and the presence of a protoplanetary disk. This stage is critical for the observation

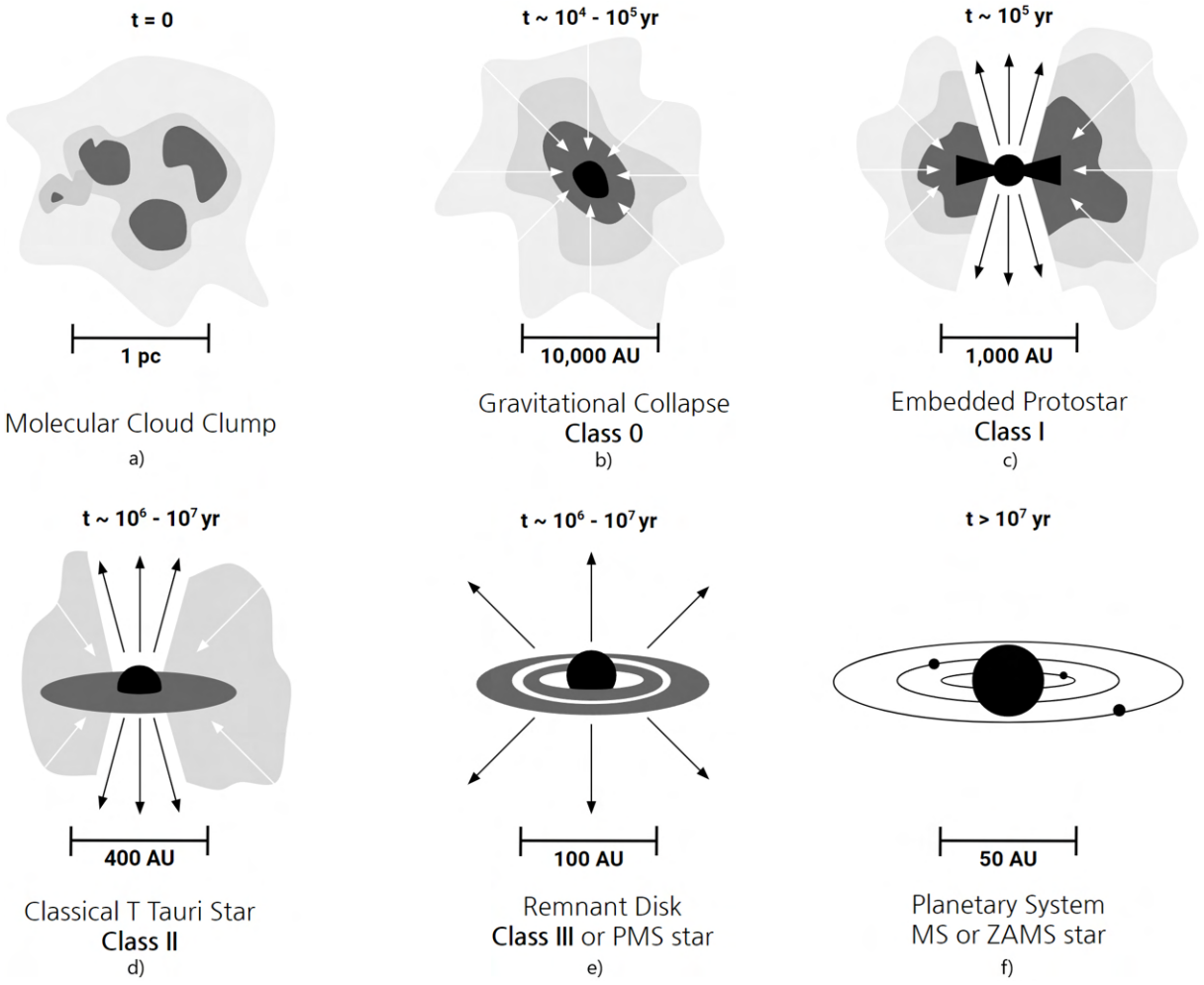

Figure 1.1: Schematic depicting the birth of a star from its earliest phase to maturity. At stage *a)*, a molecular cloud clump hints at a future star cluster. By stage *b)*, gravitational forces have triggered collapse into a dense core. Stage *c)* reveals a protostar accreting mass from the surrounding dense envelope, exhibiting outflows. Stage *d)* shows the protostar accumulating mass, its surrounding envelope thinning, with a visible protoplanetary disk and outflow activity. In stage *e)*, the PMS star has a disk where planets coalesce. Finally, stage *f)* portrays a main sequence star, orbited by a developed planetary system.

of disk formation and beginning of the planetesimal accretion processes. In this stage the spectral range expands to include both optical and infrared wavelengths (Figure 1.2). This lasts from about 1 million to 10 million years and the surrounding disk measures around 400 au.

Upon reaching around 10 million years in age, the YSO enters the most evolved phase, Class III (Figure 1.1 *e*), where the system's size is about 100 au. A Class III YSO has accreted most of its natal circumstellar material, concluding the protostellar phase. It is in this phase that planet formation predominantly occurs. Then, the Class III YSOs becomes easily visible throughout the optical (Figure 1.2) and are often considered as pre-main-sequence (PMS) stars, which is a premature star contracting towards the main sequence (Schulz, 2005).

With an age surpassing 10 million years, the YSO Class III will reach the main sequence. Often characterized by the presence of a planetary system much like our own Solar System (Figure 1.1 *f*). At this stage, the star commences sustained nuclear fusion of hydrogen at its core, initiating its lifecycle in the galaxy.

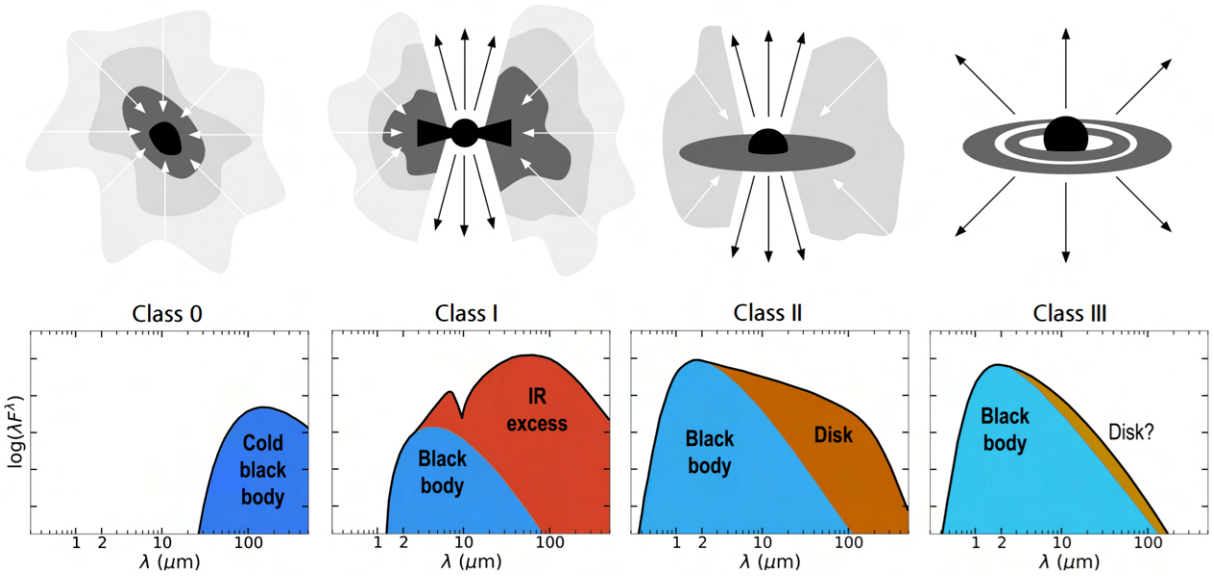

Figure 1.2: The top half of the figure presents a schematic diagram for each class of YSOs, showing the evolution from class 0 to III. The bottom half displays the corresponding SEDs. Adopted from Dauphas and Chaussidon (2011).

The spectral energy distribution (SED) is a representation of the energy output of an astronomical object as a function of frequency or wavelength. It is a fundamental tool in astrophysics for inferring the physical properties of stars, galaxies, and other celestial bodies, by analyzing the distribution and intensity of their electromagnetic radiation across the spectrum.

For Class 0, the SED illustrates a cold black body curve. Progressing to Class I, the SED shows both a black body and an infrared excess, indicative of a heated envelope surrounding the forming protostar. In Class II, the SED features a warmer black body spectrum from the central star and a distinct contribution from the circumstellar disk. By Class III, where planet formation is underway, there may be a slight emission feature from any remaining disk material, debris, or newly formed planets around the central star.

1.2 Brown dwarfs

Brown dwarfs are intriguing celestial bodies that straddle the line between the heaviest gas giant planets and the lightest stars. Often described as failed stars or substellar objects, these bodies have masses bellow 0.075 $M_{\odot}$. This mass represents a key boundary in stellar physics. Objects with more than 0.075 $M_{\odot}$ can sustain hydrogen fusion, thereby are true stars. Brown dwarfs, on the other hand, are defined by their inability to sustain hydrogen fusion in their cores, mainly due to their limited mass. As a result, brown dwarfs never reach the main sequence. As they age, their temperature and luminosity steadily decrease. These bodies emit most of their energy in the infrared spectrum, with temperatures that can range from a few hundred to a few thousand K, depending on their age, mass, and chemical composition (Reid, 2005).

As mentioned in the previous section, the formation of stars results from the gravitational collapse and hierarchical fragmentation of molecular clouds. While this mechanism can theoretically also form brown dwarfs, the challenge lies in achieving the necessary high density for substellar mass fragments to collapse. The required density for a substellar mass fragment to undergo gravitational collapse is significantly higher than the density measured in high-density star-forming regions (Stamer and Inutsuka,

2019).

Planets, on the other hand, form in protoplanetary disks through core accretion or the gravitational collapse of a disk fragment (Drążkowska et al., 2023). The mass range for star-like and planet-like formation overlaps, complicating the identification of substellar objects based on mass alone. Consequently, several processes have been proposed for the formation of brown dwarfs.

One theory suggests that brown dwarfs form in the same way as stars, with turbulence in a molecular cloud leading to the compression and fragmentation of gas (Padoan and Nordlund, 2002, 2004; Hennebelle and Chabrier, 2008; Elmegreen, 2011). In this process, the mass of each core ultimately determines the mass of the resulting stellar or substellar object (Lomax et al., 2016). Another mechanism is based on star-like formation but involves ejection from a stellar embryo. Here, interactions within a massive core can eject some objects, halting their accretion prematurely (Reipurth and Clarke, 2001; Goodwin et al., 2004; Bate, 2009). A third method involves planet-like formation, where fragmentation of massive circumstellar disks around stars results in substellar companions that may be ejected through interactions (Stamatellos and Whitworth, 2009; Kratter et al., 2010; Basu and Vorobyov, 2012; Vorobyov, 2013). Lastly, photo-erosion by radiation from OB stars can prevent accretion by stripping the envelope and disk of low-mass protostars. However, this is an inefficient method and is unlikely to be the dominant mechanism, especially in regions without OB stars (Hester et al., 1996; Whitworth and Zinnecker, 2004).

One way to confirm if brown dwarfs can form like stars is by searching for a substellar population of YSOs. Finding brown dwarf-mass objects that exhibit similar behavior would support the theory that brown dwarfs can share a formation channel with stars. Furthermore, like stars, most brown dwarfs are born in clusters and associations, making these environments ideal laboratories for studying the formation of both stars and brown dwarfs.

1.3 Rosette Nebula

The Rosette Nebula, also known as Caldwell 49, is a massive cloud of gas and dust that forms a vibrant and mesmerizing region of star formation in the constellation Monoceros. As part of the larger Monoceros complex, the nebula is noted for its intricate rosette-like structure, framed by dark filaments and surrounded by a radiant halo of ionized hydrogen, which creates a characteristic H II region (Figure 1.3).

Situated about 1,500 pc from Earth (Ogura and Ishida, 1981; Perez et al., 1987; Hensberge et al., 2000; Martins et al., 2012; Park and Sung, 2002; Lombardi et al., 2011; Kharchenko et al., 2013; Bell et al., 2013; Kuhn et al., 2019; Mužić et al., 2019; Lim et al., 2021), the Rosette Nebula spans an impressive diameter of approximately 40 pc, making it one of the larger emission nebulae visible from Earth. At its core lies the star cluster NGC 2244, also known as Caldwell 50. This young star cluster comprises a large OB association. These stars emit intense ultraviolet radiation, causing the surrounding hydrogen gas to ionize and create the distinctive pinkish-red glow associated with emission nebulae. Their ionization process leads to a bright expanding HII region that influences nearby molecular clouds through photoevaporation and photoionization. Morover, this powerful ionization front created by the winds of the OB associantion is evacuating the center of its original cloud.

The star cluster NGC 2244 is estimated to be around 2 Myrs old (Perez et al., 1987; Lim et al., 2021; Mužić et al., 2022). Besides this central cluster, the Rosette Nebula also hosts other young star clusters and groups previously identified in the studies by Phelps and Lada (1997); Roman-Zuniga (2006); Poulton et al. (2008); Cambrésy et al. (2013). These studies also suggest that areas near the molecular cloud of the Rosette Nebula are younger than those in the central region, occupied by the cluster NGC 2244.

After a century of research, the Rosette Nebula region is recognized as one of the most important sites

Figure 1.3: The Rosette Nebula in the constellation of Monoceros, with a field of view of 2.6 by 2 square degrees. Credit: John Corban & the ESA/ESO/NASA Photoshop FITS Liberator.

for studying star formation. The region has been forming stars for the past few Myrs and is expected to continue, given the dynamic environment of the molecular material. The OB association of NGC 2244 has created a large photodissociation region that interacts with the nearby molecular cloud, revealing a rich embedded star population. Additionally, young, low-mass stars might be forming around the central cavity, possibly indicating triggered star formation. The interaction between the nebula and the molecular cloud has significantly influenced the formation of embedded clusters and associations, though the full extent of this interaction remains unclear. The star formation activities in the Rosette Molecular Cloud may be linked to both its early evolution and the current interaction with the HII region (Román-Zúñiga and Lada, 2008).

The nebula's abundant YSOs make it an excellent target for astronomers studying the early stages of star formation and the conditions that lead to new stars and stellar systems. Studies have been conducted to uncover both the stellar (Mužić et al., 2022; Kuhn et al., 2015, 2014) and substellar (Almendros-Abad et al., 2023; Mužić et al., 2019) populations of the Rosette Nebula. Research has also utilized excess emissions in the infrared to identify young stars (Cambrésy et al., 2013; Poulton et al., 2008; Balog et al., 2007). In this thesis, we will identify the YSO population using infrared excess, encompassing both the stellar and, for the first time, the substellar (brown dwarf) populations. This analysis will also be used to draw conclusions that help determine the relative ages of these populations and reconstruct the star formation history in the region.

Chapter 2

Data Reduction and Photometry

This thesis centers on the examination of data gathered in the Rosette Nebula region, employing a variety of instruments and telescopes. The culmination of these efforts resulted in the construction of a dataset, as outlined in Chapter 3. However, additional data coverage was needed for the southeast area of the Rosette Nebula. This region contains important known groups of stars (Phelps and Lada, 1997), but it lies farther from the star cluster NGC 2244 and, therefore, is not as well covered by the main Optical-NIR catalogue (Mužić et al., 2022). To address this, we performed data reduction and photometry on retrieved data from this region of the sky.

2.1 Retrived dataset

We retrieved all the images obtained with the NOAO Extremely Wide-Field InfraRed Mosaic (NEWFIRM; Autry et al., 2003; Probst et al., 2004, 2008) from the National Optical-Infrared Astronomy Research Laboratory (NOIRLab) Astro Data Archive[1], within a radius of 2° centered on NGC 2244, as summarized in the Table 2.1. It is essential to acknowledge that, despite being referred to as KX_S, HX, and JX, these filters correspond almost identically to the K_S, H, and J filters and will be referred to as such.

Table 2.1: Retrieved data from the NOIRLab Astro Data Archive, employing the NEWFIRM instrument.

Observatory	*Cerro Tololo*	*Kitt Peak*		
Telescope	*Blanco*	*Mayall*		
Program Number	2011A-0567	2012B-0439		
Observation Date	18/03/2011	29/01/2013		
Instrument Filter	K_S	KX_S	***HX***	***JX***
No. Science Images	12	24	24	20
Exposure time per frame (s)	20	20	20	25
No. Flat Frames (On/Off)	11/11	10/10	10/10	10/10
Exposure time per frame (s)	2	2	5	10
No. Dark Frames	12	20		20
Exposure time per frame (s)	20	20		25

The data spans three distinct sky regions, labeled F1, F2, and F3 as shown in Figure 2.1. Notably, there is a slight overlap in F1 and F2. The F1 field is covered solely by the K_S filter at Cerro Tololo Inter-

[1] https://astroarchive.noirlab.edu/

American Observatory (CTIO), with program number 2011A-0567 (PI: Elizabeth Lada)[2]. The fields F2 and F3 are covered by J, H, and K_S filters at Kitt Peak National Observatory (KPNO), with program number 2012B-0439 (PI: Charles Lada)[3]. All accompanied by corresponding calibration frames: flat and dark frames. The details regarding Fields F1, F2, and F3, including their central coordinates, are presented in Table 2.2.

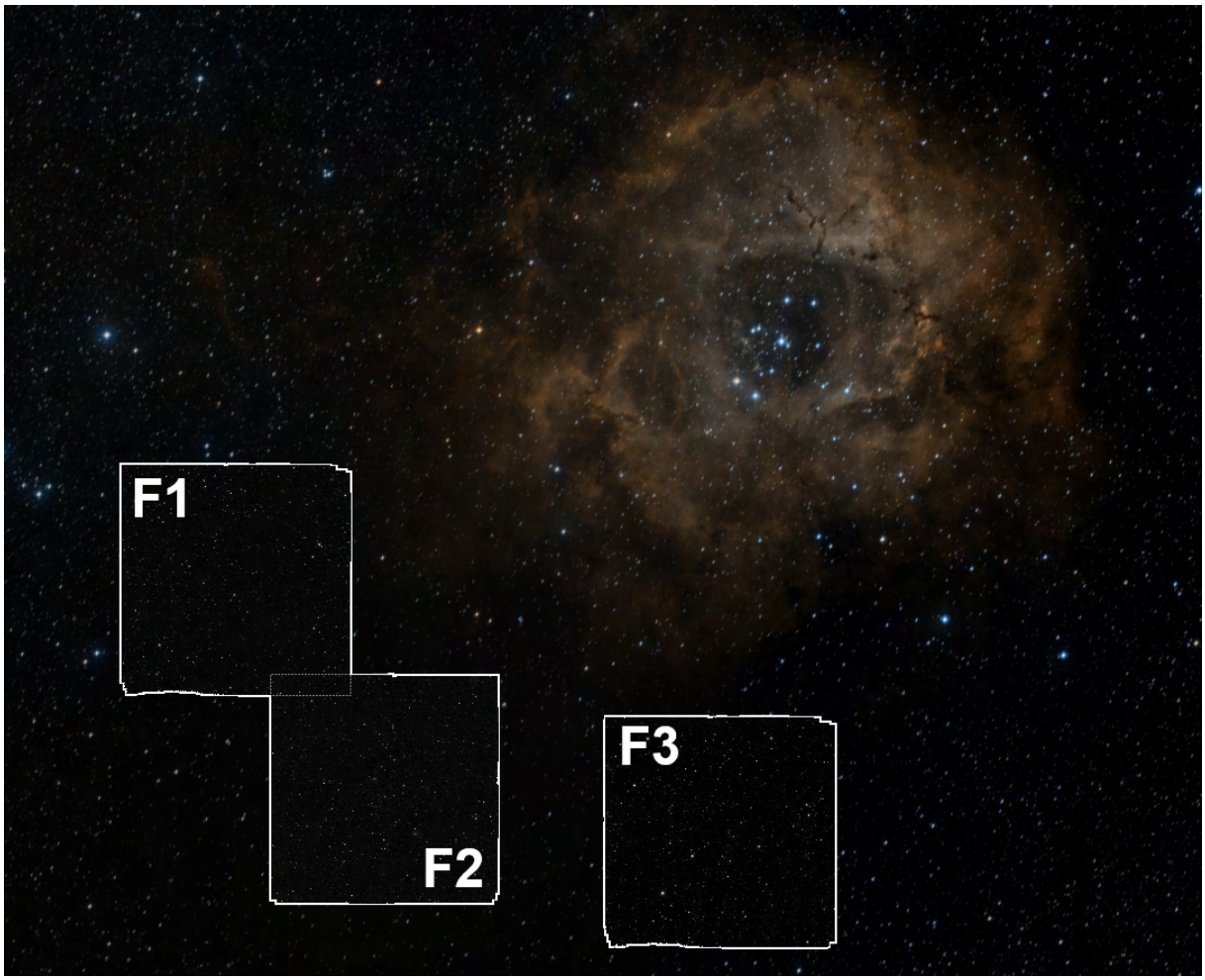

Figure 2.1: This image presents the three mosaics generated through the data reduction process using the K_S filter, revealing an overlap between F1 and F2. The background image, sourced from the Digital Sky Survey, distinctly displays the central structure of the Rosette Nebula, with a field of view of 2.6 by 2.1 square degrees.

Table 2.2: Fields observed by NEWFIRM.

Program Number	$(\alpha, \delta)(J2000)$	**Field Name**	**Filters**
2011A-0567	$(06^h35^m22^s, +03°58'34'')$	F1	K_S
2012B-0439	$(06^h32^m26^s, +03°51'22'')$	F2	J, H, K_S
	$(06^h36^m44^s, +04°25'13'')$	F3	J, H, K_S

[2] https://time-allocation.noirlab.edu/#/proposal/details/2011A-0567
[3] https://time-allocation.noirlab.edu/#/proposal/details/2012B-0439

2.2 Instrument Overview

The NOAO Extremely Wide-Field InfraRed Mosaic (NEWFIRM; Autry et al., 2003; Probst et al., 2004, 2008) is an instrument renowned for its exceptional infrared sensitivity and an exceptionally wide field of view (FoV), designed for operation at the Cassegrain focus of the NOAO 4-meter telescopes. Although this instrument has been used at both the Mayall Telescope at KPNO and the Blanco Telescope at CTIO (Figure 2.2) in alternating campaigns, it is currently located at CTIO.

Figure 2.2: Cerro Tololo Inter-American Observatory (CTIO) is positioned approximately 500 km north of Santiago, Chile, at an altitude of 2200 meters. Credit: https://noirlab.edu/public/programs/ctio/

The NEWFIRM features a focal plane comprised of a 2×2 mosaic of 2048×2048 Orion InSb array detectors, and the gaps separating the detectors are approximately $35''$. The detector covers a wavelength range of 1 to 2.4 μm at 0.4 arcseconds per pixel. The net FoV encompasses an area of nearly $28' \times 28'$ (Table 2.3), almost the size of the full moon.

The NEWFIRM camera includes two filter wheels capable of accommodating various filters [4], such as the J-, H-, and K_S-bands. Additionally, NEWFIRM operates without a mechanical shutter. Instead, the exposure duration is controlled by the variance between the initial and final nondestructive reads of the array (Shaw, 2015). This characteristic bears significant consequences for linearity and measured counts, as elaborated in Section 2.3.2.

Table 2.3: NEWFIRM camera characteristics (Shaw, 2015).

Field of view	$28' \times 28'$
Pixel scale of FPA	$0.40''$/pixel
Inter-array gaps	$35''$, or 88 pixels
Delivered image quality	$0.8''$ in excellent seeing conditions

2.3 Data reduction

Before performing photometry, the raw data obtained from observations undergoes a process known as data reduction, during which various instrumental effects are corrected. In the case of NEWFIRM

[4] https://noirlab.edu/science/programs/ctio/instruments/newfirm/instrument/filters

images, our custom Python routines were employed for data reduction, as outlined in Figure 2.3. The schematics distinguish retrieved and processed data in blue, calibration images in a yellow background, and pink-boxed objects representing Python packages or external software used in the reduction process. Processed images are labeled according to the applied data reduction steps (DC - Dark Corrected; SC - Sky Corrected; FFC - Flat Field Corrected; CC - Coordinate Calibrated).

The raw data frames go through a series of reduction and calibration steps outlined in Fig. 2.3, and described in the following sections.

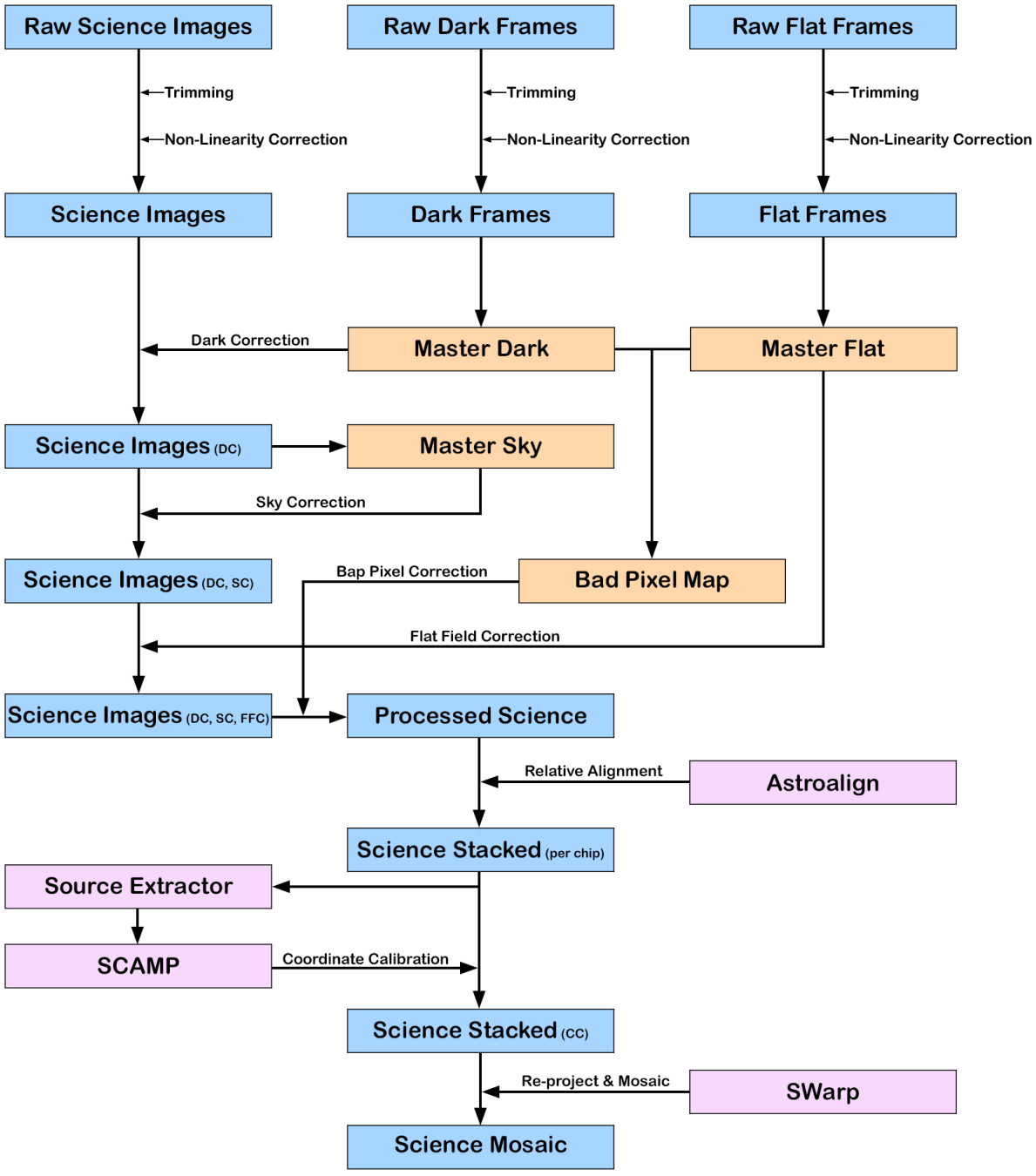

Figure 2.3: Illustration of the procedures undertaken in the reduction of the NEWFIRM dataset. DC: Dark Corrected; SC: Sky Corrected; FFC: Flat Field Corrected; CC: Coordinate Calibrated.

2.3.1 Trimming

Each detector is read out through 64 amplifiers, yielding images of 2048×2112 pixels. The Orion detectors include reference pixels to monitor electronic stability during readout, with one reference pixel for each of the 64 amplifiers. These reference pixels are read once per row during the readout process and stored at the end of each image row, creating an extra section spanning from pixel 2049 to 2112. The reference pixels are not used in pipeline processing, so this section can be removed (Shaw, 2015).

Furthermore, within the primary 2048×2048 data section, there is a 1-pixel border containing reference columns or problematic pixels (Dickinson and Valdes, 2009). This border will be retained for the non-linearity correction (Section 2.3.2) to accurately account for the read time (Dickinson, 2008). However, it will be removed after this correction is applied.

2.3.2 Non-linearity

The NEWFIRM arrays, similar to most infrared detectors, exhibit non-linearity. As the intensity of an incident signal remains constant, the detector's recorded counts increase at a rate slower than linear. With accumulating photoelectrons in a pixel, the rate of additional electron accumulation decreases. Around 10,000 Analog-to-Digital Units (ADU), these arrays typically show about 6 to 8% non-linearity, reaching saturation slightly above this level (Dickinson, 2008; Shaw, 2015). In Figure 2.4, a schematic illustrates the linearity behavior of NEWFIRM. It demonstrates how the recorded counts by the array deviate from the actual counts that would have been recorded if the array were linear.

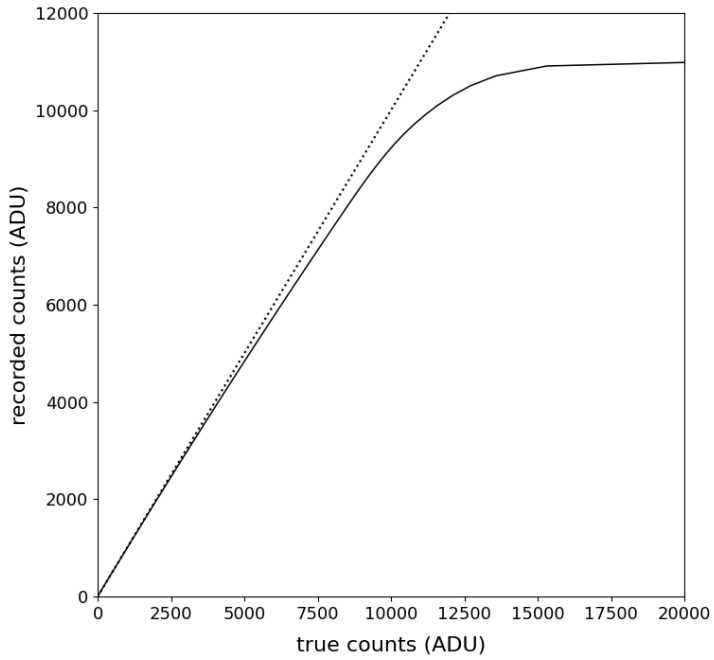

Figure 2.4: Depiction of the non-linear behavior of an infrared array. The horizontal axis denotes the expected counts for a linear count rate reaching the detector, while the vertical axis illustrates the counts captured by the pixel. A dotted line indicates a linear relationship, whereas a solid line represents a function deviating from linearity akin to the NEWFIRM arrays, leading to saturation at a maximum value slightly above 10,000 ADU.

Calibrating the non-linear behavior of infrared arrays ensures photometry quality between different source intensities, from the brightes to the faintest of sources. Calibrating linearity in NEWFIRM proves challenging because the recorded images do not encompass all the original counts collected in each pixel.

The arrays operate in a correlated double sampling (CDS) mode. This involves resetting the array, followed by a non-destructive read of each pixel after a brief yet variable time interval. The interval between the reset and the first read differs across pixel positions. After the initial read, the integration time elapses, and then the pixels undergo another read. The recorded final value for each pixel represents the difference between these two readouts. However, the total accumulated counts were actually higher due to counts collected during the reset-to-1st-read (r2r) interval. In the most common observing mode with NEWFIRM, which was the one used in all retrieved data (4 digital averages and 1 Fowler sample) the duration of this interval ranges between 0.0346 to 1.1946 seconds, contingent on the pixel's location within the array (Dickinson, 2008).

To correct for non-linearity, we used the method described by (Dickinson, 2008). By knowing the readout direction of each array and using the provided equations, we corrected the non-linearity in all our retrieved data (including science images, dark frames, and flat frames). We accomplished this using our own Python routines.

2.3.3 Dark correction

Infrared imaging detectors operate within a spectrum that's invisible to the human eye, capturing thermal radiation emitted by objects. However, these detectors are prone to capturing not only the desired infrared signals but also the background noise and sensor-generated signals. This includes dark current, which is the electronic noise generated within the detector itself even in the absence of any external radiation.

To address these challenges, we performed dark correction, beginning with the creation of the master dark. Within NEWFIRM's Orion InSb array detectors, dark current is typically minimal, averaging around 0.17 electrons per second per pixel (Shaw, 2015). However, dark frame images also include electronic bias effects driven by on-chip co-additions, digital averages, Fowler samples, and exposure duration, particularly noticeable in very brief integrations. But when subtracted from the scientific images, the master dark significantly mitigates these undesirable effects.

To generate the master dark, it is recommended to acquire a series of dark frame images matching the exact readout parameters of the scientific data. This includes factors like integration time, digital averages, co-additions, and Fowler sampling. Dark frames are filter-independent since no light passes through during their capture. This allows the same dark frames and, subsequently, master dark to be used for both Ks and H filter images, as shown in Table 2.1.

The data retrieved comprised several dark frames taken on the same day as the scientific observations. Individual dark frames have been median-combined to produce a master dark. Then the master dark was subtracted from the science images. This eliminates the dark current and other electronic bias components from the scientific images while preserving the genuine signal originating from external sources.

2.3.4 Sky correction

In ground-based IR imaging, the signal from the background overwhelmingly dominates the detected signal in broad-spectrum filters from most astrophysical sources, often surpassing the flux from the faintest stars and galaxies by several orders of magnitude. The background flux consists of several components, including contributions from the night sky (resulting from OH^- emission, moonlight, and a thermal component at the K_S-band), heat sources in the telescope dome, the telescope optics, and dark current. Notably, molecular emission in the night sky can exhibit significant variations on timescales of a few minutes and can also vary spatially across the extensive FoV of the NEWFIRM instrument. Therefore, achieving accurate sky subtraction is crucial for obtaining reliable photometric measurements.

To address this challenge, a master sky was created from the dark-corrected science images. It should be noted that science images have been taken at slightly different positions (procedure called dithering). This allowed us to get the estimate of the background emission in most of the pixels, since stars will not be located at the same positions on the detector. To obtain the master sky, we normalized the dark-corrected images by dividing them by their own median. Then the images were median-stacked. Finally, the normalized master sky is multiplied by the median of each dark-corrected science image, before being subtracted from it. This process effectively subtracts the sky effects from the dark-corrected science images.

2.3.5 Flat field correction

The response of a detector can vary across the array due to factors like the light path, extraneous particles, filter transmission, and pixel response variability. To address these challenges, flat field correction is used. This correction standardizes the response of each pixel across the sensor's focal plane, ensuring that all pixels capture light equally.

Flat field images consist of a set of frames of a uniformly illuminated surface. For our NEWFIRM data, the observing team employed dome flats — a widely used method to acquire flat field images within telescope domes. These domes act as diffusive, featureless reflectors, appearing out of focus for the telescope optics. Dome flats are created by illuminating a flat screen within the dome using broad-spectrum light sources devoid of emission lines, often through incandescent lamps. This process is adaptable, enabling image capture at any time during the day.

In the NIR, it is common to take exposures both with the dome flat lamps turned on and off. Specifically in the K_S-band, where thermal emission from the white spot and various elements within the telescope or instrument structure might illuminate the detector. Taking this on-off difference helps eliminate any thermal or scattered light components present in the dome flats.

The data retrieved encompassed light-on and light-off dome flat field images for each filter, acknowledging the wavelength-dependent responsiveness of pixels. These images were captured on the same day as the corresponding observation. The median-combined light-off dome flat field images were subtracted from the median-combined light-on dome flat field images. This subtraction process mitigates biases and dark current effects, allowing a focused analysis solely on differences in light intensity. The resulting image was then normalized by dividing it by its own respective median. This normalization aimed to create an image with pixel values around unity, regardless of the exposure time in the flat frames.

This process leads to the creation of the master flat, as depicted in Figure 2.5, for the filter K_S at the CTIO. The master flat revealed notable cosmetic imperfections within the photo-active areas of the arrays. A concise description of the identified defect types, as indicated by their corresponding numbers in the Figure 2.5, is provided in the Table 2.4.

The dark- and sky-corrected science images were then divided by their respective master flat to generate the dark-, sky- and flat field-corrected science images, free from the constraints mentioned earlier.

2.3.6 Bad pixel correction

The NEWFIRM detector arrays exhibit various defects that require masking or interpolation during the image reduction process. These defects encompass a range of issues, including cracks in the detector substrate, areas with significantly reduced sensitivity due to contaminants on the arrays, portions of the detectors that have become detached from the readout electronics, pixels with unusually high dark current,

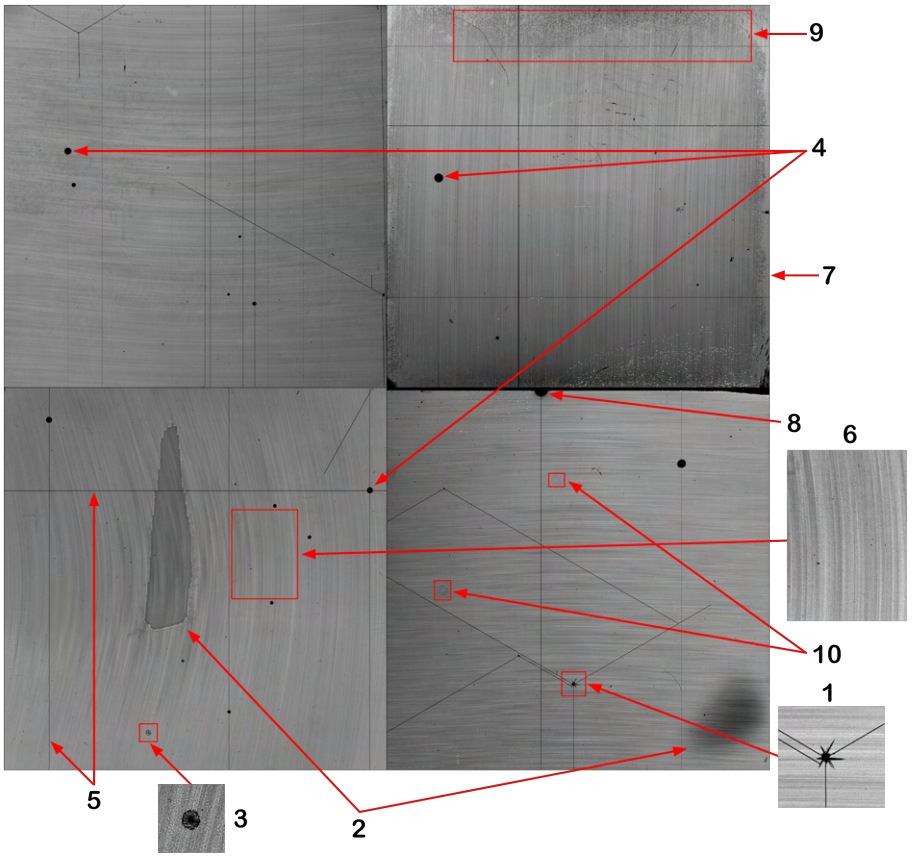

Figure 2.5: The K_S-band master flat image displaying all four arrays is presented. Various cosmetic defects inherent in the NEWFIRM sensors are outlined, with a description available in Table 2.4.

Table 2.4: Master flat defects in the NEWFIRM sensors (Shaw, 2015).

Defect	Description
1.	Diagonal fractures in the InSb substrate, exhibiting complete insensitivity.
2.	Widespread areas with slightly diminished sensitivity and increased dark current.
3.	Small sections with reduced sensitivity due to impurities present on the arrays.
4.	Photo-Emissive Defects (PED) caused by electrical shorts in the bonded readout electronics, leading to circular areas as large as approximately 50 pixels in diameter, displaying zero sensitivity after passivation.
5.	Non-functional rows or columns, which are frequently, though not invariably, linked to PED occurrences.
6.	Residual patterns showing slight fluctuations in substrate crystal growth.
7.	Regions at the edges or corners of the detector that have detached from the readout electronics, resulting in zero sensitivity.
8.	Damaged regions on the detector, surrounded by areas of heightened dark current and non-linear response.
9.	Extended regions exhibiting elevated dark counts and pixel non-linearity.
10.	Out-of-focus dust particles.

pixels with atypical linearity responses, and regions with detector damage that emit a noticeable, bright glow.

In our approach, we utilized the master flat and master dark, visually inspecting their value distributions. Then, we selected an acceptable range of values in order to exclude outliers and unexpected values. In principle, we would observe dark bad pixels in the master flat images and bright bad pixels in the master dark images. Table 2.5 displays the value range for both the master flat and master dark for each detector array. This analysis resulted in a binary matrix, where a value of 1 was assigned to pixel positions outside the value range (deemed as bad pixels), and a value of 0 was assigned to the remaining pixels (deemed as good pixels).

Table 2.5: Value ranges for the bad pixel map in the master flat and master dark for each detector array.

Observatory		*Cerro Tololo*	*Kitt Peak*		
Filter	Array	K_S	KX_S	HX	JX
Master Flat	SN019	0.73 — 1.28	0.73 — 1.25	0.70 — 1.25	0.72 — 1.24
	SN022	0.64 — 1.32	0.73 — 1.26	0.72 — 1.28	0.72 — 1.28
	SN013	0.70 — 1.32	0.71 — 1.25	0.7 — 1.27	0.70 — 1.26
	SN011	0.70 — 1.30	0.74 — 1.26	0.73 — 1.25	0.75 — 1.23
Master Dark	SN019	-31 — 4	-55 — 5		-48 — 2
	SN022	-30 — 7	-28 — 7		-22 — 4
	SN013	-27 — 4	-30 — 7		-22 — 4
	SN011	-55 — 0	-41 — 6		-22 — 4

To address these identified bad pixels, our Python routine systematically traverses each pixel on the detector. When encountering a pixel flagged as bad in the bad pixel map matrix, it interpolates its new value using the surrounding non-flagged pixels in an 8 by 8 box. If fewer than 65% of pixels in the box were good, the pixel is assigned a NaN (Not a Number) value to prevent it from impacting subsequent stages.

2.3.7 Alignment

At this point, we have a set of reduced dithered images for each chip. These images now need to be stacked into a single deep exposure per chip, but previously need to be corrected for the telescope lens' curvature, spherical nature of the sky, and dithering.

As previously mentioned, although each image exhibits dithering, the offset is small enough for common sources to be identifiable across all images within each set. To address this, we started by aligning the images using only their World Coordinate System (WCS). Then we utilized the $AstroAlign$ package (Beroiz et al., 2020). This tool identified common sources among images taken by the detector, utilizing them as references for its alignment routine. For each chip, we selected one image as a reference for aligning the others. $AstroAlign$ then performed a first order transformation on the other images to match the alignment of the reference image. Afterwards, for a finer alignment, we utilized a Python algorithm to identify stars in the images and supplied their positions to $AstroAlign$. Then, $AstroAlign$ applied higher-order polynomials to adjust the alignment, correcting for the previously mentioned effects. This process was iterated until all images aligned with the chosen reference image. The result was a median-combined aligned image for each chip derived from dithered images.

2.3.8 Coordinate calibration and mosaic

The science stacked images now needed to have their pixel coordinates calibrated onto the WCS. We started by using a software called *SExtractor* (Source-Extractor; Bertin and Arnouts 1996) to constructs a catalogue of celestial objects. Following this, we used *SCAMP* (Software for Calibrating AstroMetry and Photometry; Bertin 2006) to read the *SExtractor* catalogues in order to compute astrometric solutions, facilitating the coordinate calibration of each science stacked image. Then, we utilized the 2MASS (Cutri et al., 2003) catalogue as a reference to refine the *SCAMP* astrometric solution. *SCAMP* aligns the positions of detected sources with known celestial objects, correcting their astrometry to account for distortions and other instrumental effects that could affect the astrometry accuracy.

With the established correct WCS, we use *SWarp* (Bertin et al., 2002) in the subsequent phase of our pipeline. *SWarp* co-adds FITS images and warps the pixels positions based on the astrometric projection defined in the now calibrated WCS standard. This co-addition process results in the creation of a single mosaic image for each set of observations, integrating the information from the four chip images of the NEWFIRM detector array.

The data reduction process was concluded, yielding three observed fields (Table 2.2). The field F1 was captured solely in the K_S filter, while the other two, F2 and F3, were recorded in J, H, and K_S filters. Consequently, we obtained a total of seven mosaic images. The resulting mosaic images for the K_S filter are depicted in Figure 2.1.

Several of the mosaics feature noteworthy objects, which are highlight in Figures 2.6, 2.7, 2.8 and 2.9

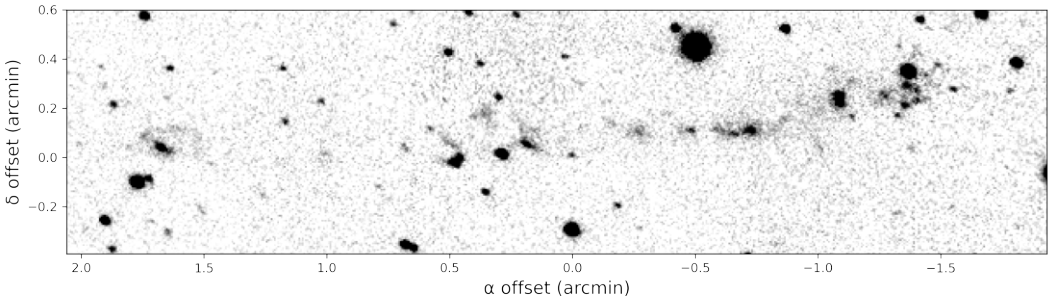

Figure 2.6: Bipolar protostellar outflow MHO 1321 (Ybarra et al., 2010) as seen in the K_S filter. The origin is set at $(\alpha, \delta)(J2000) = (06^h35^m27.18^s, +03°56'15.61'')$.

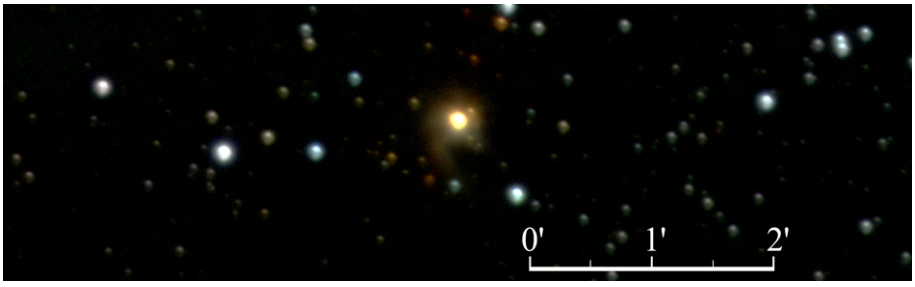

Figure 2.7: Multi-band composite image of YSO IRAS 06294+0352 (Suto et al., 1992), merging K_S-band (red), H-band (green), and J-band (blue). The center of the image is set at $(\alpha, \delta)(J2000) = (06^h32^m07^s, +03°50'05'')$.

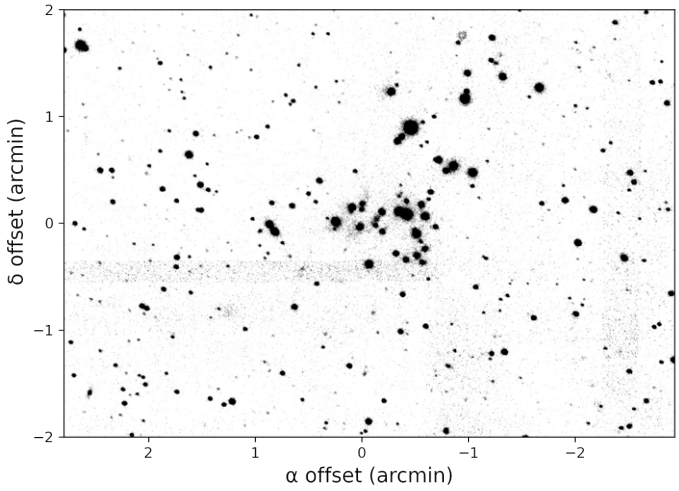

Figure 2.8: Star Cluster PL07 (Phelps and Lada, 1997) through the K_S filter. The origin is set at $(\alpha, \delta)(J2000) = (06^h35^m31.96^s, +03°58'54.21'')$.

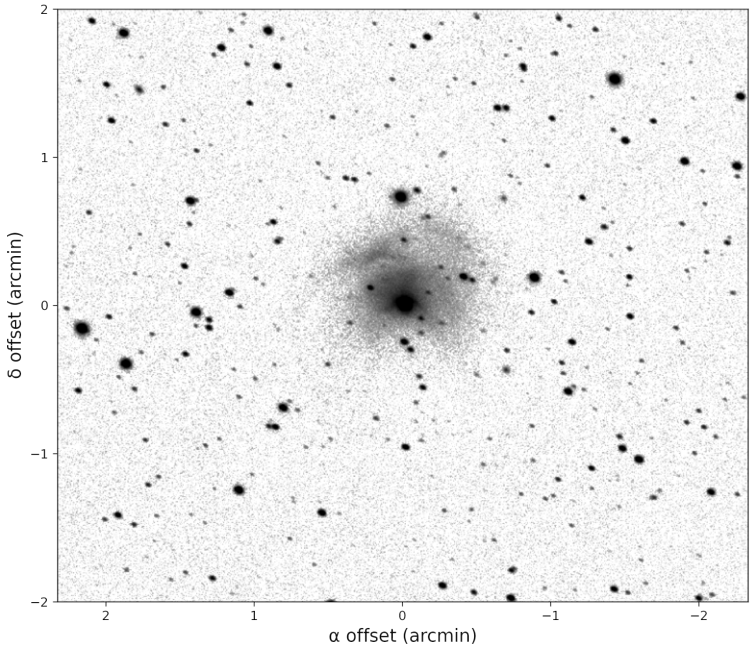

Figure 2.9: Reflection Nebula GN 06.32.5 through the K_S filter. The origin is set at $(\alpha, \delta)(J2000) = (06^h35^m09.28^s, +03°51'43.11'')$.

2.4 Photometry

Photometric analysis was conducted on the seven mosaics obtained through the data reduction process. The flux values of the sources in these mosaic images are expressed in ADU, having undergone linearization (Section 2.3.2), these values linearly correlate with the brightness of the object. This section provides a detailed account of how we determined the magnitude values for our sources and calibrated them using the 2MASS catalogue.

2.4.1 Source-Extractor and PSF Extractor

We began by using *SExtractor* (Bertin and Arnouts, 1996) to obtain the position of stars in each mosaic, disregarding any saturated source. To identify saturated sources, a count threshold of 8,000 ADU per

number of co-adds was set, with values exceeding 16,000 ADU considered saturated for the K_S- and H-band mosaics (readout with two co-adds) and 8,000 ADU for the J-band mosaic (readout with one co-add).

Then, for each mosaic, the *SExtractor* output was given to *PSFEx* (PSF Extractor;Bertin, 2011), a software capable of generating PSF (Point-Spread Function) models. The *SExtractor* software outputs a catalogue that must include information about the size of vignettes associated with each object. Vignettes, representing cuts from the original image of suspected point sources, were chosen to be 25 by 25 pixels. The *SExtractor* catalogue also specified a fixed aperture size (20 pixels) used to normalize the amplitude of the PSF models. This aperture needed to be wide enough to mitigate the influence of seeing but not so wide as to be susceptible to pollution from nearby sources.

PSFEx selected potential point sources from the *SExtractor* catalogue based on measurements like ellipticity, excluding sources with ellipticity > 0.1. It could also exclude sources flagged for contamination or saturation effects, leveraging *SExtractor*'s system of flags indicating issues encountered during source processing. *PSFEx* excluded all sources with flag values above 254 and signal to noise ratios bellow 20.

PSF extraction is an iterative process, with each iteration improving the accuracy of the PSF model by comparing it to the image data. During this process, neighboring sources in the vignettes were filtered out. After completion, the PSF model, along with relevant diagnostics, was stored in a file as output. These PSF models were then used in a second run of *SExtractor* on the mosaics. Extracted sources in this run had to exhibit at least a 2σ flux variation across 5 pixels from the background. The output catalogue by *SExtractor* in this run included the position of sources in the equatorial coordinate system, along with their uncalibrated flux values.

To ensure that *SExtractor*'s catalogue only contains point sources (unlike resolved galaxies), we began by analyzing the SPREAD_MODEL parameter, which indicates the local PSF model. We filtered out sources deviating more than 3σ from the median. Additionally, we excluded sources with ellipticity values above 0.5, as high ellipticity suggests non-stellar entities. The value and weight of flags was utilized to eliminate sources impacted by issues such as saturation and memory overflow. Those with flag values exceding 3 were excluded from the catalogue. Additionally, sources situated in close proximity to image borders were eliminated. This decision stems from the acknowledgment that regions near image borders often exhibit heightened noise levels and an abundance of bad pixels, compromising the accuracy of the uncalibrated flux values.

2.4.2 Calibrating to 2MASS

At this stage, the catalogues generated through the *SExtractor* and *PSFEx* routines featured uncalibrated-flux values for all sources, which are not yet in physical units. To calibrate our photometry, we cross-matched the NEWFIRM catalogue to that from 2MASS survey. Prior to this cross-matching, the flux values of our sources were converted into instrumental magnitudes, using the following equation:

$$m_{\text{instr}} = -2.5 \log \left(\frac{f}{t_{\text{exp}}} \right), \tag{2.1}$$

where the instrumental magnitude is represented by m_{instr}, the uncalibrated flux of a source is f, and t_{exp} is the exposure time of the images.

To calibrate our photometry, we calculate the zero point (ZP), which is an offset with respect to 2MASS magnitude, as well as the color-terms. The color-terms may arrise due to differences in NEWFIRM and 2MASS filters, and were computed using the J and K_S filters, as they show the largest wavelength differences among the three filters.

The stars in the two catalogues were matched within a $1''$ radius tolerance. Both the ZP and colour-term corrections were determined via a linear fit, where the ZP corresponds to the intersection of the fit, and the colour-term corresponds to the slope of the following system of equations:

$$\begin{aligned} J &= J_{\text{instr}} + \text{ZP}_1 + c_1 \cdot (J - K) \\ H &= H_{\text{instr}} + \text{ZP}_2 + c_2 \cdot (J - K) \\ K_S &= K_{S\text{instr}} + \text{ZP}_3 + c_3 \cdot (J - K), \end{aligned} \tag{2.2}$$

where J_{instr}, H_{instr}, and $K_{S\text{instr}}$ are the instrumental magnitudes.

As mentioned earlier we have 7 mosaics, two regions, F2 and F3, cover by J, H and K_S filters and F1 covered solely in the K_S filter. In this region, the calibration has been performed using the ZP only.

During the calculation of the ZPs and colour-terms not all sources were used. This was necessary because the faintest sources exhibited significant scatter and the brightest sources had a non-linear relationship with the 2MASS catalogue. For example, for the F1 only the data depicted in black, in the left panel of Figure 2.10, was used to obtain the ZP value.

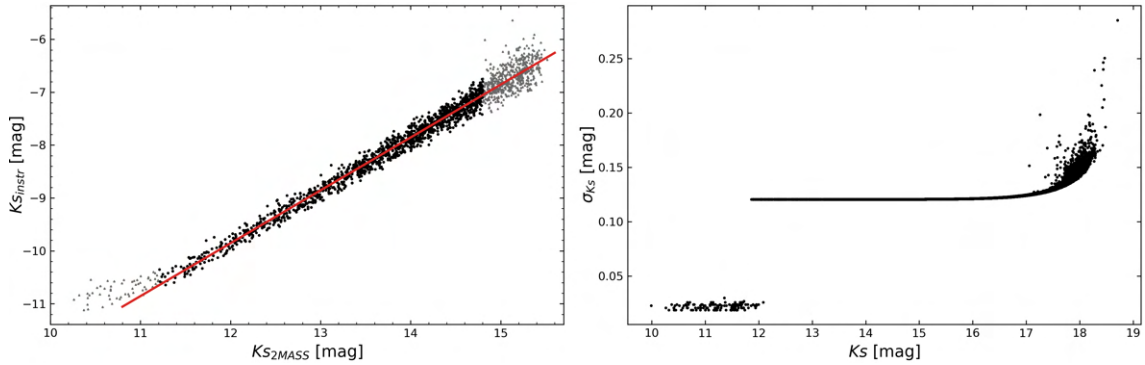

Figure 2.10: In the left panel, we compared instrumental magnitudes with 2MASS magnitudes in the F1 to obtain the ZP. We used only the black data points for the linear fit due to high variation in faint sources and non-linearity in bright sources (gray). In the right panel, we show the uncertainties vs magnitude for the F1 mosaic. We replaced bright sources with 2MASS photometry, causing a noticeable discontinuity.

For the other two regions, F2 and F3, where we have J-, H- and K_S-band, ZP and colour-term corrections were applied. The ZP and colour-term along with their uncertainties were determined using the plots in Figure 2.11. The interception of the linear regression in these colour-colour diagrams is the corresponding ZP and the slope is the corresponding colour-term.

The determined values for the ZPs and colour-terms can be found in the Table 2.6. It is worth noting that the color term is negligible, as its uncertainties exceed its value. This indicates that the J, H, and K_S filters used in the NEWFIRM observations align almost perfectly with those present in 2MASS.

Table 2.6: ZPs and colour-terms for each filter and field, along woth corresponding uncertainties

Filter	K_S			**H**		**J**	
Field	F1	F2	F3	F2	F3	F2	F3
zero point (mag)	21.86	21.78	21.77	22.68	22.66	22.51	22.51
$\sigma_{\text{zero point}}$ (mag)	0.12	0.10	0.11	0.11	0.11	0.14	0.15
colour-term	—	-0.025	-0.083	-0.009	-0.068	0.05	-0.01
$\sigma_{\text{colour-term}}$	—	0.026	0.027	0.027	0.027	0.04	0.05

Following the ZPs and colour-terms corrections, photometry of the brightest stars was replaced

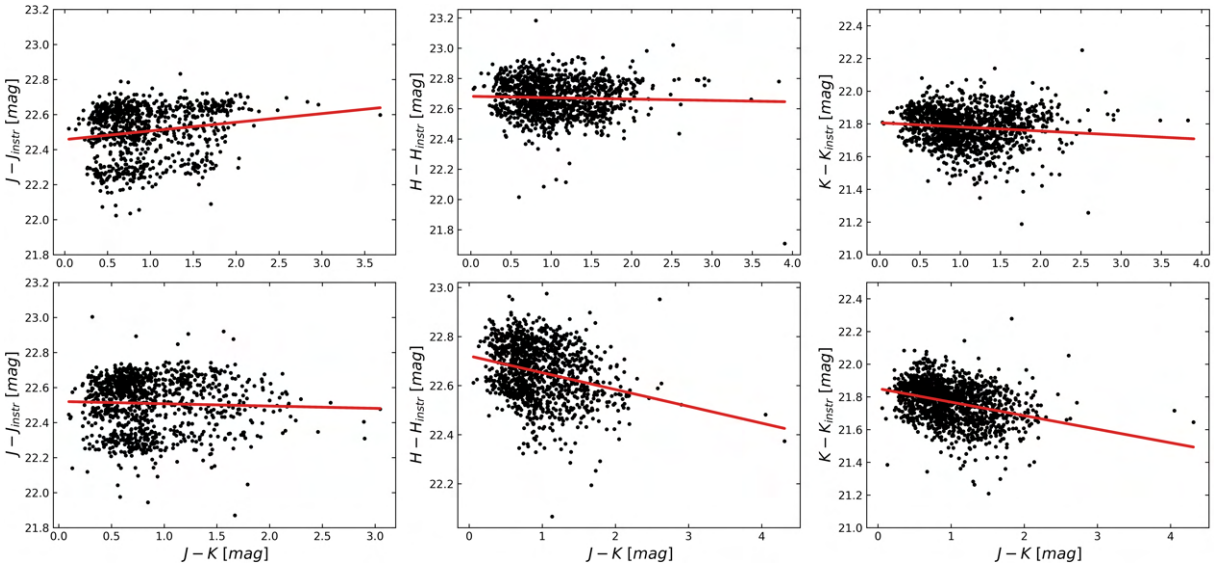

Figure 2.11: The colour-colour diagram for F2 (top panels) and F3 (bottom panels) of sources matched against 2MASS. The interception of the linear regression and its slope are the ZP and colour-term, respectively.

by that from 2MASS, to mitigate potential saturation issues. The uncertainties were calculated by error propagation, including the uncalibrated flux uncertainties from *SExtractor*, and the uncertainties of ZPs and color terms. For F1 the plot of uncertainty as a function of magnitudes is depicted in the right panel of Figure 2.10. For F2 and F3 this is depicted in the top and bottom panels of Figure 2.12, respectively.

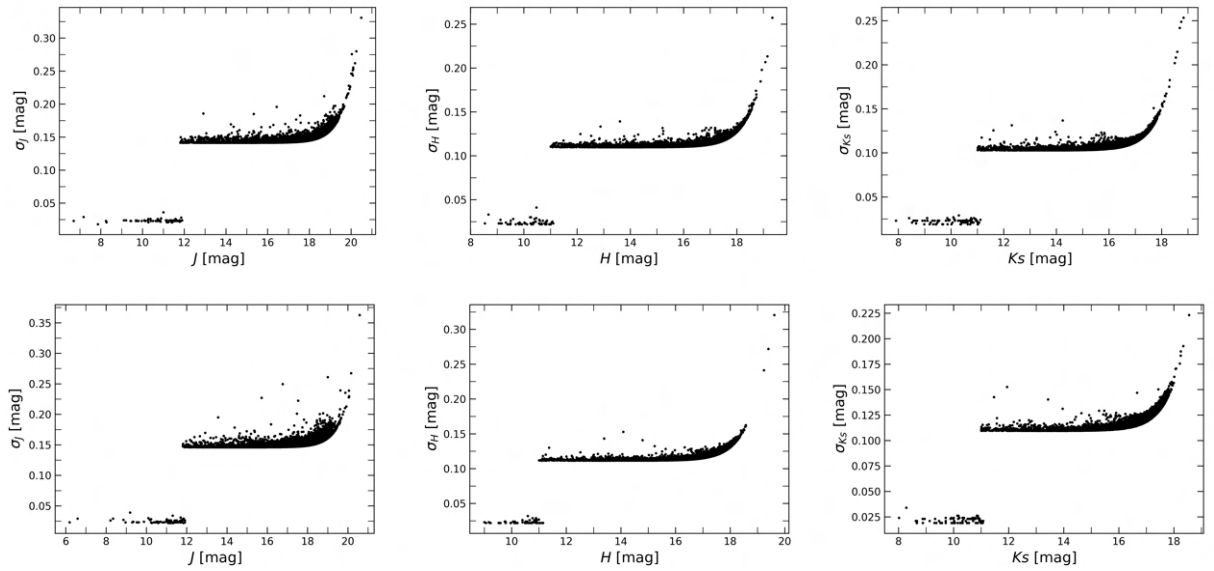

Figure 2.12: The photometric uncertainties as a function of magnitude are presented for the region F2 (top panels) and F3 (bottom panels). To address potential saturation in the bright sources, their photometry was substituted with values from 2MASS, resulting in a noticeable discontinuity.

Due to a slight overlap on the F1 and F2 in the K_S filter, a comparison of independently obtained magnitude values is presented in Figure 2.13. It is evident from the figure that their relationship is nearly one-to-one, indicating that their values are nearly identical within the uncertainties.

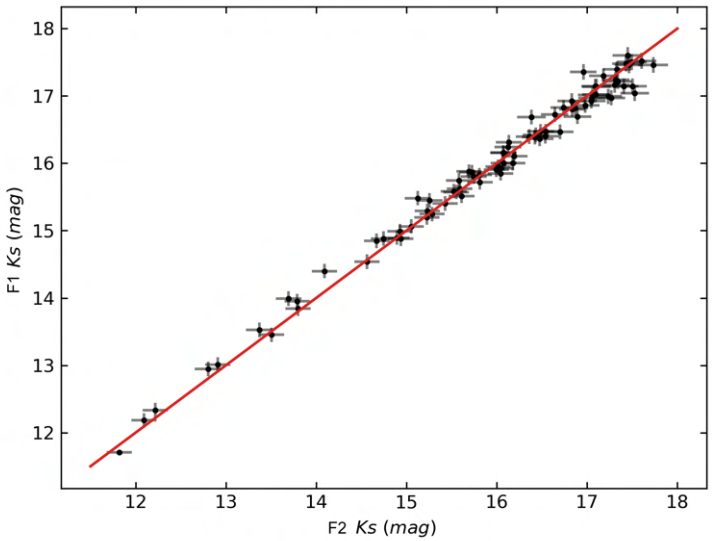

Figure 2.13: Magnitude comparison of the overlapped stars in the K_S filter.

Upon completing the photometry calibration process, we merged the resulting photometry catalogues into a single catalogue. This catalogue includes the positions of $28,584$ sources, each with at least one of J-, H-, or K_S-band magnitudes, along with their corresponding uncertainty measurements. In regions of overlap, we selected the magnitude value associated with the smaller uncertainty. The median uncertainties for the photometry in the J-band, H-band, and K_S-band, obtained through the error propagation method, are 0.15 mag, 0.14 mag, and 0.13 mag, respectively.

Chapter 3

Photometric Data Collection

This chapter focuses on the assembly of a photometric catalog spanning from optical to MIR wavelengths, and inspection of its main properties. This catalogue of astronomical sources is then used, in Chapter 4, to identify Class I and Class II YSOs within the Rosette Nebula region.

3.1 Datasets

3.1.1 IRAC MIR photometry

In order to select YSOs and categorize them into Class I and Class II, we need to rely on MIR photometric values. Thus, we used MIR catalogue from Almendros-Abad et al. (2023), which was acquired using the IRAC (InfraRed Array Camera; Fazio et al., 2004) on the Spitzer Space Telescope (Werner et al., 2004). The MIR data used in Almendros-Abad et al. (2023) was retrieved from the Spitzer Heritage Archive within a 1.5° radius centered on NGC 2244 (Figure 3.1). In order to address issues arising from the presence of a bright extended nebulosity, which was impeding source detection and photometry measurement, a nebulosity filter was applied. This filter is described in detail in the work of Bertin et al. (in prep.). This filter separates the emissions from celestial objects (where photometry was performed) and the background emissions, as displayed in Figures 3.2 and 3.3, respectively.

We used the mosaic images displayed in Figure 3.1 to obtain the composite images that can be seen in Figure 3.4 and 3.5 using our own Python scripts and *Photoshop* (Adobe Systems, 2012).

The MIR data from Almendros-Abad et al. (2023) has photometry from four IRAC filters, namely, Channel 1 (3.55 µm), Channel 2 (4.49 µm), Channel 3 (5.73 µm), and Channel 4 (7.87 µm)[1]. These filters are commonly referred to as IRAC1, IRAC2, IRAC3, and IRAC4, respectively. To create a single catalogue with data from all four IRAC filters, we conducted matching within a $1.5''$ radius tolerance. This value was selected as it approximates the spatial resolution of all IRAC filters. Celestial objects with at least one match were combined into a single source using their median coordinates. To ensure all sources were accounted for, those without matches were also included.

3.1.2 Optical-NIR photometry from Mužić et. al. (2022)

The MIR IRAC catalogue served as a foundation for our dataset. To complement it, we used photometric data from the optical and NIR. We began by merging the previously acquired NEWFIRM catalogue with the dataset outlined in Mužić et al. (2022). This dataset covers a region of $2.8^\circ \times 2.6^\circ$ centered on NGC 2244. It encompasses photometric data from diverse observatories and instruments, including

[1] https://irsa.ipac.caltech.edu/data/SPITZER/docs/irac/iracinstrumenthandbook/6/

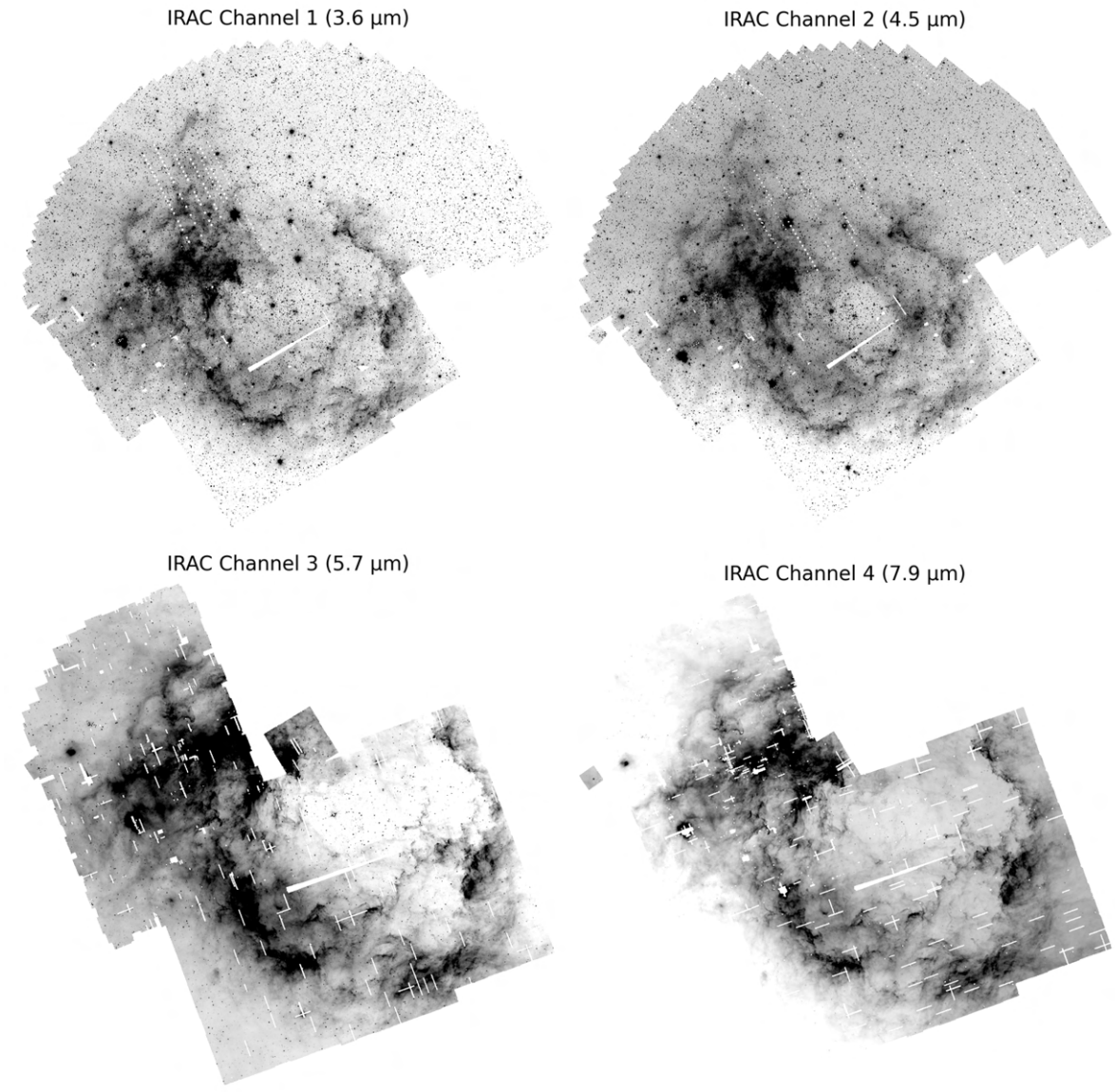

Figure 3.1: The mosaics generated by Almendros-Abad et al. (2023) prior to implementing the nebulosity filter, showcasing IRAC Channel 1, 2, 3, and 4.

CTIO (Blanco, DECam; Honscheid and DePoy 2008), CFHT (MegaCam; Boulade et al. 1998), INT (WFC; Ives et al. 1996), UKIRT (WFCAM; Casali et al. 2007), KPNO (Mayall, FLAMINGOS; Elston 1998), NTT (SofI; Moorwood et al. 1998), and ESO (VLT, HAWK-I; Casali et al. 2009). Furthermore, the dataset is complemented with photometric data from Gaia EDR3 (Gaia Collaboration, 2021), Pan-STARRS (Chambers et al., 2019), and 2MASS (Cutri et al., 2003) photometric data. Our objective was to enhance this dataset by incorporating our own photometric catalogue (Chapter 2), which includes data from KPNO (Mayall) and CTIO (Blanco) (NEWFIRM Autry et al., 2003).

The photometric data within the Mužić et al. (2022) dataset is calibrated to be aligned with the filters: u, g, r, i, z, y tied to the Pan-STARRS PS1 catalogue; Y tied to the UKIDSS (Lawrence et al., 2007) photometric system; J, H, K_S tied to the 2MASS catalogue; G, G_{BP}, G_{RP} tied with Gaia photometric system.

As our NEWFIRM catalogue was calibrated to the 2MASS catalogue, we were able to directly com-

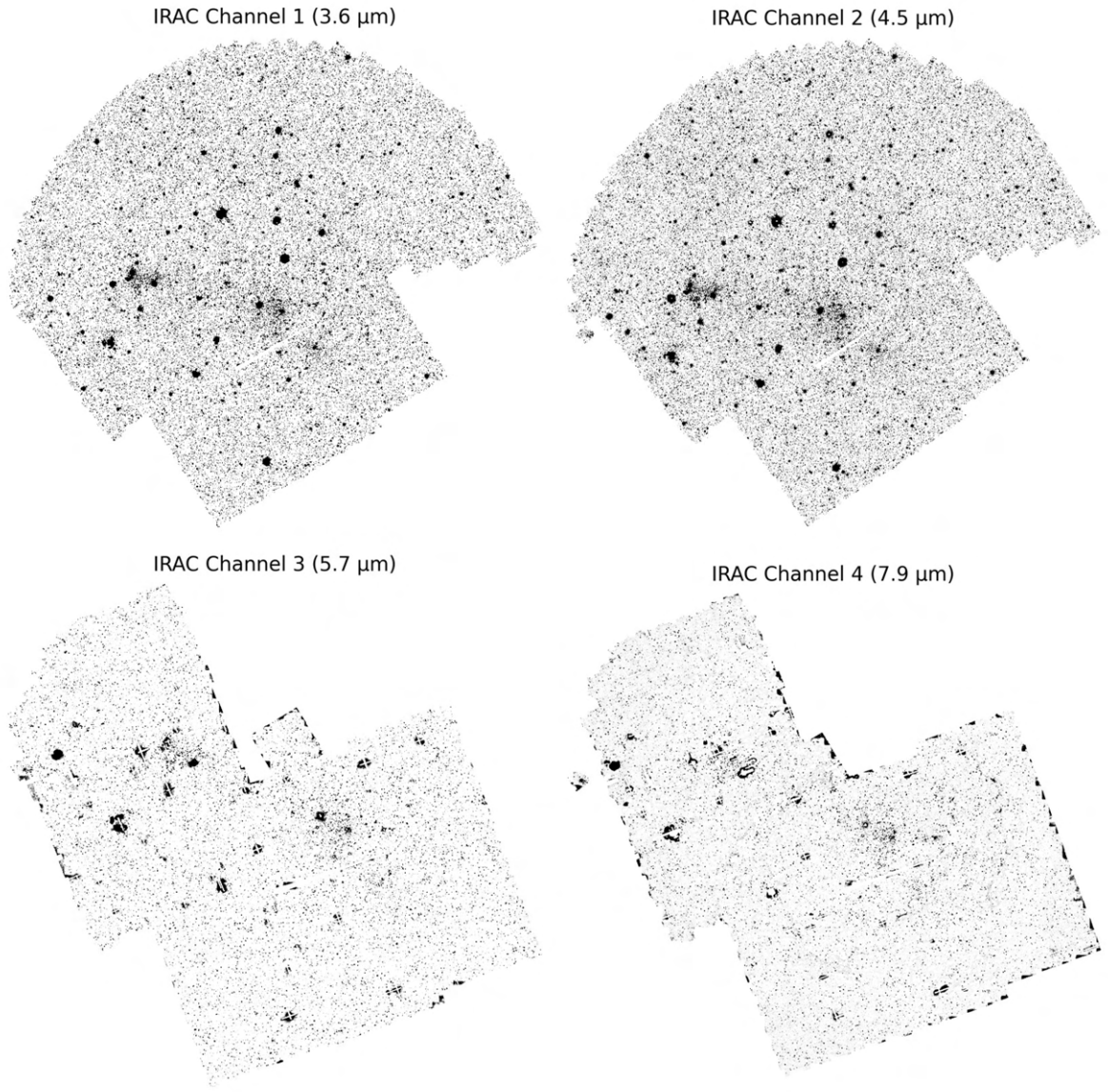

Figure 3.2: The same mosaics as in Figure 3.1 is presented with the nebulosity filter applied. This denebulized image retains only the celestial objects, enabling accurate photometry.

bine the J, H, and K_S filters from both datasets. For sources present in both catalogues (i.e., celestial sources matching within $1''$), we selected the photometric value that had the least uncertainty.

Then, we performed matching within a $1.5''$ radius to integrate this dataset onto the MIR IRAC catalogue (Section 3.1.1). Matched sources were merged, and the coordinates from the IRAC catalogue were retained. Sources not present in the IRAC catalogue (i.e., those without matches) were disregarded, since MIR photometric data is necessary for identifying and classifying YSOs more accurately. The rest of the MIR catalogue, containing sources without a NIR counterpart, was kept intact.

3.1.3 Additional public catalogues

The current dataset comprises optical, NIR, and MIR photometry of the Rosette Nebula region. However, a small portion of our IRAC data, responsible for the MIR photometry, lacks coverage in the optical and

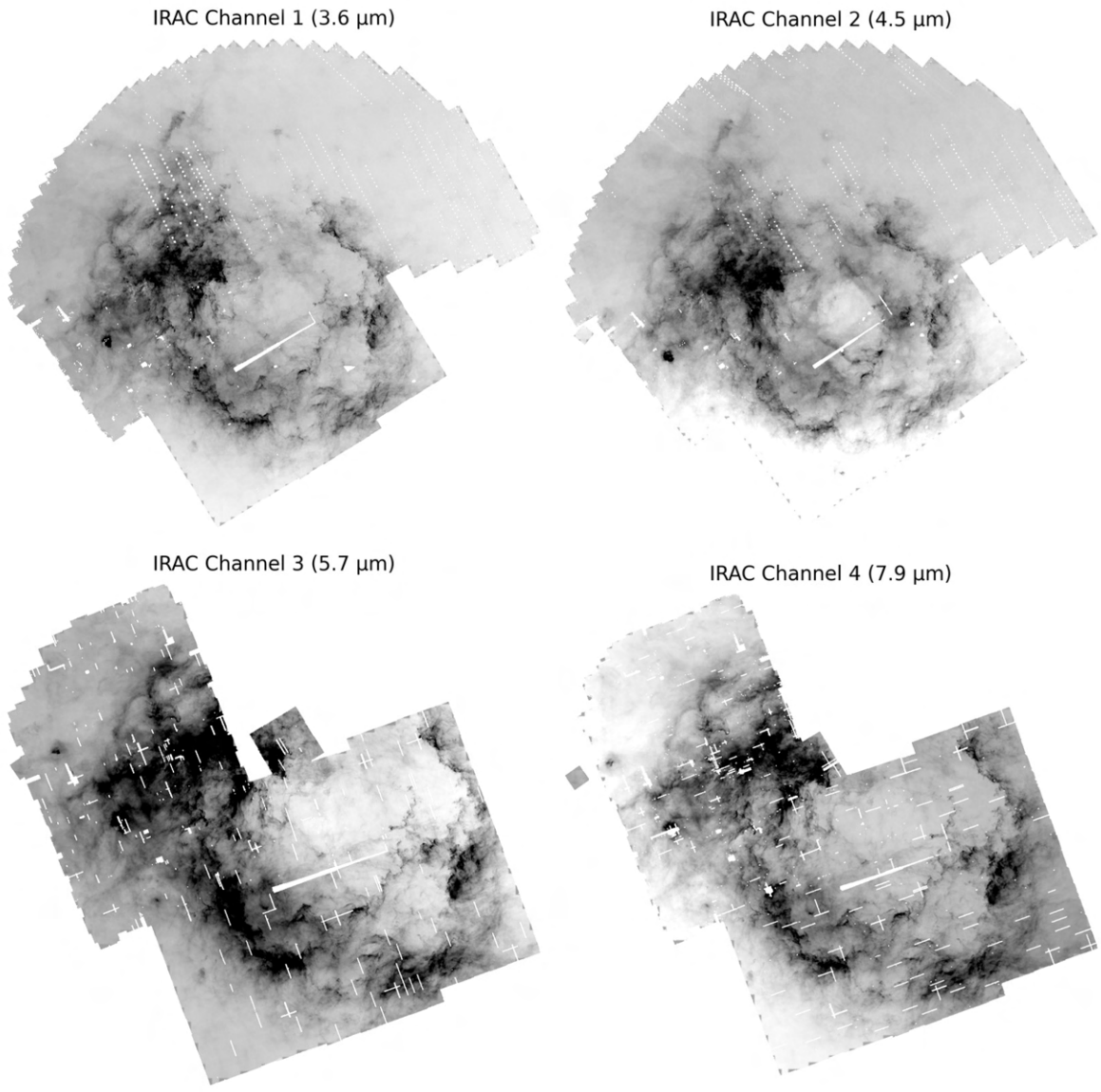

Figure 3.3: The nebulosity component of the mosaics in Figure 3.1 is shown in these figures. This image is devoid of stars and other celestial sources, revealing only the background effects. Here, the heated gas and dust from the Rosette Nebula become apparent.

NIR. As we are utilizing the IRAC data as the foundation for our analysis, it was imperative to complement this data with information from other spectral bands. To address this, we incorporated data from various public surveys.

3.1.3.1 UKIDSS

We began with data from the UKIDSS-DR6 Galactic Plane Survey (UKIDSS Consortium, 2012). We retrieved a 2° catalogue centered at NGC 2244 and initially concentrated on correcting issues related to sensor edges in the UKIDSS photometry. Sensors usually have more noise towards the edges, causing incorrect pixel values that are misidentified as sources. We were able to circumvent this by filtering out objects likely to be detector noise from the catalogue by specifically removing those where the *cl* flag was equal to zero. This process improved the data quality near the detector edges and around very bright stars.

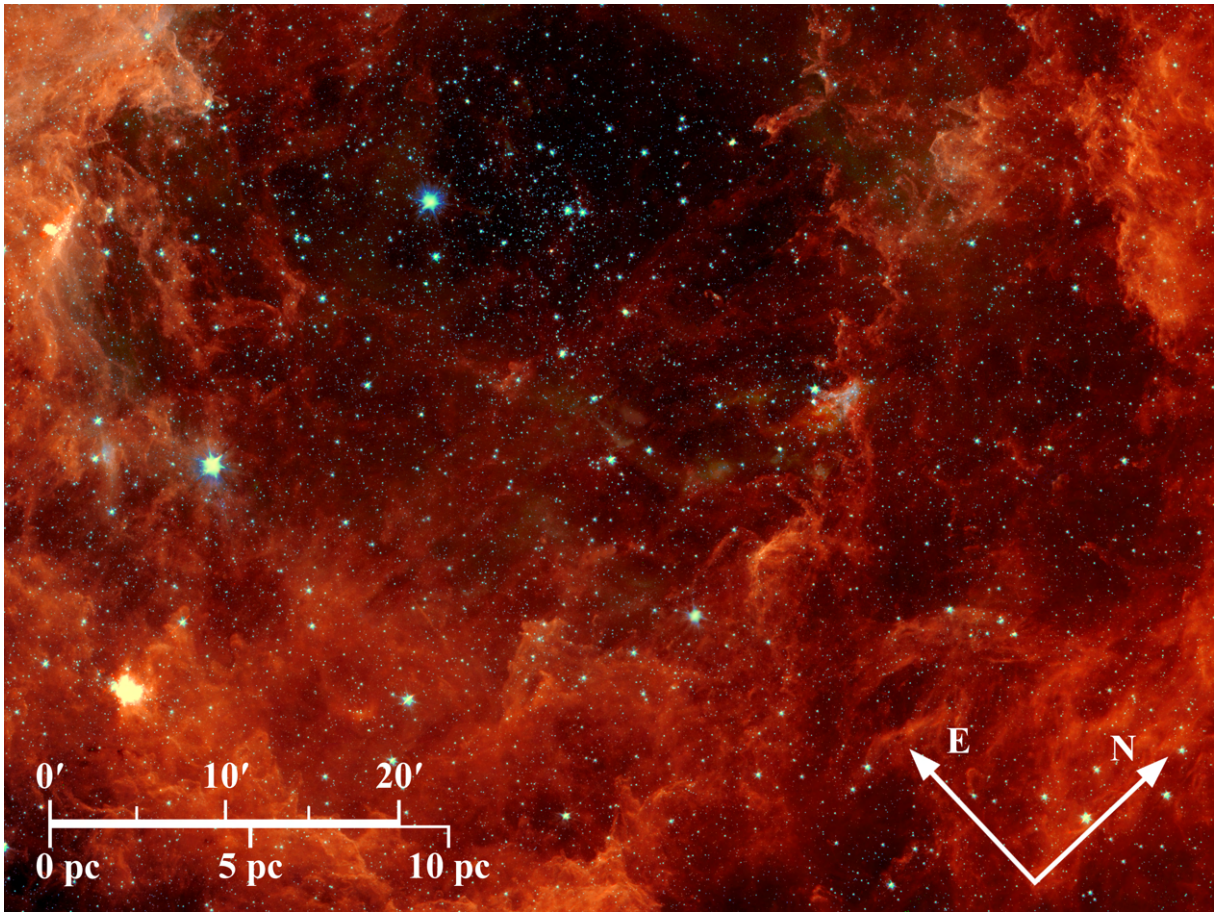

Figure 3.4: This composite image of the Rosette Nebula showcases the central region where NGC 2244 resides. The colour scheme attributes red to IRAC Channel 4, green to the Channel 2, and blue to the Channel 1.

Subsequently, we used photometric data from sources observed in other framesets in the UKIDSS catalogue. Regions near the detector edges were reobserved in other framesets to improve photometry. We retained sources with an *m* flag of 2 and discarded their detector edge photometry counterparts (sources that matched within $1''$), as their photometry was less reliable.

Furthermore, we implemented a correction to the photometric uncertainties reported in the UKIDSS catalogue. This correction, outlined in Hodgkin et al. (2008), addresses the issue of the underestimated uncertainties present in the UKIDSS data. The corrective expression is defined in Equation 3.1 as:

$$\delta_{\text{corr}} = \sqrt{c \cdot \delta^2 + s^2}, \tag{3.1}$$

where δ represents the catalogued uncertainty value and δ_{corr} represents the corrected value for the uncertainty. Additionally, c and s are constants, with values 1.082 and 0.021, respectively.

The UKIDSS catalogue supplied data in the J-, H-, and K-bands, which do not directly align with the 2MASS filters. To reconcile the UKIDSS system with the 2MASS system, we employed the system of equations outlined in Hodgkin et al. (2008), as presented below:

$$\begin{aligned} J_{\text{UKIDSS}} &= J_{\text{2MASS}} - 0.065 \cdot (J_{\text{2MASS}} - H_{\text{2MASS}}) \\ H_{\text{UKIDSS}} &= H_{\text{2MASS}} + 0.070 \cdot (J_{\text{2MASS}} - H_{\text{2MASS}}) - 0.030 \\ K_{\text{UKIDSS}} &= K_{\text{2MASS}} + 0.010 \cdot (J_{\text{2MASS}} - K_{\text{2MASS}}). \end{aligned} \tag{3.2}$$

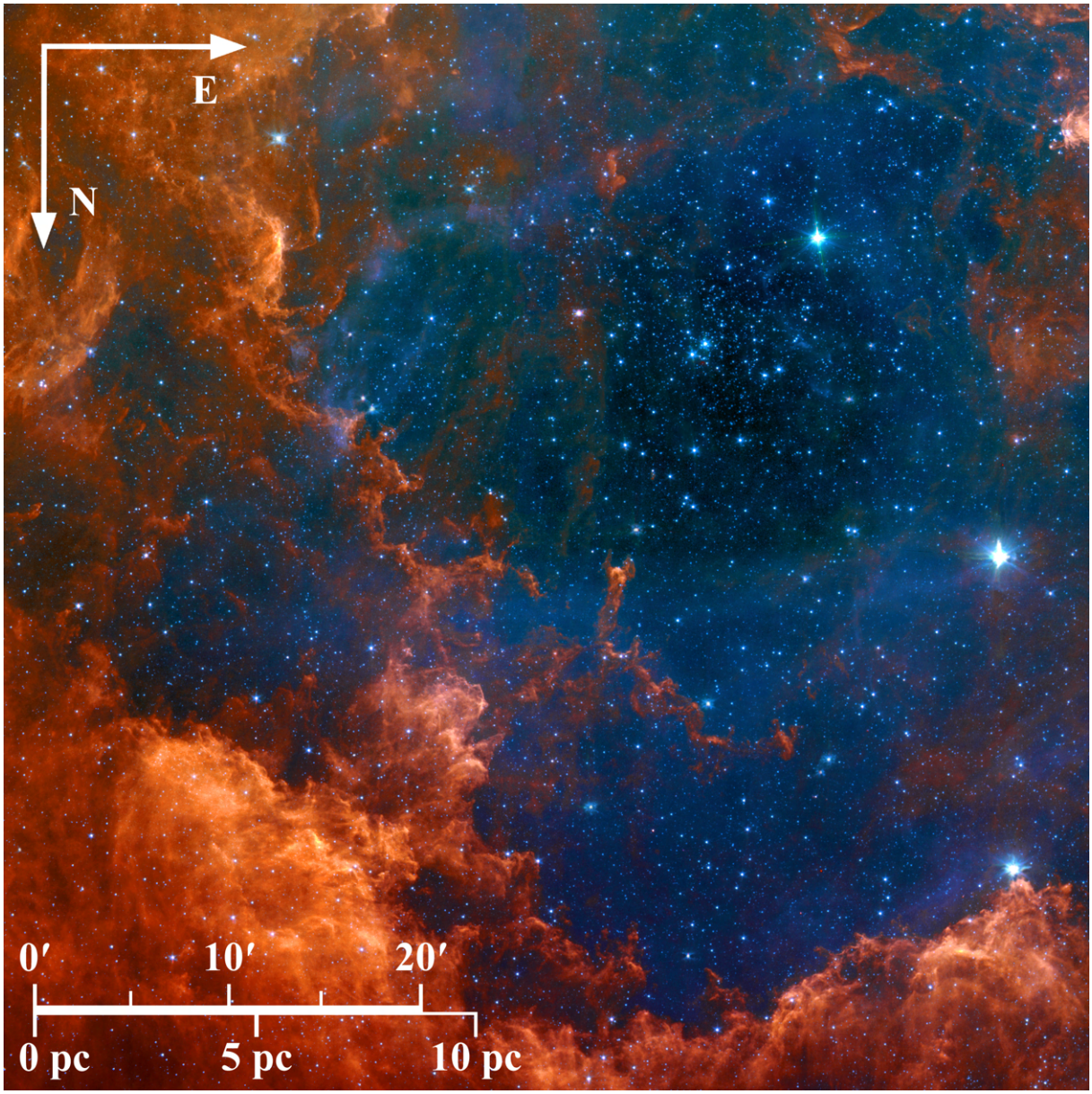

Figure 3.5: This composite image of the Rosette Nebula and NGC 2244 highlights a different field compared to the one shown in Figure 3.4. The colour scheme attributes red to IRAC Channel 4, green to the Channel 3, and blue to the Channel 2.

Using these equations, we conducted a transformation to align the data with the 2MASS catalogue. However, this transformation is applicable only to sources with data in both J and H filters. Consequently, we excluded every source lacking J and H filter data. This not only enables translation into the 2MASS photometric system but also serves as a means of cleaning out non-astrophysical sources, potentially caused by transient events or detector issues unlikely to recur in the same location with a different filter at a different time. This step greatly contributed to the overall source cleaning of the UKIDSS catalogue.

Following this, we performed matching with our dataset (Section 3.1.2) within $1.5''$. In cases where sources lacked J, H, or K_S photometric data, the corrected UKIDSS photometry values were added. When one of these bands already had data, the data with a smaller uncertainty was retained. Sources without matches to sources in the main dataset were disregarded.

3.1.3.2 2MASS

At this stage, our catalogue was expected to be fully covered in MIR and NIR wavelengths (Section 3.1.3). However, UKIDSS-DR6 Galactic Plane Survey is not an all sky survey, resulting in a small uncovered area in the NIR. To address the small uncovered area in the NIR, we retrieved a 2° 2MASS catalogue centered at NGC 2244. This not only fills the gaps left by UKIDSS, but might also include saturated stars and stars in close proximity to saturated stars, that potentially had poor or missing photometric data in the UKIDSS catalogue or the catalogue of Mužić et al. (2022).

We began by cleanning the 2MASS catalogue by eliminating sources associated with the predicted positions of known Solar System objects. These were identified through the binary asteroid or comet flag, denoted as *Aflg*. Subsequently, we filtered the data for optimal photometric quality, focusing on the JHK Photometric quality flag, referred to as *Qflg*, accepting values no worse than D[2]. Finally, we assessed the artifact contamination and confusion flag, denoted as *Cflg*, to eliminate data values that were potentially affected. Non-zero values in the *Cflg* across any band indicated that the measurements of that source might be contaminated and were consequently excluded.

After the cleaning process we merged the 2MASS data with our main dataset, through matching within $1.5''$. In cases where there was no assigned photometric value in the main dataset, the value was simply added. If a value was already assigned, the one with the lowest uncertainty was retained. Sources without matches to sources in our main dataset were disregarded.

3.1.3.3 Pan-STARRS

Finally, the IRAC data region is fully complemented with NIR photometry (Section 3.1.3.2). However, a deficiency in the optical photometry for the regions outside the $2.8^\circ \times 2.6^\circ$ centered on NGC 2244 from Mužić et al. (2022) dataset still remains. To cover these region in optical wavelengths we used the Pan-STARRS release 1 (PS1) Survey. We began by retriving data from a 2° circle centered at NGC 2244. For catalogue decontamination, the *Qual* flag was utilized, indicating whether a source was a genuine object or a potential false positive. Sources with a value equal to or greater than 64 were removed.

Moreover, the Pan-STARRS survey provided the alternative to obtain photometry data through Kron's first moment algorithm (Kron, 1980) for retrieval, which is preferred over PSF photometry. The latter is recognized for yielding inaccurate measurements for extended sources.

Following the same methodology as before, a matching within a $1.5''$ radius with our main dataset was done. In cases where there was no assigned photometric value in the main dataset, the value was simply incorporated. If a value was already assigned, the one with the lowest uncertainty was retained. Sources without matches to our dataset were disregarded.

Ultimately, we have achieved a photometric catalogue of sources covering the optical, NIR, and MIR spectra. This dataset incorporates MIR data from IRAC, processed by Almendros-Abad et al. (2023), the extensive optical and NIR dataset detailed in Mužić et al. (2022), our NIR NEWFIRM catalogue, and is complemented with UKIDSS, 2MASS, and Pan-STARRS public catalogues.

[2] https://irsa.ipac.caltech.edu/2MASS/download/allsky/format_psc.html

3.2 Photometric catalogue

3.2.1 Catalogue inspection

The catalogue from Section 3.1 includes over 1.1 million sources, covering optical to MIR wavelengths. To be included, a source had to be detected in at least one IRAC filter. However, sources with data in only one band are often noise, and IRAC photometry can be misleading near bright stars, creating spurious, non-astronomical sources. Noise is unlikely to be consistently detected across multiple filters at the same position. Therefore, by excluding sources detected in only one band, the catalogue is reduced to 567,008 sources, roughly half of the original count.

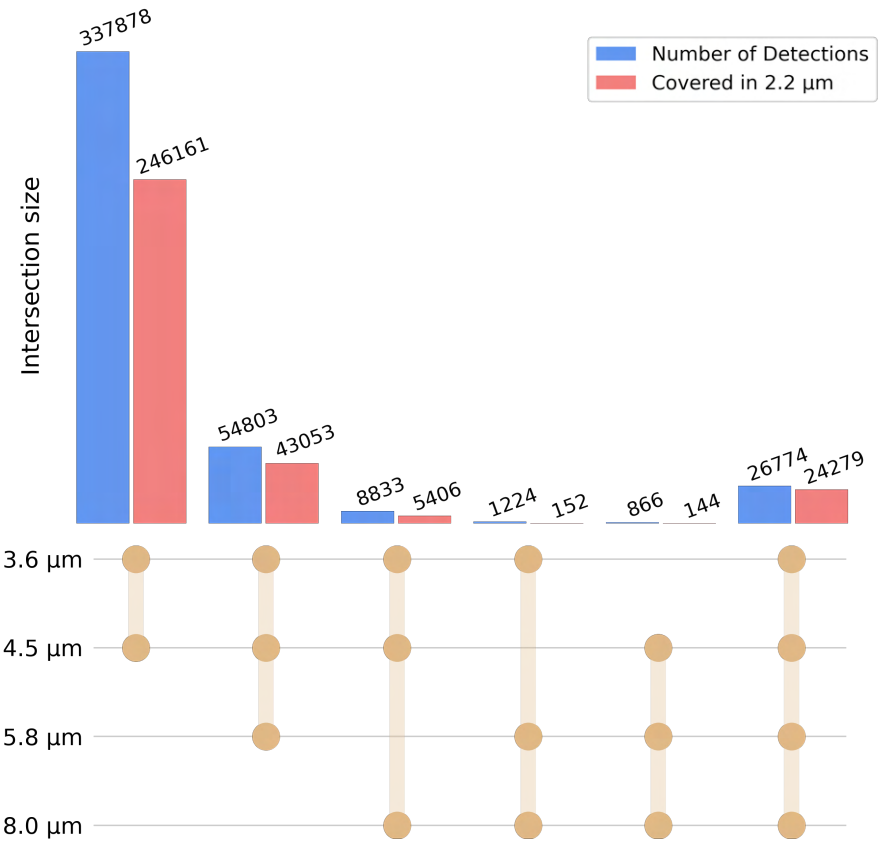

Figure 3.6: Diagram showing the number of detected sources for various combinations of IRAC filters, as well as the subset of those sources also covered by the 2.2 µm K_S filter.

Furthermore, some regions are only covered by specific filters. For instance, IRAC1 and IRAC2 cover a broader area of the Rosette Nebula, as illustrated in Figure 3.1. To better assess the relevant sources, particularly those covered by IRAC, we generated the diagram depicted in Figure 3.6. The diagram illustrates various combinations of IRAC filters. The IRAC filters, namely Channel 1, 2, 3, and 4, correspond to wavelengths of approximately 3.6 µm, 4.5 µm, 5.8 µm, and 8.0 µm, respectively, while the 2.2 µm filter corresponds to the K_S filter. The diagram reveals that nearly 340,000 sources are covered by both IRAC1 and IRAC2 filters but not by IRAC3 and IRAC4. Among these 340,000 sources, approximately 250,000 are also encompassed by the K_S filter. Similarly, only about 27,000 sources are encompassed by all four IRAC filters, with approximately 24,000 of them also covered by the K_S filter.

3.2.2 Completeness

When analyzing the distribution of sources across a range of magnitudes, we anticipate detecting a greater number of sources at fainter magnitudes. This is primarily due to the fact that as we observe the sky in any direction, the number of sources increases with their distance from Earth. However, distant sources appear fainter. And, due to limited exposure time, there exists a magnitude limit beyond which an instrument cannot detect fainter sources. This is called the completeness limit. Determining the completeness limit of a catalogue enables us to ascertain that all sources up to this limit were detected during the observations. The completeness limit for each filter was determined by creating histograms of the frequency distribution of object magnitudes. The peak of the histogram represents the magnitude at which most objects were detected, indicating the completeness limit. For our catalogue, the magnitude value of the completeness limit is listed in Table 3.1 for relevant photometric bands.

Table 3.1: Photometric completeness.

Filter	λ_{eff} [µm]	Completeness [mag]
IRAC4	8.0	15.2
IRAC3	5.8	16.2
IRAC2	4.5	17.1
IRAC1	3.6	17.1
K_S	2.2	17.4
H	1.7	18.0
J	1.2	18.9
y	1.0	19.7
z	0.9	20.3
i	0.8	21.3
r	0.6	21.4
g	0.5	21.8
G_{rp}	0.8	19.2
G	0.6	20.6
G_{bp}	0.5	21.0

The IRAC photometric bands, along with J-, H- and K_S-band, will be used to select YSO candidates in the next chapter. Displayed in Figure 3.7 and 3.8, we have their uncertainties as a function of magnitude, along with the frequency of objects, which were used to determine the completeness magnitude. Taking these figures into acount, along with the values listed in Table 3.1, a cutoff was applied. Photometric data for J, H, K_S, IRAC1 and IRAC2 with uncertainties above 0.2 magnitudes was disregarded. In the same way, photometric data with uncertanties above 0.4 magnitudes in IRAC3 and IRAC4 was disregarded.

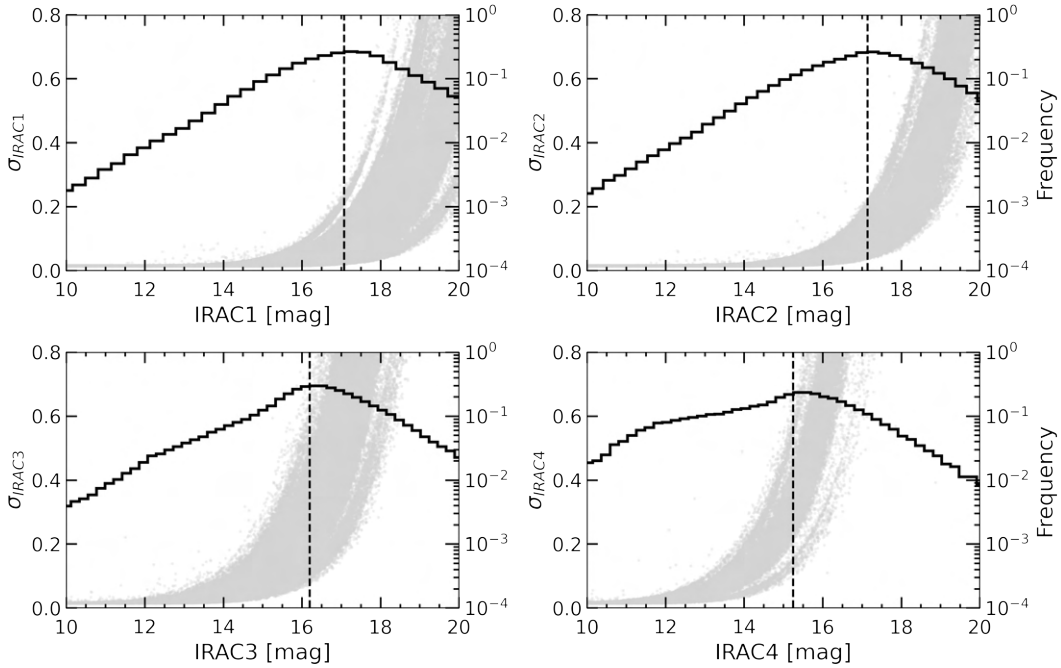

Figure 3.7: The photometric uncertainties as a function of magnitude plotted in gray and the density of sources as a function of magnitude plotted as the black line for all IRAC filters. The dashed black line indicates completeness magnitude for the given filter. For IRAC1 and IRAC2, a bin size of 0.33 mag is used, while for IRAC3 and IRAC4, a bin size of 0.22 mag is applied.

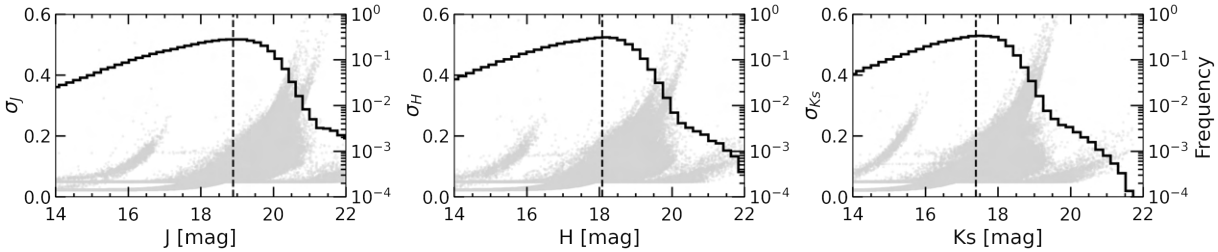

Figure 3.8: The photometric uncertainties as a function of magnitude plotted in gray and the density of sources as a function of magnitude plotted as the black line for J, H, and K_S-bands. The dashed black line indicates completeness magnitude for the given filter. The bin sizes for the J, H, and K_S bands are set to 0.2 magnitudes.

Chapter 4

Candidate Selection

In this chapter, we employ two methods for selecting YSOs, referred to as Tier 1 and Tier 2 selection. Tier 1 is the most reliable method, as it utilizes data from all four IRAC filters. However, because many sources lack photometric data for IRAC3 and IRAC4, we introduce the Tier 2 selection method to expand the number of sources that can be analyzed.

4.1 Tier 1 selection

In this section, we implemented what we refer to as Tier 1 selection of YSO candidates. This selection and classification is partially grounded on the work of Gutermuth et al. (2009) *Phase 1* classification scheme. Additionally, for applicable sources, we also employed an enhanced version of the quasi-stellar objects (QSOs) cutoff proposed by Bouy et al. (2009). Consequently, the Tier 1 selection relies exclusively on sources present in all 4 IRAC photometry bands.

As previously outlined in Section 3.2.2, besides only retaining sources with photometric data across all IRAC filters, we required their photometric uncertainties to be below 0.2 magnitudes for IRAC1 and IRAC2, and below 0.4 magnitudes for IRAC3 and IRAC4. This yields a catalogue containing 22,192 sources.

Going forward, the IRAC photometric filters will often be referred to by their wavelengths in micrometers, following the convention used by Gutermuth et al. (2009). Specifically, IRAC1 will be indicated as [3.6], IRAC2 as [4.5], IRAC3 as [5.8], and IRAC4 as [8.0]. Additionally, the extinction law used to derive the reddening vector in our work is based on the findings of Wang and Chen (2019).

4.1.1 Gutermuth classification

To create a robust sample of YSO candidates (prioritizing purity over completeness), we implemented constraints in different colour spaces to isolate and eliminate several contaminating source types. Then, we selected and classified the YSOs using the remaining sources and their expected position in the colour space.

Initially, we excluded active star-forming galaxies, characterized by their strong polycyclic aromatic hydrocarbon (PAH) feature emission, which results in very red 5.8 and 8.0 μm colours (Stern et al., 2005). To achieve this, we applied the Gutermuth et al. (2009) cuts in the [4.5] − [5.8] vs [5.8] − [8.0] and [3.6] − [5.8] vs [4.5] − [8.0] colour–colour spaces.

Sources are deemed PAH galaxies if they meet all of the following constraints:

$$\begin{aligned} [4.5] &> 11.5 \\ [4.5] - [5.8] &< 1.05 \\ [5.8] - [8.0] &> 1 \\ [4.5] - [5.8] &< \frac{1.05}{1.2} \times ([5.8] - [8.0] - 1). \end{aligned} \tag{4.1}$$

This cut, based on Equation 4.1, is illustrated in Figure 4.1.

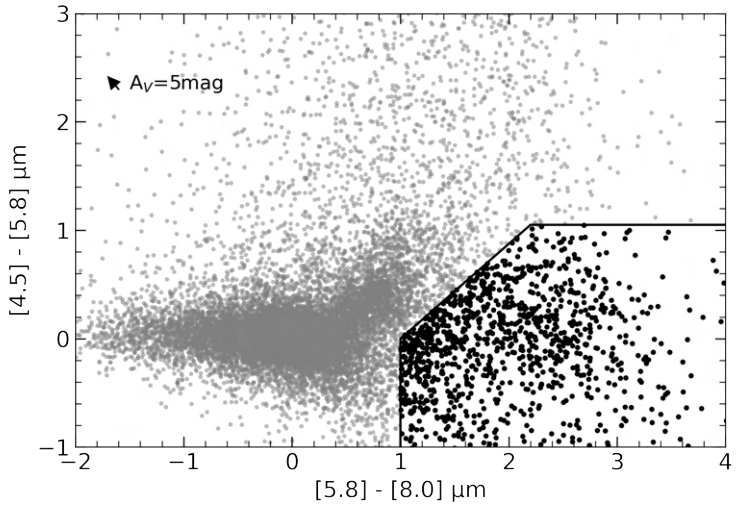

Figure 4.1: The colour–colour diagram employed for isolating and removing unresolved starforming galaxies, represented by filled black circles. An A_V=5 mag reddening vector is represented.

Furthermore, sources are also regarded as PAH galaxies if they cover all of the following constraints:

$$\begin{aligned} [4.5] &> 11.5 \\ [3.6] - [5.8] &< 1.5 \\ [4.5] - [8.0] &> 1 \\ [3.6] - [5.8] &< \frac{1.5}{2} \times ([4.5] - [8.0] - 1). \end{aligned} \tag{4.2}$$

The cut defined by Equation 4.2 is depicted in Figure 4.2.

Once a source has been identified as a PAH galaxy, it is excluded from further consideration in the classification scheme. Given the distinct colour, compared to YSOs, we anticipate minimal residual contamination from these objects in our final sample of YSO candidates.

Subsequently, in the Gutermuth et al. (2009) classification scheme, cutoffs are applied in an attempt to isolate broad-line active galactic nuclei (AGNs). However, these objects exhibit MIR colours that closely resemble those of YSOs (Stern et al., 2005). Moreover, the cutoffs used primarily rely on magnitude, and our catalogue extends nearly 2 magnitudes deeper than the one used by Gutermuth et al. (2009). Performing these cutoffs would probably result in numerous genuine YSOs being overlooked. Therefore, we decided not to apply these cutoffs. Instead, we later (Section 4.1.2) attempted a different method to remove QSOs.

Unresolved knots of shock emission are frequently detected across all IRAC bands, posing another contamination challenge in our YSO samples. Sources displaying photometric characteristics that meet all of the following criteria are likely to be originated from shock emission, and thus were eliminated:

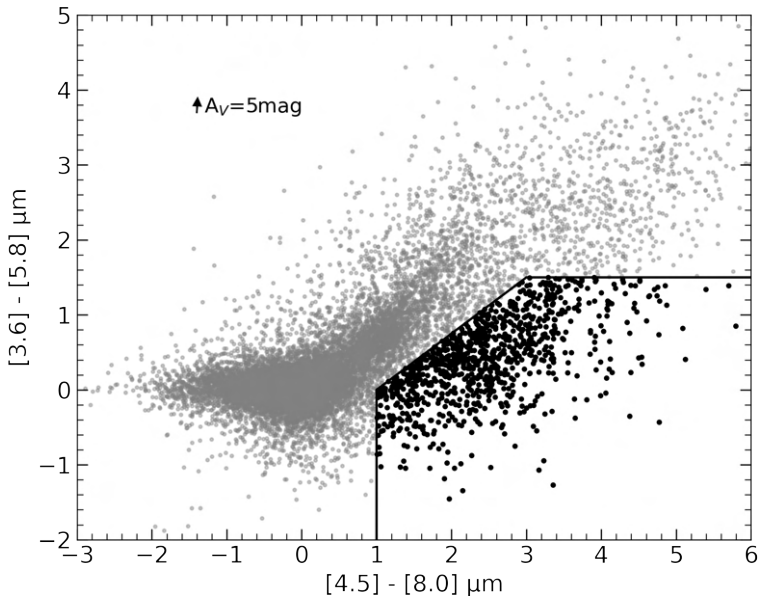

Figure 4.2: The colour–colour diagram employed for isolating and removing unresolved starforming galaxies, represented by filled black circles. An A_V=5 mag reddening vector is represented.

$$\begin{aligned} &[3.6]-[4.5] > \frac{1.2}{0.55} \times (([4.5]-[5.8])-0.3)+0.8 \\ &[4.5]-[5.8] \leq 0.85 \\ &[3.6]-[4.5] > 1.05. \end{aligned} \tag{4.3}$$

Another set of contaminant sources includes cases where resolved structured PAH emission has influenced the photometric apertures of faint field stars. This leads to spurious excess emission in the [5.8] and [8.0] µm bands. Sources that meet all of the following criteria are consistent with having PAH-contaminated apertures:

$$\begin{aligned} \sigma_1 &= \sigma[[4.5]-[5.8]] \\ \sigma_2 &= \sigma[[3.6]-[4.5]] \\ [3.6]-[4.5]-\sigma_2 &\leq 1.4 \times (([4.5]-[5.8])+\sigma_1-0.7)+0.15 \\ [3.6]-[4.5]-\sigma_2 &\leq 1.65. \end{aligned} \tag{4.4}$$

The cuts delineated by Equations 4.3 and 4.4 are illustrated in the left panel of Figure 4.3.

Among the remaining sources in the same colour-colour diagram, we categorize those that satisfy the following criteria as Class I YSOs:

$$\begin{aligned} &[4.5]-[5.8] > 0.7 \\ &[3.6]-[4.5] > 0.7. \end{aligned} \tag{4.5}$$

In the right panel of Figure 4.3 we observe how the constraints are implemented on the dataset. We should note that in exceptional scenarios, a Class II source that is heavily reddened could display colours akin to those of a Class I, as specified in Equation 4.5.

We can now discern Class II YSOs from the surrounding field stars by identifying sources that satisfy the following constraints:

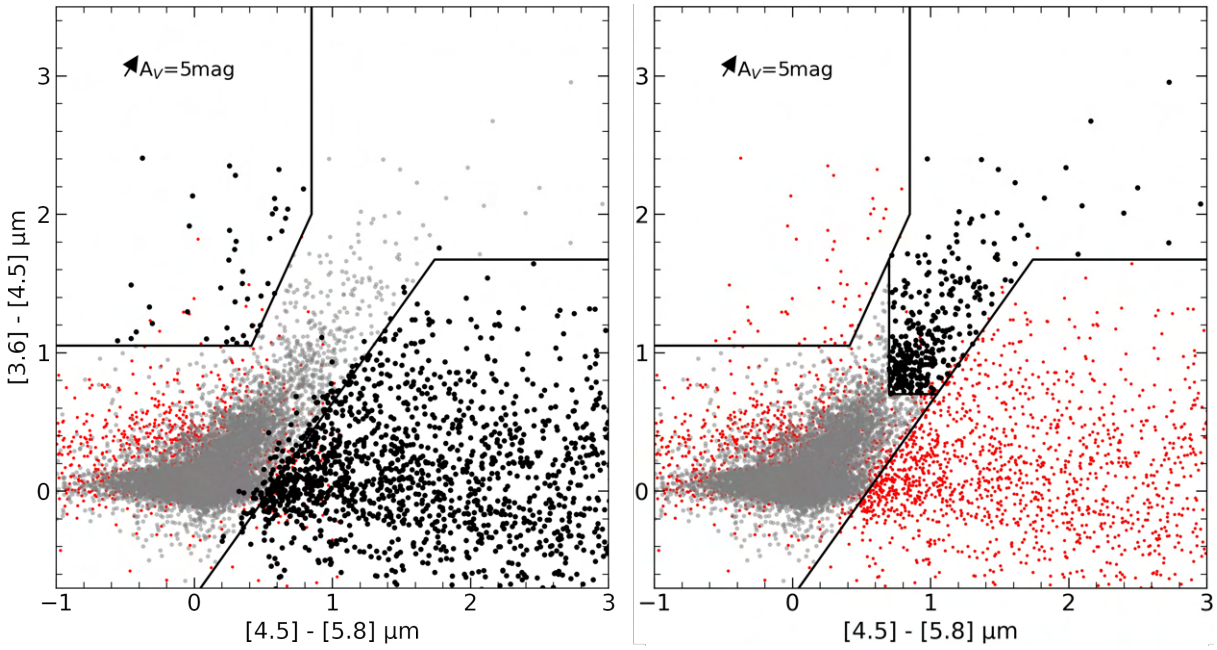

Figure 4.3: The colour-colour diagram in the left panel was utilized to differentiate between unresolved shock emission knots (represented by filled black circles in the top left) and objects impacted by structured PAH aperture contamination (filled black circles in the bottom right). In the right panel, the same colour-colour diagram was employed to isolate Class I YSOs (filled black circles). Additionally, unclassified sources (filled gray circles) are represented, while previously classified sources are not considered (small red dots). An A_V=5 mag reddening vector is represented.

$$
\begin{aligned}
\sigma_3 &= \sigma[[4.5]-[8.0]] \\
\sigma_4 &= \sigma[[3.6]-[5.8]] \\
[4.5]-[8.0]-\sigma_3 &> 0.5 \\
[3.6]-[5.8]-\sigma_4 &> 0.35 \\
[3.6]-[5.8]+\sigma_4 &\leq \frac{0.14}{0.04} \times (([4.5]-[8.0]-\sigma_3)-0.5)+0.5 \\
[3.6]-[4.5]-\sigma_2 &> 0.15.
\end{aligned}
\tag{4.6}
$$

In Figure 4.4, we can see the implementation of the constraints outlined in Equation 4.6 applied to the remaining unclassified sources.

From this analysis, we derived 1,608 Class II YSOs and 326 Class I YSOs.

4.1.2 Quasi-stellar objects (QSOs)

The preliminary result from Section 4.1.1 might still be contaminated with QSOs. To reclassify sources that are likely QSO we used, for the sources that allow it, an enhanced version of the QSOs cutoff proposed by Bouy et al. (2009). This cutoff requires J- and i-band photometry with uncertainties bellow 0.2 magnitudes. The Equation 4.7 shows the condition for a source to be considered a QSO.

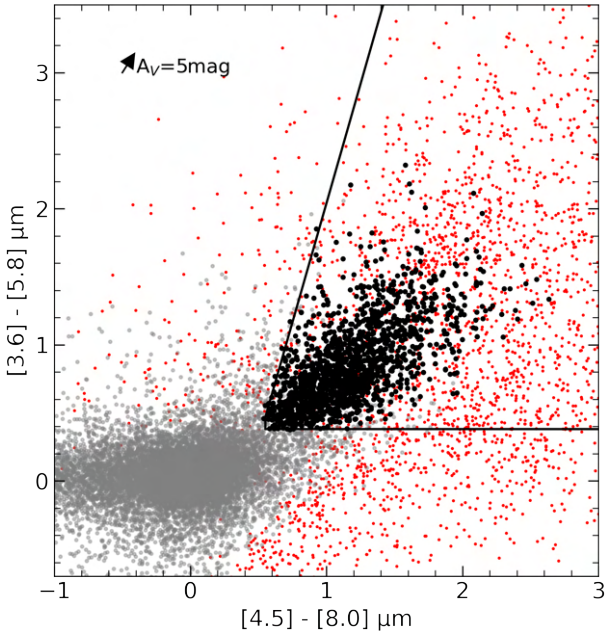

Figure 4.4: The colour–colour diagram employed to isolate Class II YSOs (filled black circles), along with previously unclassified sources (filled gray circles). Previously classified sources are not considered (small red dots). An A_V=5 mag reddening vector is represented.

$$\begin{aligned} \sigma_5 &= \sigma[\mathrm{i}-\mathrm{J}] \\ [3.6] &> 13 \\ \mathrm{i}-\mathrm{J} &\leq 1.5+\sigma_5 \\ \mathrm{i}-\mathrm{J} &< 1.12\times(\mathrm{J}-[3.6])-0.8. \end{aligned} \tag{4.7}$$

The constrains of the Equation 4.7 can be seen in Figure 4.5. The stipulation that the IRAC1 filter's magnitude must be above 13 stems from Wu et al. (2012) study, which analyzed over 37,000 quasars and showed a noticeable rise in quasar detection within the 13 to 14 magnitude range for the WISE (Wide-field Infrared Survey Explorer; Cutri et al. 2021) W1 filter. This observation was extended to the IRAC Channel 1 filter due to its wavelength coverage closely mirroring that of the WISE W1 filter. It is also noteworthy that out of the 22,000 sources identified in the original Tier 1 selection criteria, more than 18,500 sources also meet these additional photometric requirements. However, only 1,189 out of the possible initial 1,934 YSOs could be employed in this analysis.

This QSO cutoff removed potentially misclassified YSOs. A variety of other selection methods exist to isolate broad-line AGNs and QSOs. However, these objects often exhibit MIR colours similar to those of YSOs, making them a significant contaminant. Despite efforts using IRAC colour-colour diagrams, they remain difficult to separate (Stern et al., 2005; Gutermuth et al., 2009; Donley et al., 2012). In the work of Gutermuth et al. (2009), a colour-magnitude diagram is employed to mitigate the contamination from broad-line AGNs, as illustrated for our catalogue in Figure 4.6. As previously stated, the Gutermuth et al. (2009) applied cuts for broad-line AGNs removal primarily rely on magnitude. However, considering that our catalogue extends nearly 2 magnitudes deeper, a considerable number of potential YSOs were being disregarded. Thus, instead of relying solely on magnitude-based criteria, we opted to remove QSOs using the methods outlined in Equation 4.7, as depicted in Figure 4.5.

This yields 1,599 sources classified as YSO Class II and still 326 sources classified as YSO Class I.

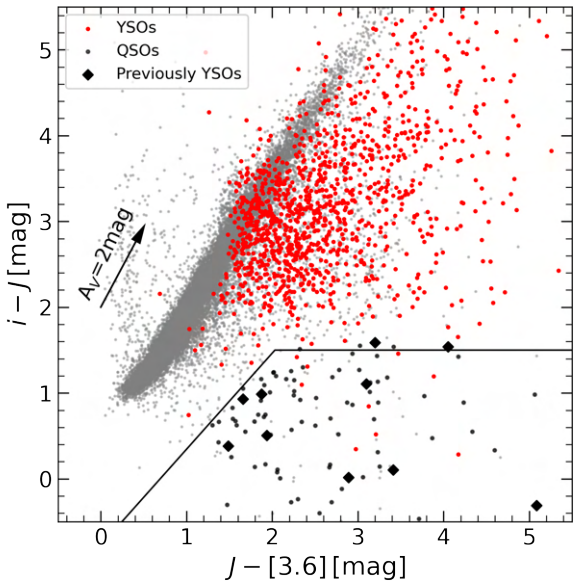

Figure 4.5: The colour-colour diagram serves as the basis for isolating QSOs. In the diagram, objects that were not initially classified as YSOs but are now reclassified as QSOs are represented by black circles. YSOs that have been classified as QSOs are depicted as black diamonds. Objects that were identified as YSOs and remain classified as such are shown in red, while previously unclassified sources are represented by filled gray dots. An A_V=2 mag reddening vector is represented.

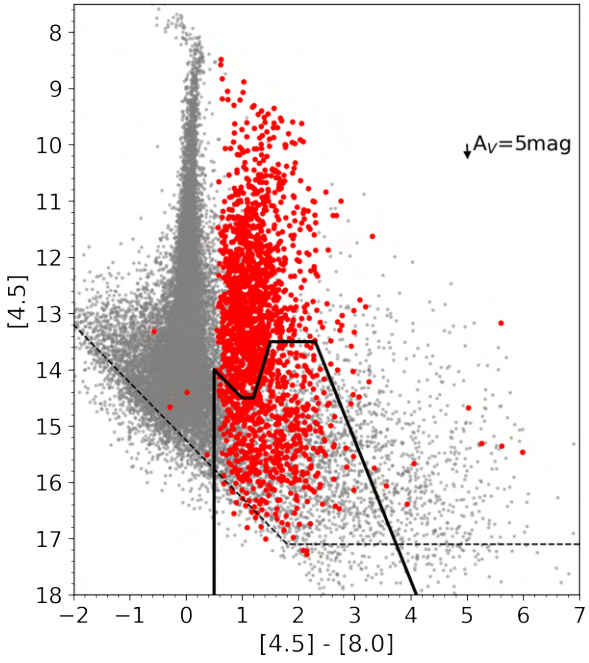

Figure 4.6: The colour-colour diagram utilized in an attempt to differentiate broad-line AGNs by identifying the area below the solid black line. YSO candidates are depicted in red, while other sources are represented by filled gray circles. The dashed line indicates the completeness limit of our catalogue. An A_V=5 mag reddening vector is represented.

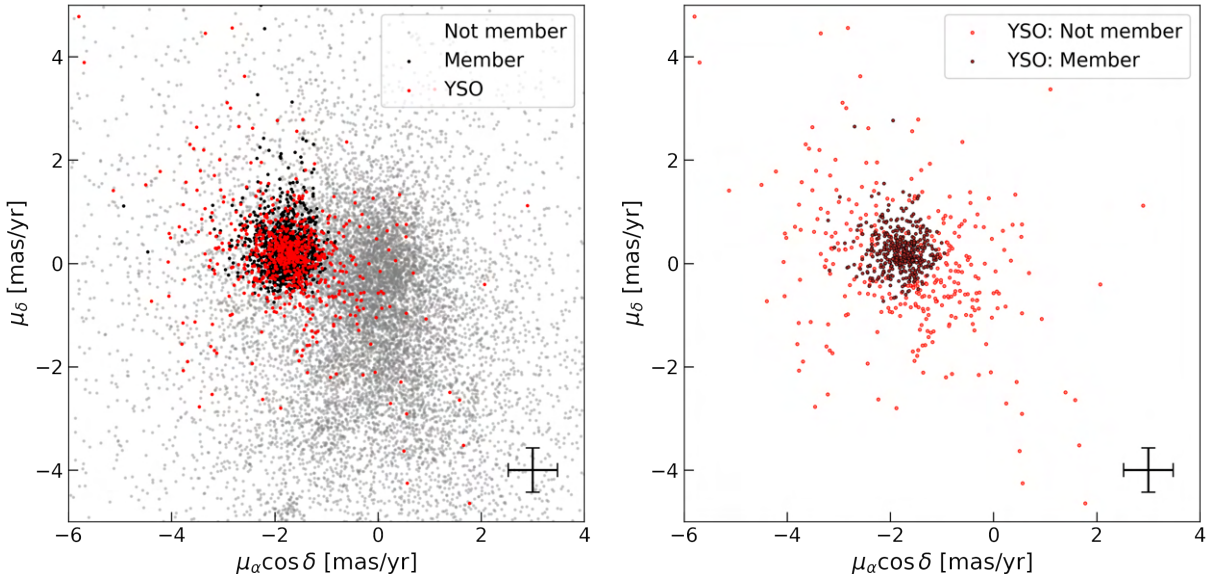

Figure 4.7: Visualization of Gaia EDR3 proper motions with membership probabilities from Mužić et al. (2022). The left panel shows sources identified as members as black dots, non-members as grey dots, and YSO candidates from the Tier 1 selection as red dots. The right panel focuses on the YSO candidates marked in red in the left panel, indicating their membership status, dark red dots represent members, while pale red dots represent non-members. Each panel also details the mean proper motion uncertainty in its lower right corner.

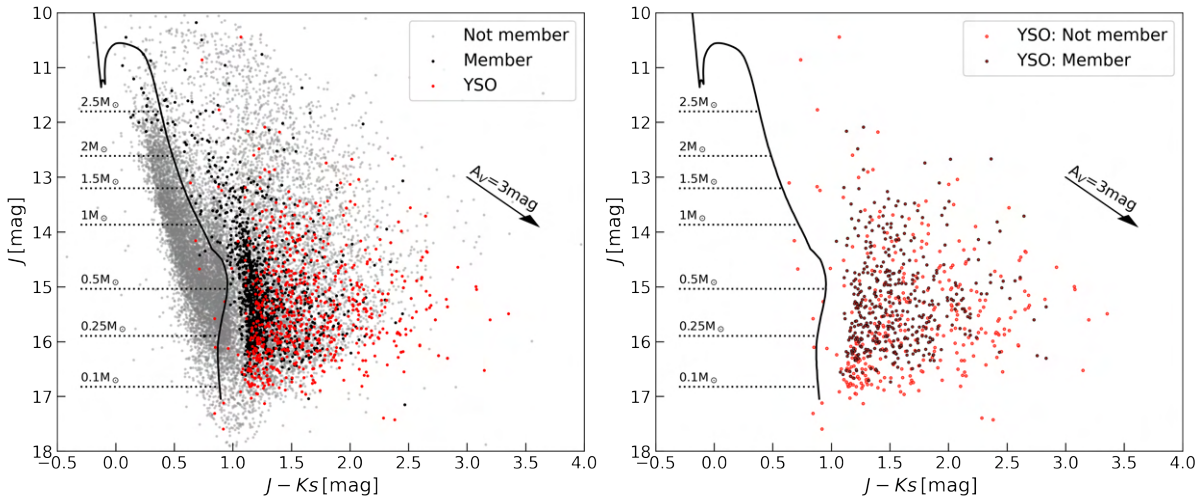

Figure 4.8: Colour-magnitude diagram. The left panel segregates objects into non-YSOs/non-members in gray, non-YSOs/members in black, and YSOs in red. The right panel narrows focus to YSOs, with members in dark red and non-members in pale red. Both panels are augmented with a solid line that shows the 2 Myr PARSEC isochrone (Bressan et al., 2012a; Pastorelli et al., 2020) and an A_V=3 mag reddening vector.

4.1.3 Results

In the previous sections, we gathered a selection of YSO candidates. Our analysis of these YSO candidates begin by referencing the study conducted by Mužić et al. (2022), which utilized a probabilistic random forest algorithm to determine the likelihood of a source being a member of the Rosette Nebula and NGC 2244. By comparing data from both their catalogue and ours, we were able to retrive the membership probabilities values for matching sources. Membership was assigned to sources with at least an

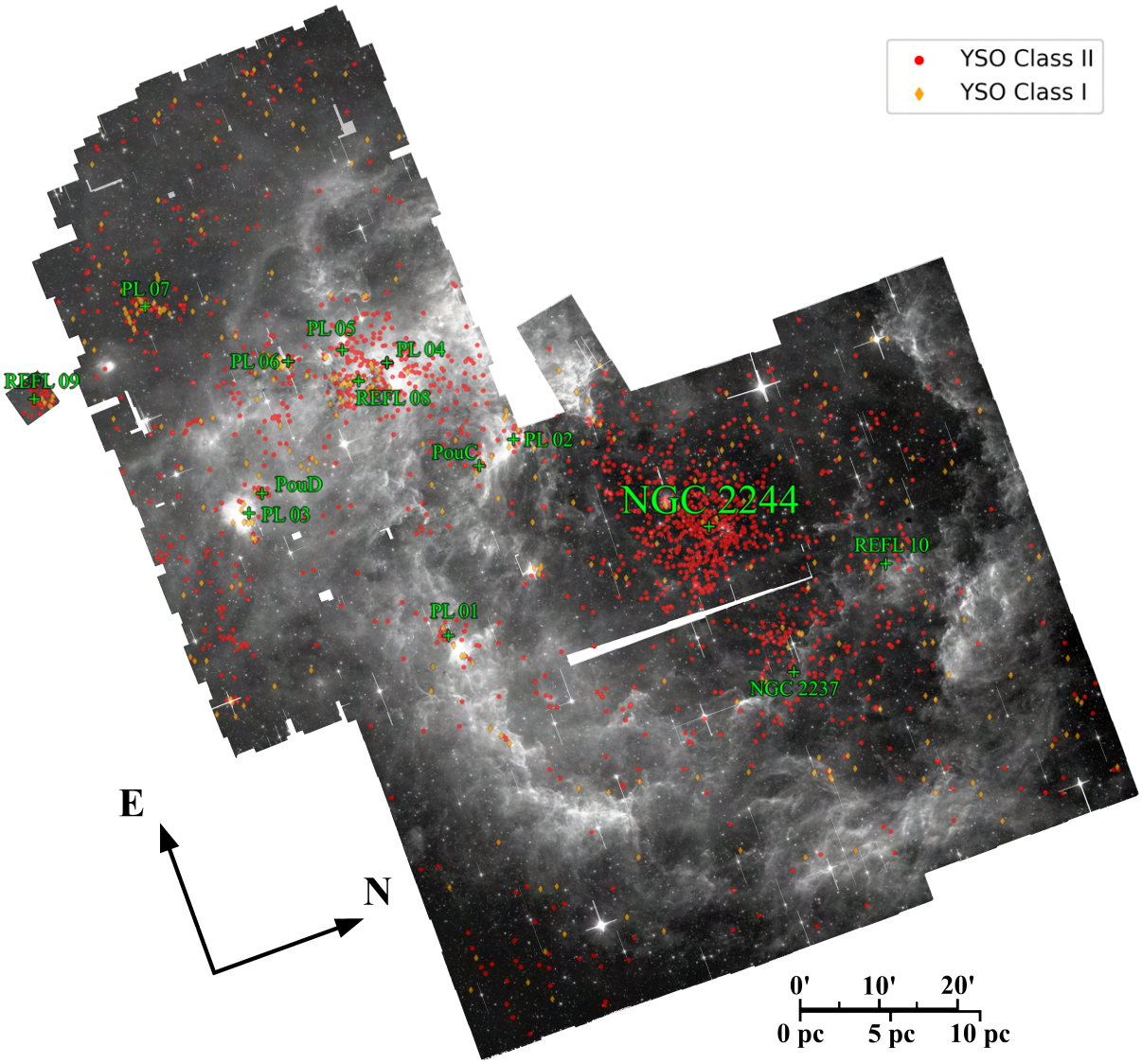

Figure 4.9: Rosette Nebula image overlyed with the locations of Tier 1 YSO candidates, with Class I YSOs marked in orange diamonds and Class II YSOs in red circles. Green crosses denote the positions of young clusters and groups previously identified in the studies by Phelps and Lada (1997); Roman-Zuniga (2006); Poulton et al. (2008); Cambrésy et al. (2013).

80% probability of being members, based on the probabilistic classification determined by Mužić et al. (2022). Therefore, following this work, we classify sources with a membership probability of 80% or higher as members, while those with a probability below 80% are treated as non-members.

Our analysis showed that among the 9 matching sources categorized as YSO Class I, only 2 (22%) were considered members, while the remaining 7 (78%), were non-members. Similarly, out of 774 Class II YSOs evaluated, 438 (57%) were reported as members, and the remaining 336 (43%) were determined to be non-members.

These findings did not align with our initial expectation of a predominant membership. However, we recognize that the methodology used by Mužić et al. (2022) may have a bias towards the optical, which could steer the results. Therefore, to assess the validity of the membership probability for our YSO candidates, we began by visually examining the two-dimensional internal motions of the stars using

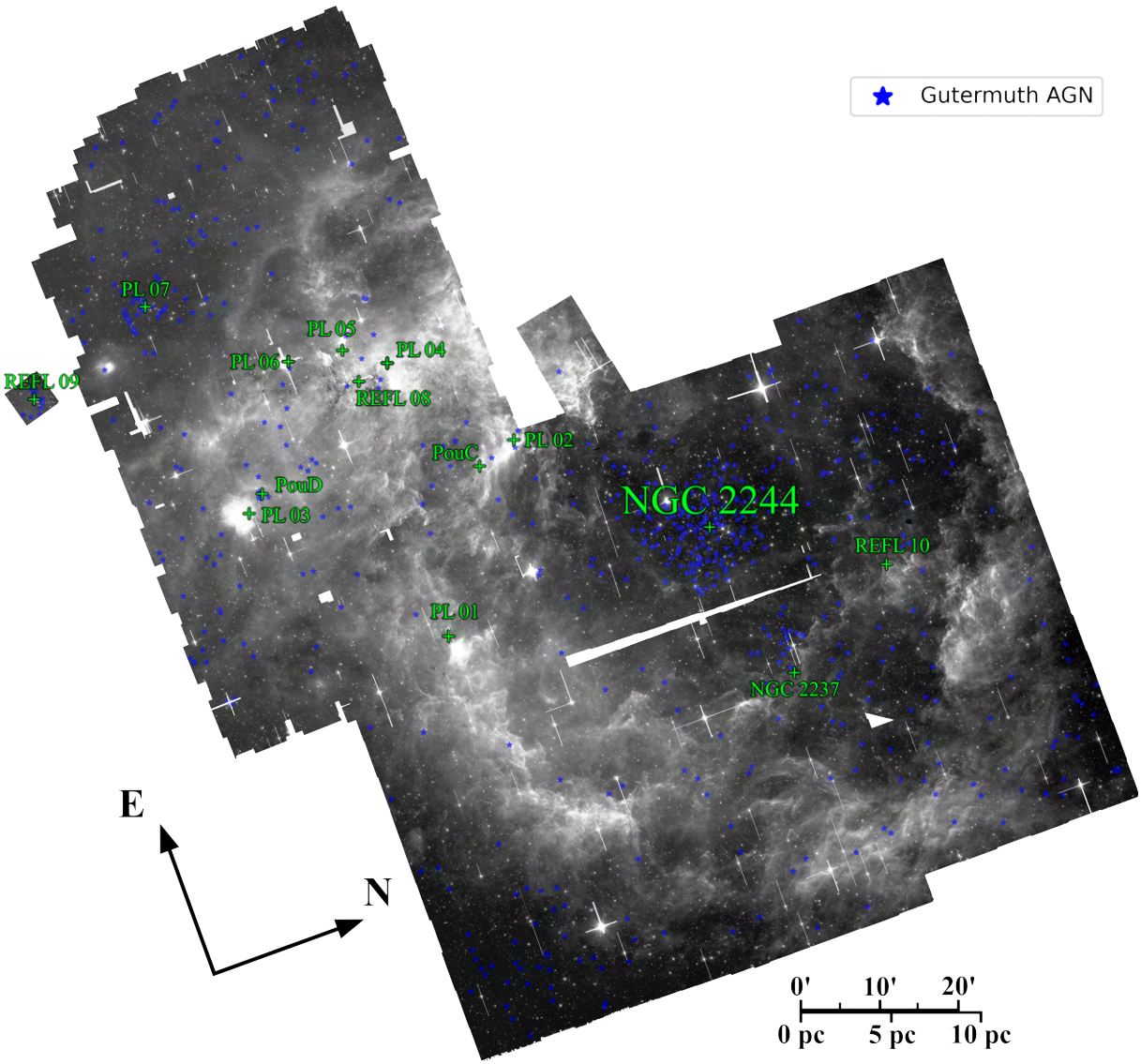

Figure 4.10: Rosette Nebula image overlyed with the locations of Tier 1 YSO candidates, that would have been classified as broadline-AGNs Gutermuth et al. (2009) method depicted by blue stars.

Gaia EDR3 (Gaia Collaboration, 2021) proper motions data. During our review, we noted that, with the exception of a few potential outliers, the sources shared similar proper motion values, taking into account the average uncertainty value. This shared characteristic is clearly visible in Figure 4.7, as these objects are clustered in a consistent area within the proper motion space.

Further inspection revealed that YSO candidates that are non-members and members alike are located in the same region on the colour-magnitude diagram presented in Figure 4.8. This observation led us to determine that the membership probability was biased towards the optical. Concurrently, our examination confirmed that these sources seem to be part of the same collective, affirming our findings.

The Tier 1 YSO candidates distrubution is illustrated in Figure 4.9. This visualization clearly shows that the vast majority of YSO candidates are situated near the locations of young clusters and groups that were identified in earlier research by Phelps and Lada (1997); Roman-Zuniga (2006); Poulton et al. (2008); Cambrésy et al. (2013).

The depiction of the location of all YSOs that would be classified as broadline-AGNs according to the

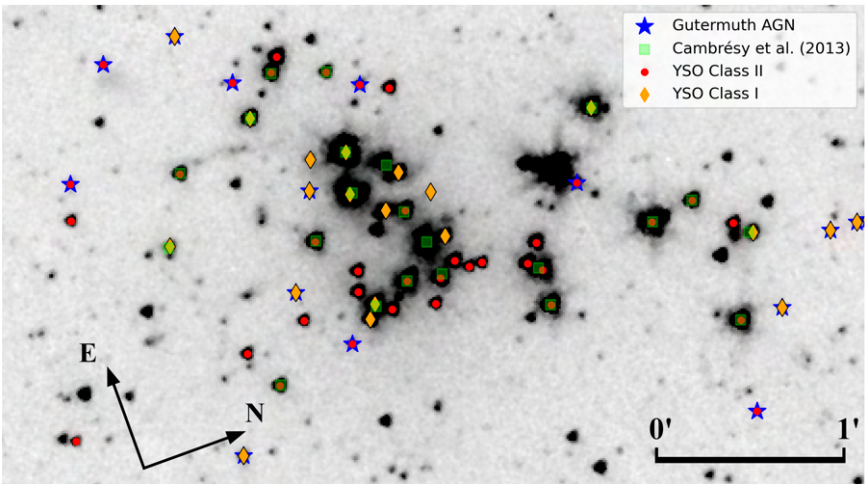

Figure 4.11: YSO distribution in the PL07 Cluster. Class I YSO candidates are marked with orange diamonds and Class II YSO candidates with red circles. Previously identified YSO candidates by Cambrésy et al. (2013) are highlighted with green squares. Additionally, YSOs that would have been classified as broad-line AGNs by the method of Gutermuth et al. (2009) are indicated with blue stars.

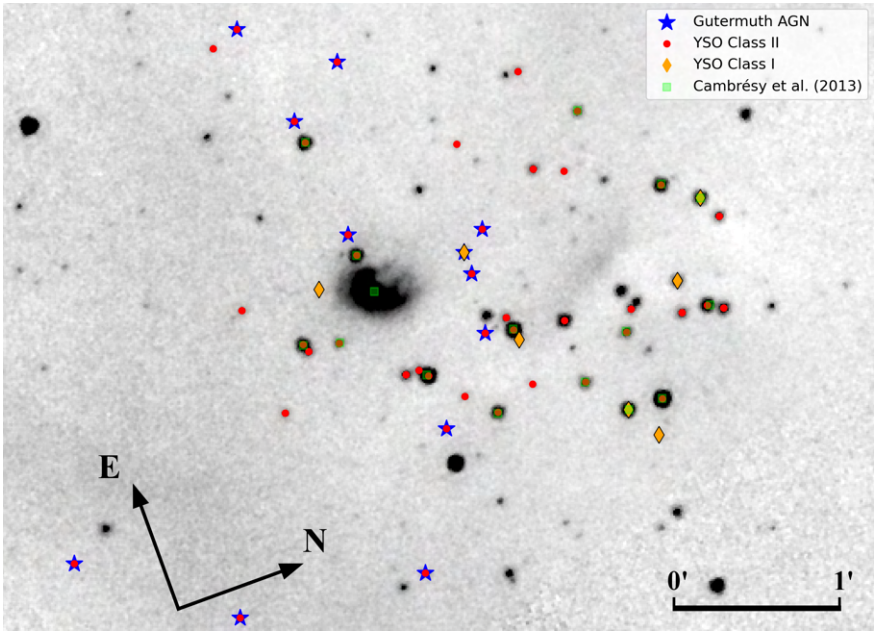

Figure 4.12: YSO distribution in the REFL09 Cluster. Class I YSO candidates are marked with orange diamonds and Class II YSO candidates with red circles. Previously identified YSO candidates by Cambrésy et al. (2013) are highlighted with green squares. Additionally, YSOs that would have been classified as broad-line AGNs by the method of Gutermuth et al. (2009) are indicated with blue stars.

classification method developed by Gutermuth et al. (2009) is shown in Figure 4.10. In Figure 4.11, we examined the PL07 region, which was previously identified in the NEWFIRM mosaics (refer to Figure 2.8). This region contains a high concentration of YSOs, which are displayed and differentiated as Class I and Class II YSOs. We also identified which of these YSOs would have been categorized as broad-line AGNs using the Gutermuth et al. (2009) selection method. Our analysis revealed a significant number of YSOs, specifically, 56 YSOs. Among these, 14 (25%) would have been classified as broad-line AGNs in Gutermuth et al. (2009). Based on this information, it seems more sensible to infer that a significant portion of the YSO candidates in these young clusters are, in fact, genuine YSOs, as opposed to broad-line AGNs. Although broad-line AGNs might occasionally appear in our list of YSO candidates, there

should not exist a correlation between their presence and the proximity to young clusters. Rather, a more uniform distribution across the entire field is expected. This implies that, while some contamination is inevitable, it would be dispersed across the entire field. Consequently, it is a plausible assumption that a YSO that would have been classified as a broad-line AGN that is located near young clusters are, in all likelihood, actual YSOs. Similar things can be seen in other young clusters and groups in the Rosette region, for example in Figure 4.12. In these figures we can see a high density of YSOs located near young clusters and groups that would have been classified as broad-line AGNs. This, once again, corroborates the ideia that most of these are genuine YSOs.

4.2 Tier 2 selection

In this section, we introduce a different selection method, named Tier 2. This selection process was created to tackle the limited FoV and lower magnitude of completeness of IRAC3 and IRAC4. IRAC4 also exhibits a lack of data in dense clusters within bright, compact HII regions. Groups such as PL 01, PL 02, PL 03, PL 05, PL 06, and REFL 08 all show some lack of coverage in IRAC4, with some also experiencing data gaps in IRAC3, though to a lesser extent. (Povich et al., 2013) note that the nebular background emission in IRAC4 is so extreme that it prevents the detection of the majority of point sources across the entire luminosity range. This seems to hold true in our study as well, even when using photometric data from denebulized mosaics, as shown in Figure 4.13, where we still observe a bright halo around the saturated regions with missing data.

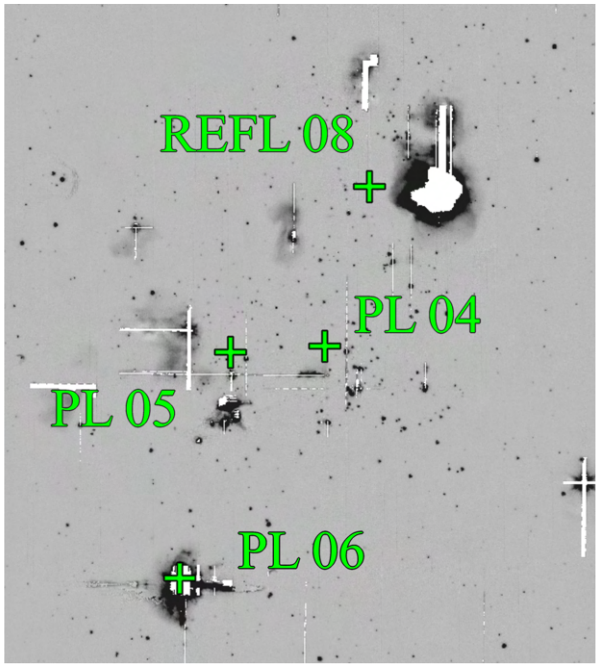

Figure 4.13: Zoomed-in view of the IRAC4 denebulized mosaic, highlighting PL 4, PL 05, PL 06, and REFL 08.

The first phase of the Tier 2 identification and classification of YSOs was done using customized constraints in the colour space based on the positions of sources classified in Tier 1. Consequently, Tier 2 selection is biased by the Tier 1 selection. Despite the latter's proven reliability, we recognize the bias inherent in this approach and the limitations resulting from the absence of IRAC3 and IRAC4 photometric data, which would have facilitated a more accurate selection given their longer wavelengths. In the second phase, we used VOSA (Bayo et al., 2008) to derive the extinction (A_V) and the effective temperature

(T_{eff}), which allows us to create an Hertzsprung-Russell (HR) diagram and estimate the ages of the sources selected in the first phase. Sources younger than 10 Myrs were retained as Tier 2 YSO candidates.

The Tier 1 selection criteria were applied to a dataset of just over 22,000 sources. In contrast, the Tier 2 criteria enabled the analysis of a significantly larger dataset comprising more than 273,000 sources. Similar to Tier 1, the Tier 2 selection mandates that the photometric uncertainties for IRAC1 and IRAC2 must be less than 0.2 magnitudes. Additionally, it incorporates J-, H-, and K_S-band photometric data, that also required these bands to have uncertainties below 0.2 magnitudes.

4.2.1 Tier 2 phase 1: colour-colour diagrams

The first colour-colour diagram we used is presented in Figure 4.14. Based on the distinct area occupied by Tier 1 YSO candidates within this diagram, we formulated Equation 4.8. This equation serves as a criterion to exclude sources located outside the clearly defined region associated with YSO candidates. This process narrows down our pool of potential YSOs by removing likely non-YSO entities. Sources meeting any of the criteria outlined in Equation 4.8 were excluded from further analysis.

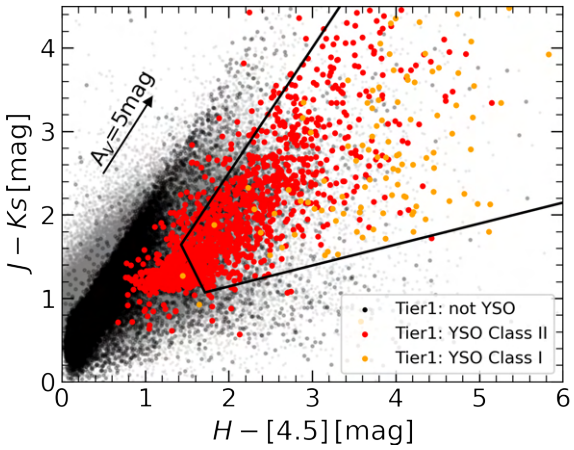

Figure 4.14: The colour-colour diagram was used to identify and eliminate most contaminants from the catalogue. YSO candidates from Tier 1 are depicted in red and orange circles for Class II and Class I, respectively. An A_V=5 mag reddening vector is represented. The black lines represent the criterion defined in Equation 4.8.

$$\begin{aligned} &\mathrm{J}-\mathrm{K}_S > -0.5 + 1.5 \times (\mathrm{H}-[4.5]) \\ &\mathrm{J}-\mathrm{K}_S > 4.5 - 2 \times (\mathrm{H}-[4.5]) \\ &\mathrm{J}-\mathrm{K}_S < 0.65 + 0.25 \times (\mathrm{H}-[4.5]). \end{aligned} \tag{4.8}$$

In this colour-colour diagram, a strict cutoff was implemented to substantially minimize contamination from non-YSOs. As shown in Figure 4.14, there is a noticeable area with a high density of Tier 1 Class II YSO candidates outside the clearly defined region. This was done intentionally to exclude most contaminants, as this area is in close proximity to the Tier 1 non-YSOs.

Following this, we produced the colour-colour diagram displayed in Figure 4.15. Observing the area occupied by Tier 1 YSO candidates led us to develop Equation 4.9. Any sources that satisfied at least one of the conditions laid out in Equation 4.9 was excluded from further analysis.

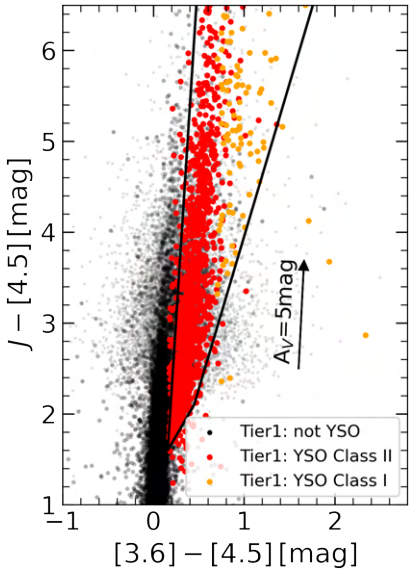

Figure 4.15: The colour-colour diagram used to identify and eliminate potential contaminants from the catalogue. YSO candidates from Tier 1 are depicted in red and orange circles for Class II and Class I, respectively. An A_V=5 mag reddening vector is represented. The black lines represent the criterion defined in Equation 4.9.

$$\begin{aligned} \mathrm{J}-[4.5] &> -\frac{8}{9} + 16 \times ([3.6]-[4.5]) \\ \mathrm{J}-[4.5] &< \frac{4}{3} + 1.7 \times ([3.6]-[4.5]) \\ \mathrm{J}-[4.5] &< 0.6 + \frac{10}{3} \times ([3.6]-[4.5]). \end{aligned} \tag{4.9}$$

Furthermore, we created the colour-colour diagram shown in Figure 4.16. By examining the specific area taken up by Tier 1 YSO candidates, we devised Equation 4.10. Sources that met the criteria described in Equation 4.10 were then excluded from further analysis.

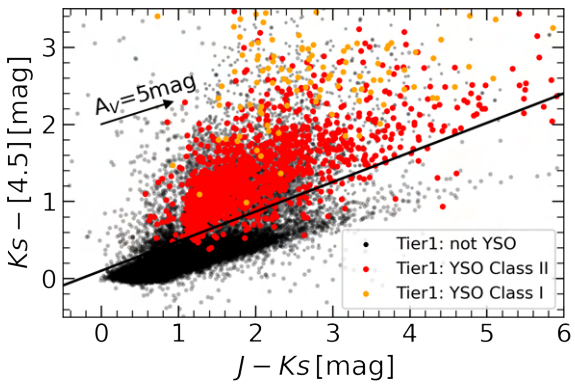

Figure 4.16: The colour-colour diagram was utilized to remove possible contaminants from the catalogue. Tier 1 YSO candidates are marked with red and orange circles for Class II and Class I, respectively. An A_V=5 mag reddening vector is represented. The black lines represent the criterion defined in Equation 4.10.

$$\mathrm{K}_S - [4.5] < 0.1 + 0.38 \times (\mathrm{J}-\mathrm{K}_S). \tag{4.10}$$

Moreover, we created the colour-colour diagram depicted in Figure 4.17. By identifing the distinct area occupied by Tier 1 YSO candidates, we formulated Equation 4.11. Any sources that fulfilled any of the conditions outlined in Equation 4.11 was excluded from further analysis.

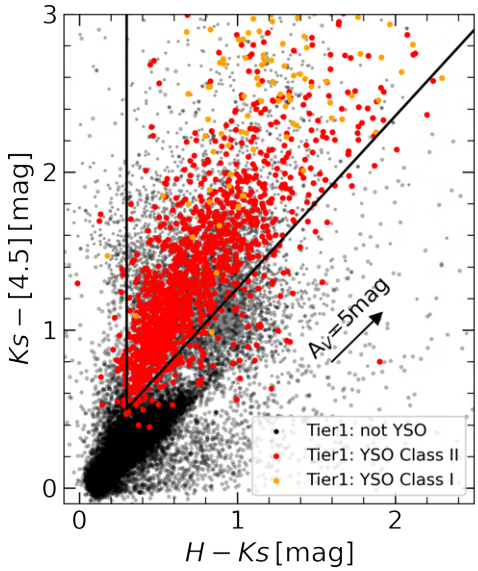

Figure 4.17: The colour-colour diagram used to remove potential contaminants from the Tier 2 catalogue. Tier 1 YSO candidates are marked with red and orange circles for Class II and Class I, respectively. An A_V=5 mag reddening vector is represented. The black lines represent the criterion defined in Equation 4.11.

$$\begin{aligned} \mathrm{H} - \mathrm{K}_S &< 0.3 \\ \mathrm{K}_S - [4.5] &< \frac{1}{6} + 1.1 \times (\mathrm{H} - \mathrm{K}_S). \end{aligned} \tag{4.11}$$

Once more, following the same procedure as the one used for eliminating QSOs during the Tier 1 process, we applied Equation 4.7 to remove QSOs, as illustrated in Figure 4.18.

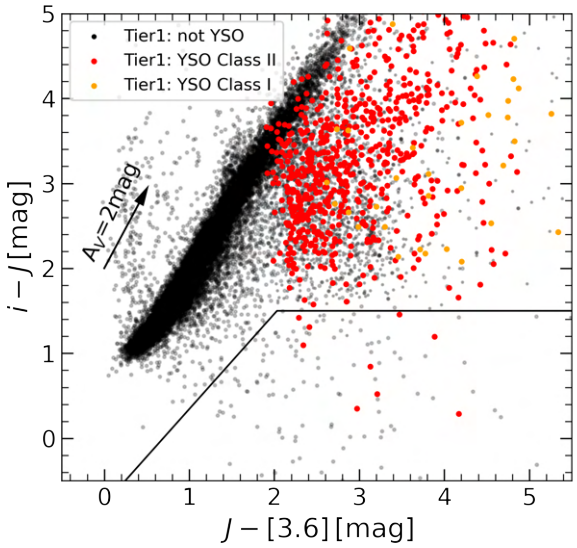

Figure 4.18: The colour-colour diagram used to isolating and remove QSOs. An A_V=2 mag reddening vector is represented.

Lastly, we produced the colour-colour diagram presented in Figure 4.19. First, we excluded sources that meet the criteria outlined in Equation 4.12.

$$\begin{aligned} \mathrm{H} - \mathrm{K}_S &< -0.35 + \frac{5}{3} \times ([3.6] - [4.5]) \\ \mathrm{H} - \mathrm{K}_S &< 0.65 \end{aligned} \tag{4.12}$$

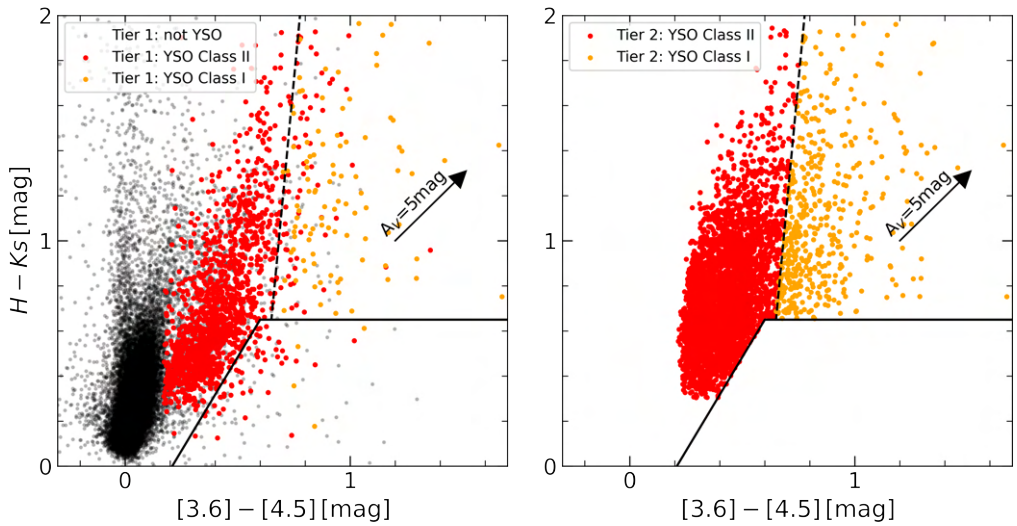

Figure 4.19: The left and right panels show a color-color diagram used to filter contaminants (solid black line) and classify remaining sources as Class I or Class II YSO candidates (dashed line). The left panel displays Tier 1 sources, while the right panel shows Tier 2 sources. The remaining Tier 2 sources left of the dashed line are possible Class II YSO candidates, and those to the right are possible Class I YSO candidates. The solid black line is defined by Equation 4.12, and the dashed line by Equation 4.13. An A_V=5 mag reddening vector is represented.

The remaining sources were then classified into Class I and Class II based on their positioning in relation to Equation 4.13; objects located to the right were designated as Class I, while those to the left are categorized as Class II. This method of distinguishing YSO classes is akin to the approach taken by Koenig and Leisawitz (2014), given the similarity between WISE1 and WISE2 photometric filters to IRAC1 and IRAC2.

$$\mathrm{H} - \mathrm{K}_S > -5.8 + 10 \times ([3.6] - [4.5]) \tag{4.13}$$

The results from the first phase of the Tier 2 selection process identified 3,714 Class II YSOs, out of which 780 were also categorized as YSO candidates in the Tier 1 selection, and 334 were not considered YSOs. Additionally, 491 Class I YSOs were identified, with 167 of these also recognized as YSOs in the Tier 1 selection, while 32 were not classified as YSOs. Sources catalogued as non-YSOs in the Tier 1 classification were excluded from further analyses.

4.2.2 Tier 2 phase 2: Hertzsprung–Russell diagram

In this section, we used VOSA (Virtual Observatory SED Analyzer[1]; Bayo et al. 2008), a software tool designed to analyze SEDs from celestial objects, with the goal of decontaminating the Tier 2 selected sources. Using the T_{eff} and A_V values obtained from VOSA for each source, we created an HR diagram to identify and select sources that appear younger than 10 Myr. Considering that the bulk of star formation in the Rosette Nebula region is expected to have taken place around 2 Myr ago, we concluded that stars exceeding the 10 Myr age threshold were likely contaminants.

This process was conducted in parallel with the examination of Tier 1 YSO sources, which had been proven reliable and served as a control sample. This control group also allowed us to check if the results we obtained were consistent with our expectations.

We began by gathering the Tier 1 and Tier 2 YSO candidates and their magnitudes in the relevant

[1] http://svo2.cab.inta-csic.es/svo/theory/vosa/

photometric filters, listed in Table 3.1. Using Equation 4.14, we calculated the flux values from those magnitudes, along with their uncertainties by error propagation.

$$F = f_0 \times 10^{-0.4 \times m}, \tag{4.14}$$

where F represents the flux value, m the magnitude, and f_0 the zero-point flux calculated for each filter. The latter values were retrieved from the SVO Filter Profile Service[2] (Rodrigo et al., 2012; Rodrigo and Solano, 2020).

The Tier 1 and Tier 2 YSO candidates were entered into VOSA, along with the fluxes for the previously mentioned filters and their uncertainties. Additionally, we allowed the A_V to range between 0 and 20 mag. We used the BT-Settl (CIFIST) model (Caffau et al., 2011), allowing the log(g) to range from 3.5 to 5 and the T_{eff} from 2000 to 7000 K, to fit our SEDs. Figure 4.20 shows a selection of SEDs obtained with VOSA.

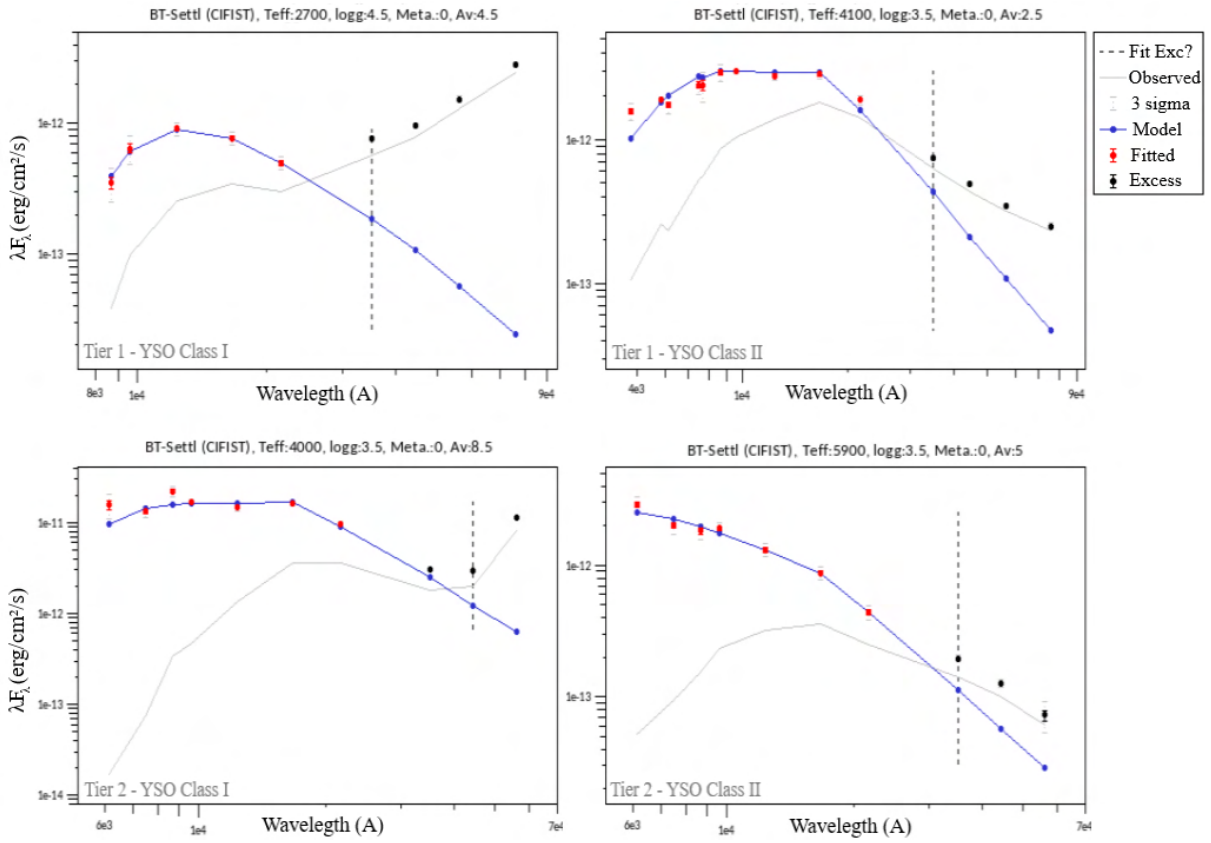

Figure 4.20: In this figure, we see the SED for YSOs. The top panels represents Tier 1 YSOs, with Class I on the left and Class II on the right. The bottom panels represent Tier 2 YSOs, again with Class I on the left and Class II on the right. The SEDs show a gray line generated by VOSA based on the provided photometric data. A fitted model in blue is overlaid, with data points displayed in red and black. The black points indicate areas with excess emission, which is typical for both Class I and Class II YSOs. The excess is noticeable from the data points after the dashed line. Expected values for these points with excess are plotted over the blue line, which represents the fitted model for the hot central protostar. These four SEDs exhibit the typical characteristics associated with their respective YSO classes.

If there are enough photometric data points without excess, VOSA can fit an SED model similar to those shown in Figure 4.20. VOSA's output also included the A_V and the T_{eff} of the central body, along

[2] http://svo2.cab.inta-csic.es/theory/fps/

with the associated uncertainties. Given the distance to the Rosette Nebula, the output parameters, the J magnitude and its relative extinction value of 0.243 (Wang and Chen, 2019), we computed the absolute magnitude, M_J, using the Equation 4.15.

$$M_J = J - 0.243 \times A_V - 5 \times \log(1500) + 5. \tag{4.15}$$

With M_J and T_{eff}, we constructed two HR diagrams. The first HR diagram, for Tier 1 YSO candidates, is shown in the top panel of Figure 4.21. The second HR diagram, for Tier 2 YSO candidates, is shown in the bottom panel of Figure 4.21. Note that some YSO candidates might appear in both diagrams, indicating that they meet the criteria for both Tier 1 and Tier 2.

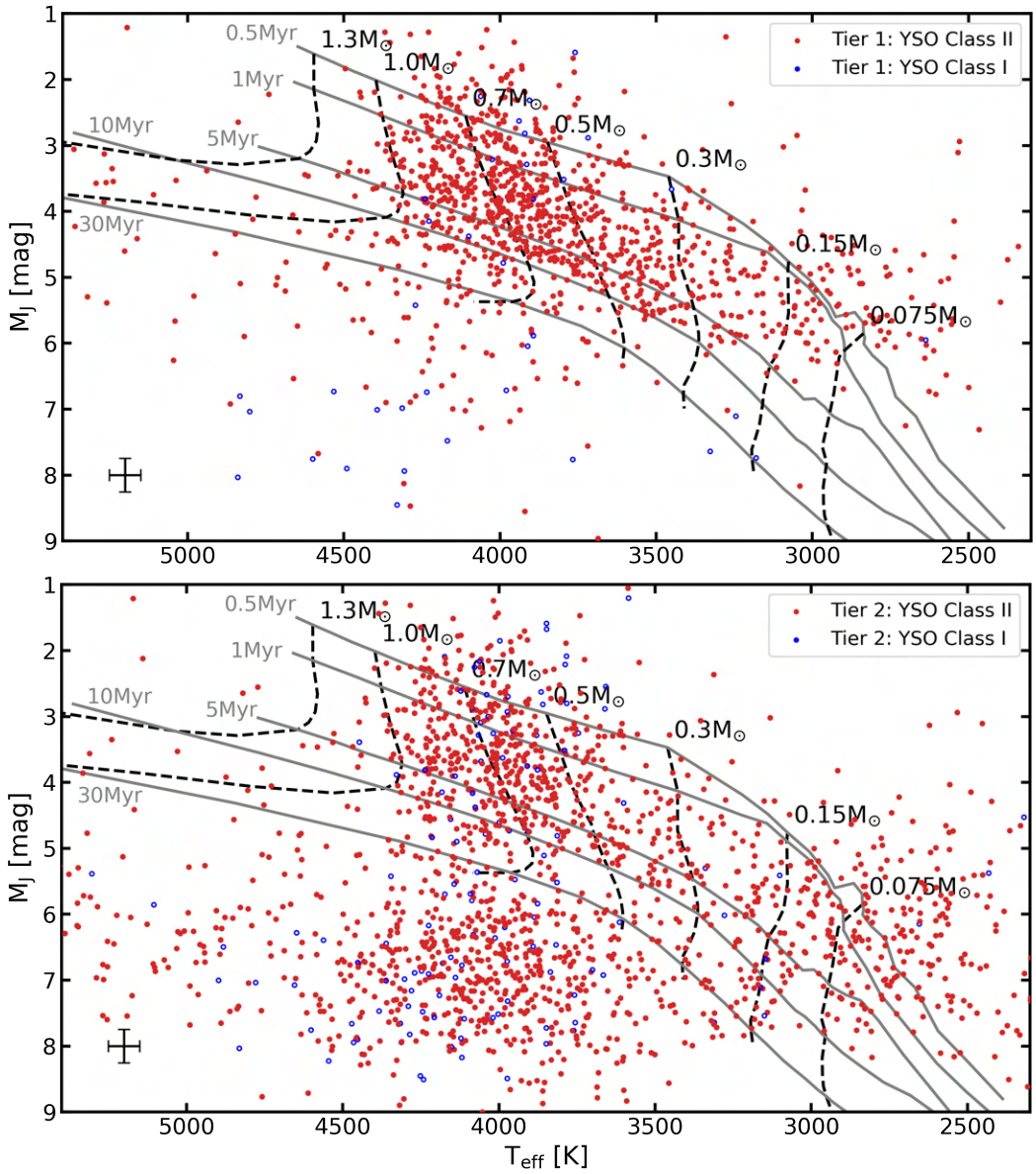

Figure 4.21: The Hertzsprung-Russell diagram illustrates the Class I and Class II YSO candidates. The top panel displays YSOs selected via the Tier 1 method, while the bottom panel depicts those selected via the Tier 2 method. The isochrones (gray solid lines) and lines of constant mass (dashed black lines) are from the BHAC15 series. A representative error bar is depicted in the lower left corner.

A small random uncertainty was added to the T_{eff} values in Figure 4.21 to improve readability. This adjustment addresses the issue of data points clustering due to the BT-Settl (CIFIST) model being

described using discrete values. Despite this adjustment, a typical error bar in the lower-left corner reflects the uncertainty, which exceeds the random uncertainty introduced.

We only consider sources within the T_{eff} range covered in Figure 4.21, as this is where the majority of data points are concentrated. Values outside this range tend to be more sporadic, and those near the model's limit are not reliable. Since they are likely artifacts of modeling attempts, suggesting they don't represent trustworthy fits. Therefore, all values outside this specified range were disregarded from the analysis.

In these HR diagrams, we overlaid the BHAC15 evolutionary tracks (Baraffe et al., 2015), which cover ages ranging from 0.5 to 30 Myrs. Most of the objects classified as Tier 1 have ages below 10 Myrs, which supports the reliability of our Tier 1 selection method. However, for the sources in Tier 2, the age distribution is broader, with many sources falling well below the 30 Myr line, suggesting the presence of contaminants.

Examining the position of Class I and Class II objects in the HR diagram, we do not observe a clear pattern, even though Class I YSOs are known to be younger. Some Class I YSOs appear to be older than 10 Myrs, even though their estimated age should be closer to 0.1 Myrs. This could suggest a high level of contamination among Class I YSOs, but this is unlikely because Class I YSOs have a distinct position in colour-colour diagrams. The same cannot be said for Class II YSOs, as field stars or extragalatic sources may sometimes occupy similar positions, particularly within the Tier 2 classification method.

An alternative explanation for the inconsistency in the position of Class I YSOs in the HR diagram is that these objects are still surrounded by a dense envelope of gas and dust. The dust grains within this envelope may differ from those found in the ISM. Since VOSA uses a general ISM extinction law, this approach is likely inappropriate for these environments. The discrepancy in dust type and size could lead to poor fits being modeled, as it does not account for the unique envelope structure characteristic of Class I YSOs.

The results derived from the HR diagram are presented in Table 4.1. This table shows sources in Tier 1, Tier 2, and New Tier 2, with the latter including sources exclusive to Tier 2 and not found in Tier 1. For each category, the table lists the number of sources that are younger than 10 million years, older than 10 million years, those with unreliable fits (falling outside the suitable T_{eff} range), and those without any fit.

Table 4.1: Hertzsprung-Russell diagram results from VOSA.

	Tier 1	Tier 2	New Tier 2	Total
Younger than 10 Myrs	947	902	350	1297
Older than 10 Myrs	192	835	720	912
Unreliable fit	147	460	362	509
No fit	639	1642	1460	2099

From the Table 4.1, we concluded that a lot of the New Tier 2 sources were likely contaminants. Since the majority of New Tier 2 with a VOSA fit were older than the 10 Myrs. As a result, we have excluded not only Tier 2 Class II sources older than 10 Myrs, but also those that do not possess a fit or have an unreliable fit. On the other hand, Tier 2 Class I sources, whether they were younger than 10 Myrs or not, were retained. These sources occupy a distinct position in the colour space, so contamination is less likely.

This led to the removal of 2,270 Tier 2 Class II YSO candidates from the original 3,714. The remaining

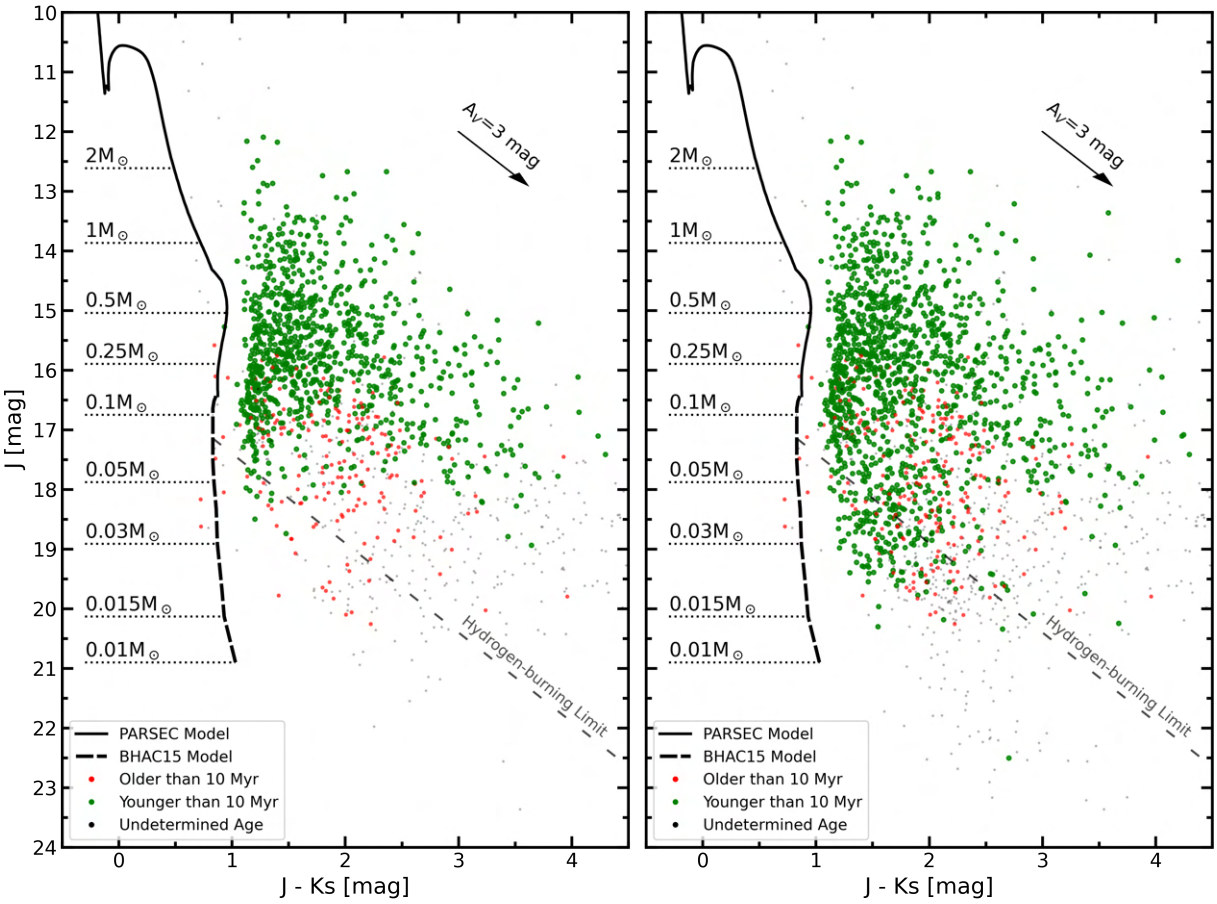

Figure 4.22: The colour-magnitude diagram illustrates the findings from the HR diagram. The left panel shows Tier 1 results, while the right panel is for Tier 2. YSOs under 10 Myrs old (green dots), older than 10 Myrs (red dots), and sources with indeterminate ages (gray dots) are indicated. The 2 Myrs PARSEC (Bressan et al., 2012b; Prisinzano et al., 2019) model isochrone is shown as a solid black line, and the 2 Myrs BHAC15 (Baraffe et al., 2015) model as a dashed black line. The gray dashed line indicates the Hydrogen-burning limit, objects below this are classified as substellar. An A_V=3 mag reddening vector is represented.

YSO candidates are displayed in a colour-colour diagrams in Figure 4.22. The left panel displays the Tier 1 YSO candidates, while the right panel shows the Tier 2 YSO candidates.

Referring again to the study by Mužić et al. (2022), which evaluated the likelihood of sources being members of the Rosette Nebula and NGC 2244, membership was assigned to sources with a probability of 80% or higher. Sources meeting this threshold were classified as members, while those below 80% were considered non-members. In our analysis of Tier 2 selected YSO candidates, we found that among 26 matching sources classified as YSO Class I, only 6 (23%) were identified as members, with the remaining 19 (77%) categorized as non-members. For the 398 Class II YSOs, 241 (61%) were classified as members, while 152 (38%) were non-members. This represents a slight improvement compared to Tier 1 selected sources. This improvement is likely due to a reduced influence of the member selection bias discussed by Mužić et al. (2022), although the higher presence of contaminants in the Tier 2 selection still keeps the membership percentage relatively low.

We identified a total of 2547 YSO candidates, with 1925 originating from Tier 1 and 1311 from Tier 2. There is some overlap among YSO candidates across tiers. The distribution of YSO candidates between Tier 1 and Tier 2, as well as between Class I and Class II, is clearly illustrated in Table 4.2.

Table 4.2: Breakdown of YSO candidates by tier and class.

	Tier 1	Tier 2	New Tier 2
Class I	326	459	292
Class II	1599	852	330
Total	1925	1311	622

4.3 Substellar population

In the previous section, we identified 120 brown dwarf mass objects with SED fits corresponding to ages younger than 10 Myrs. In this section, our aim is to reevaluate lower mass objects that did not appear younger than 10 Myrs, meaning sources that either appeared older than 10 Myrs, lacked a fit, or fell outside the analyzed T_{eff} range. This aproach is similar to the second phase of the Tier 2 selection (4.2.2). However, we allowed T_{eff} to range from 1200 to 4000 K, which is lower than the 2000 to 7000 K range used in phase 2 of the Tier 2 selection method, because low-mass objects have lower temperatures. Previously, in Tier 2, we only considered temperatures above 2350 K to avoid being too close to the 2000 K model limit. By allowing lower temperatures, we can now include sources with temperatures closer to 2000 K, that were previously excluded. Additionally, by selecting a lower maximum temperature, we can re-evaluate sources that were previously misfit with high temperatures. As mentioned earlier, sources with temperatures beyond the range analyzed in Figure 4.21, appeared sporadic and are likely unreliable fits and not genuine high temperature sources.

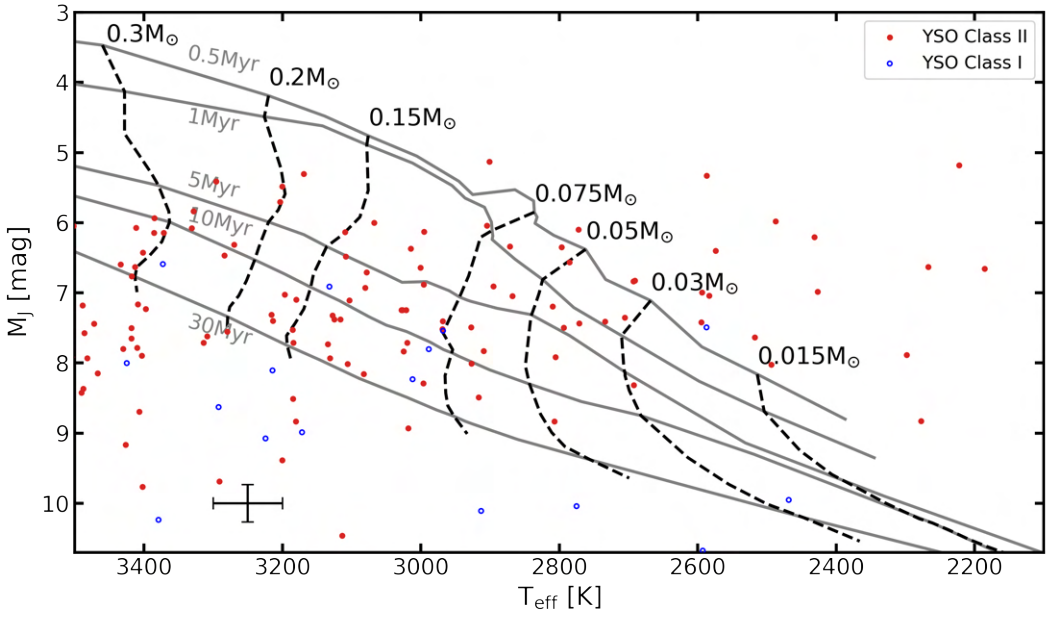

Figure 4.23: The Hertzsprung-Russell diagram illustrates the Class I and Class II YSO candidates with low masses. The isochrones (gray solid lines) and lines of constant mass (dashed black lines) are from the BHAC15 series. A representative error bar is depicted in the lower left corner.

Furthermore, we used the deep photometric data from HAWK-I (Casali et al., 2009) calibrated to the Y UKIDSS filter from the work of Mužić et al. (2022). This data, with an effective wavelength of 1.0 µm and a completeness limit of 21.0 mag, had not been utilized previously due to its limited coverage, which focused exclusively on the core of NGC 2244.

We began by selecting sources that were older than 10 Myrs, lacked a fit or had an unreliable one.

Next, we employed a colour-colour diagram, akin to those shown in Figure 4.22, to identify and select sources with masses below 0.15 $M_{\odot}$ based on the BHAC15 model at an age of 2 Myrs and the extinction law of Wang and Chen (2019). Then, we used VOSA to derive the parameters needed to construct the HR diagram presented in Figure 4.23. Figure 4.24 displays a color-magnitude diagram, highlighting the status of sources with SED fits based on their position in the HR diagram.

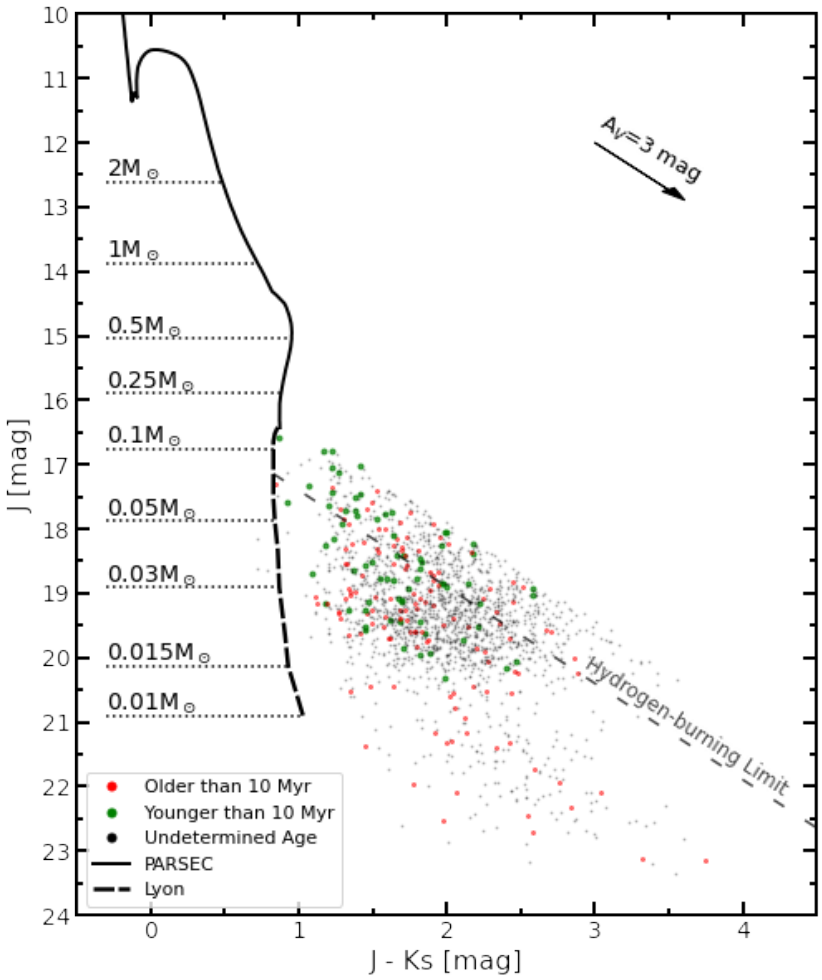

Figure 4.24: The colour-magnitude diagram illustrates the findings from the HR diagram for low mass objects. YSOs under 10 Myrs old (green dots), older than 10 Myrs (red dots), and sources with indeterminate ages (gray dots) are indicated. The 2 Myrs PARSEC (Bressan et al., 2012b; Prisinzano et al., 2019) model isochrone is shown as a solid black line, and the 2 Myrs BHAC15 (Baraffe et al., 2015) model as a dashed black line. The gray dashed line indicates the hydrogen-burning limit, objects below this are classified as substellar. An A_V=3 mag reddening vector is represented.

This approach enabled us to infer the status of 197 sources, where 128 (65%) sources appear older than 10 Myrs. It is important to note that only about 10% of the 197 sources had Y-band photometry. Despite this, we were able to obtain 69 (35%) sources that appear younger than 10 Myrs, even though they had been excluded in the previous section. Of these 69 sources, 12 were Tier 1 selected YSO candidates, 4 were Tier 2 Class I, and the remaining 53 Tier 2 Class II sources were re-added to our sample of YSO candidates. Of these 53 Tier 2 Class II sources, 31 are considered brown dwarfs, assuming an age of 2 Myr.

4.4 Manual cleaning of YSO candidates

In this section, we detailed the process for refining the sample of YSO candidates. We began by eliminating YSO candidates that may be affected by contamination. Specifically, we removed sources located near bright stars, which are prone to diffraction spikes that could distort their photometry readings. Additionally, we excluded sources that have been identified in other studies as being emission knots, despite our initial classification as potential YSOs.

4.4.1 Diffraction spikes contamination

We made efforts to remove YSO candidates whose photometric values might be skewed due to their proximity to bright stars. These bright stars cast diffraction spikes that may affect the photometric values of sources that lay on them. To identify such instances, we utilized photometric data from IRAC1 and an algorithm that identified YSO candidates located within 8 arcseconds of a star brighter than 14 magnitudes and at least three magnitudes more luminous. This analysis yielded 175 potential contaminants. However, upon visually inspecting these potentially contaminated YSOs, we found that most were located in densely populated regions and showed no signs of contamination. This was because the spikes were either not present, not bright enough, or not aligned with the YSO candidate. In some cases, it was unclear if there was significant contamination. Consequently, we conducted manual inspections of all these objects. To minimize subjectivity, we only removed sources that were very likely to have their photometry affected by diffraction spikes.

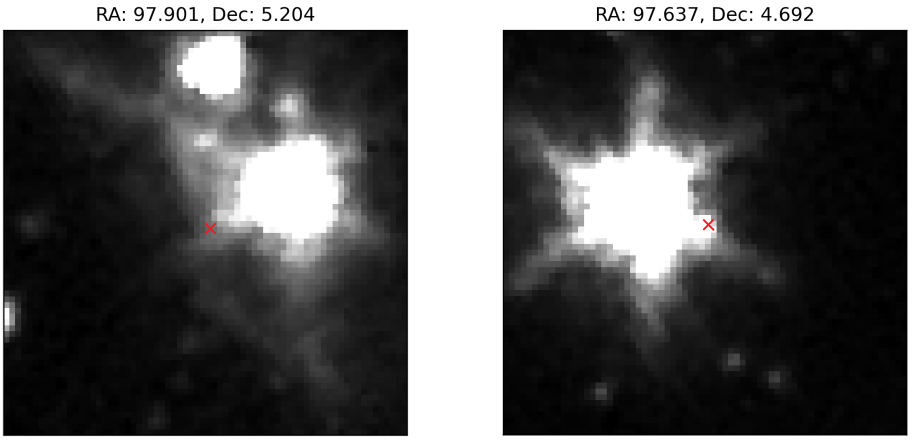

Figure 4.25: The IRAC1 images displays the position of the YSO, marked by a small red cross. It clearly shows the presence of diffraction spikes contaminating the YSO candidate.

Some of the YSO candidates considered contaminated are illustrated in Figure 4.25. Additionally, certain exceptionally bright stars, like the one shown in Figure 4.26, generate diffraction spikes that extend well beyond the 8 arcseconds threshold used on our algorithm. For these stars, a visual inspection across the surrounding region was conducted.

Ultimately, 10 sources were deemed contaminated. These sources are depicted in Figure 4.25 and Figure A.1, in Appendix A, and were removed from our catalogue of YSO candidates.

4.4.2 Emission knots

We cross-matched our YSO candidates catalogue with relevat datasets in Vizier Ochsenbein (1996); Ochsenbein et al. (2000) and also reviewed the literature to identify any known outflows in the region.

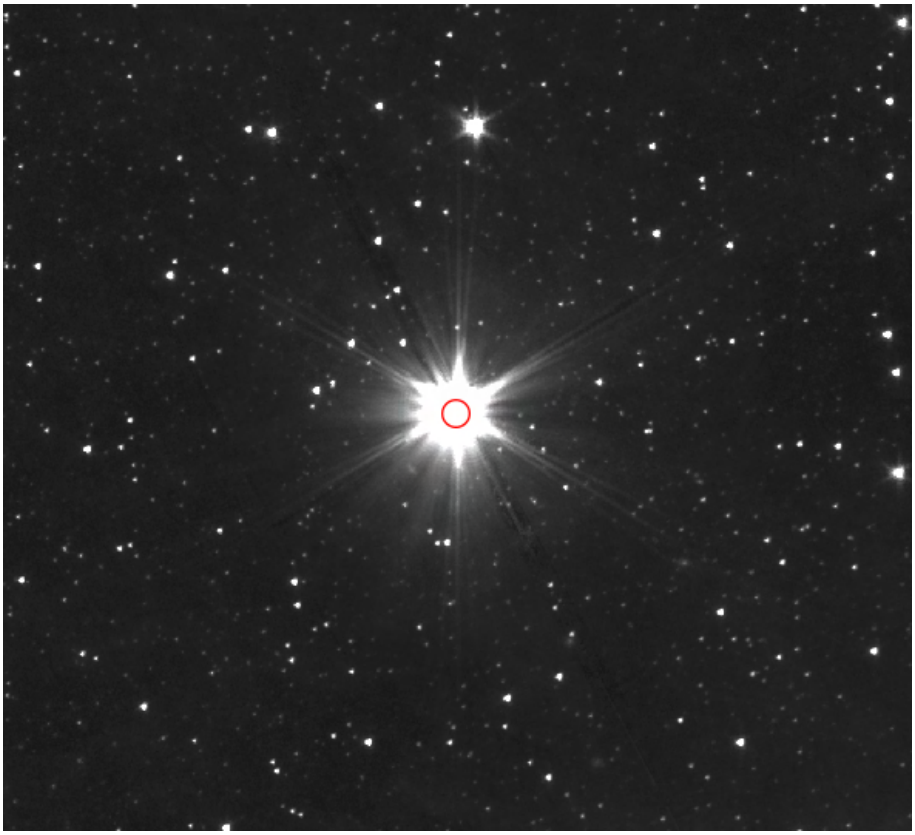

Figure 4.26: The IRAC1 image displays an exceptionally bright star accompanied by its diffraction spikes. This example highlights how such luminous stars, with their prominent diffraction spikes, can potentially interfere with the photometry of sources located along these spikes. A red circumference indicating a radius of 8 arcseconds is shown.

This approach was taken to exclude objects that had previously been classified as different types of celestial bodies. We identified 14 sources, shown in Figure 4.27, that were catalogued as YSO candidates by us. However, they are emission knots from a bipolar protostellar outflow known as MHO 1321, previously identified in the NEWFIRM images (Figure 2.6). These were removed from our YSO candidates catalogue.

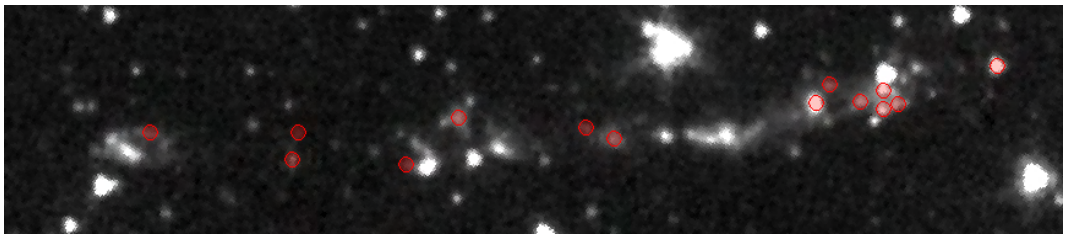

Figure 4.27: Image depicting the bipolar protostellar outflow MHO 1321 (Ybarra et al., 2010) alongside the 15 misclassified YSO candidates, indicated by red circles.

Furthermore, we conducted a visual inspection to identify any additional outflows or emission knots, but none were found.

4.5 Summary

In this chapter, we used the Tier 1 and Tier 2 selection methods to identify and classify YSO candidates, along with a reevaluation process for lower mass objects. Additionally, we removed sources that were likely contaminated or known emission knots.

The Tier 1 selection yielded 1,925 YSO candidates, while the Tier 2 selection yielded 1,311 candidates, of which 622 were not present in the Tier 1 candidates. By reanalyzing some lower mass candidates, we recovered 53 new Tier 2 sources.

This process resulted in a total of 2,600 YSO candidates. Of these, 10 were considered highly likely to be contaminated, and another 14 were known emission knots. This left us with a final catalog of 2,576 YSO candidates. Table 4.3 summarizes the distribution of these candidates by class and tier.

Table 4.3: Final YSO candidates catalogue breakdown.

	Tier 1	Tier 2	New Tier 2
Class I	313	456	291
Class II	1592	1067	380
Total	1905	1523	671

We want to clarify that Tier 1 sources are those selected using the Tier 1 method, while Tier 2 sources are selected using the Tier 2 method. However, some sources may have passed both Tier 1 and Tier 2 selections. Sources that are exclusive to Tier 2 and not identified in Tier 1 are referred to as New Tier 2.

In Table 4.4, you can find six examples of the identified YSO candidates.

Table 4.4: Six examples of identified YSO candidates.

RA [deg]	Dec [deg]	YSO Type	IRAC1 [mag]	IRAC2 [mag]	IRAC3 [mag]	IRAC4 [mag]
97.25687	4.67499	Tier 1 - Class II	13.6	13.4	13.0	12.3
97.39604	4.95788	Tier 1 - Class I	12.2	11.4	10.6	9.3
97.32741	5.19474	Tier 1 - Class II	12.4	12.1	11.9	11.2
98.39107	4.03206	Tier 2 - Class I	8.4	7.2	7.8	-
98.42147	4.61809	Tier 2 - Class II	11.2	10.8	-	10.0
98.56639	4.42112	Tier 1 - Class II	13.8	13.5	12.8	12.0
...						

Chapter 5

Results

In this chapter, we analyze the catalogue of YSO candidates derived in the previous chapter, and summarized in Section 4.5. We begin with an examination of the spatial distribution of the YSO candidates and compare our catalogue of YSO candidates with prevoius works. Then, we discussing the chronology of star formation. Finally, we take a look at the substellar populations present in the catalogue.

5.1 Spatial distribution

The distributions of Tier 1 and Tier 2 YSO candidates are shown in Figures 5.1 and 5.2, respectively. Additionally, Figure 5.3 presents the distribution of both Tier 1 and Tier 2 sources across the entire Rosette Nebula. It should be noted that in cases where Tier 1 and Tier 2 classified a source as different YSO classes, the Tier 1 classification was retained.

We identified YSO candidates in all the young clusters and groups highlighted in the studies by Phelps and Lada (1997); Roman-Zuniga (2006); Poulton et al. (2008); Cambrésy et al. (2013). We also have YSO candidates outside the expected, gas-rich regions. In the northeast, there are many Tier 2, mainly Class I candidates scattered randomly, far from gas clouds where other clusters and groups reside (Dent et al., 2009). These candidates don not seem to be genuine YSOs and are likely extragalactic contaminants. Additionally, some are very near the edge of the mosaic image, leading to poor photometric data and misidentification as IR-excess sources. A similar observation is made in the southwest, dark patch of the mosaic. We see many Tier 1 YSO candidates in this region, despite expecting almost none. This also raises questions about possible extragalactic contamination.

In Figure 5.4, we see a zoomed-in view of the central star cluster NGC 2244, along with the spatial distribution of our YSO candidates. This figure also includes YSO candidates identified in previous studies by Cambrésy et al. (2013) and Broos et al. (2013). Notably, the Class I YSOs tend to be more clustered towards the north. This clustering is due to Tier 2 Class I YSO candidates. This tendency is likely because there is less gas and dust in that region. Since Tier 2 uses shorter wavelengths for selection, it is easier to observe more objects. Additionally, the lower gas density in this area may allow other contaminant sources, typically hidden behind gas clouds, to be observed and misclassified as Class I YSO candidates.

In the lower left side of Figure 5.4, there are regions of strong interaction between the expanding HII-region and the molecular cloud. This interface seems to have generated areas of compressed gas where star formation occurs. This triggered star formation scenario seems to have led to the formation of PL 02 (Poulton et al., 2008; Cambrésy et al., 2013), as seen in Figure 5.5.

Figure 5.6 depicts cold molecular clouds adjacent to PL 02. These dense clouds endure in the intense

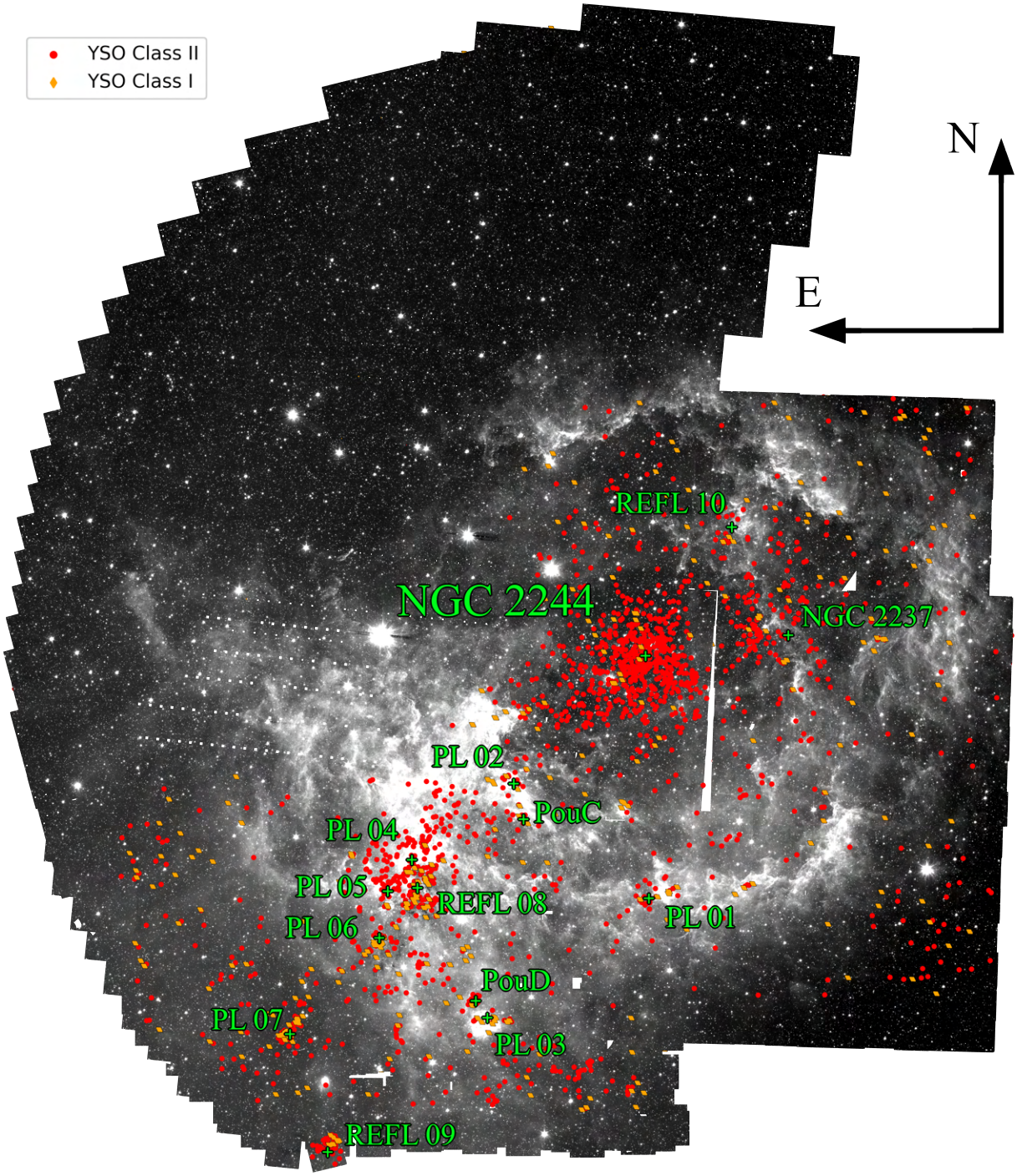

Figure 5.1: Rosette Nebula image overlyed with the locations of Tier 1 YSO candidates, with Class I YSOs marked in orange diamonds and Class II YSOs in red circles. Green crosses denote the positions of young clusters and groups previously identified in the studies by Phelps and Lada (1997); Roman-Zuniga (2006); Poulton et al. (2008); Cambrésy et al. (2013).

UV field of the interface region. The heating and subsequent pressure increase in the lower-density interclump gas compress the primordial, denser clumps. This results in the formation of pillars that orient towards the radiation source (Gritschneder et al., 2010). The high-density tips of these pillars host YSOs (Figure 5.6), potentially resulting from star formation triggered by the NGC 2244 OB population.

Figure 5.7 shows a close-up of the PL 04, PL 05, and REFL 08 regions. These area, along with NGC

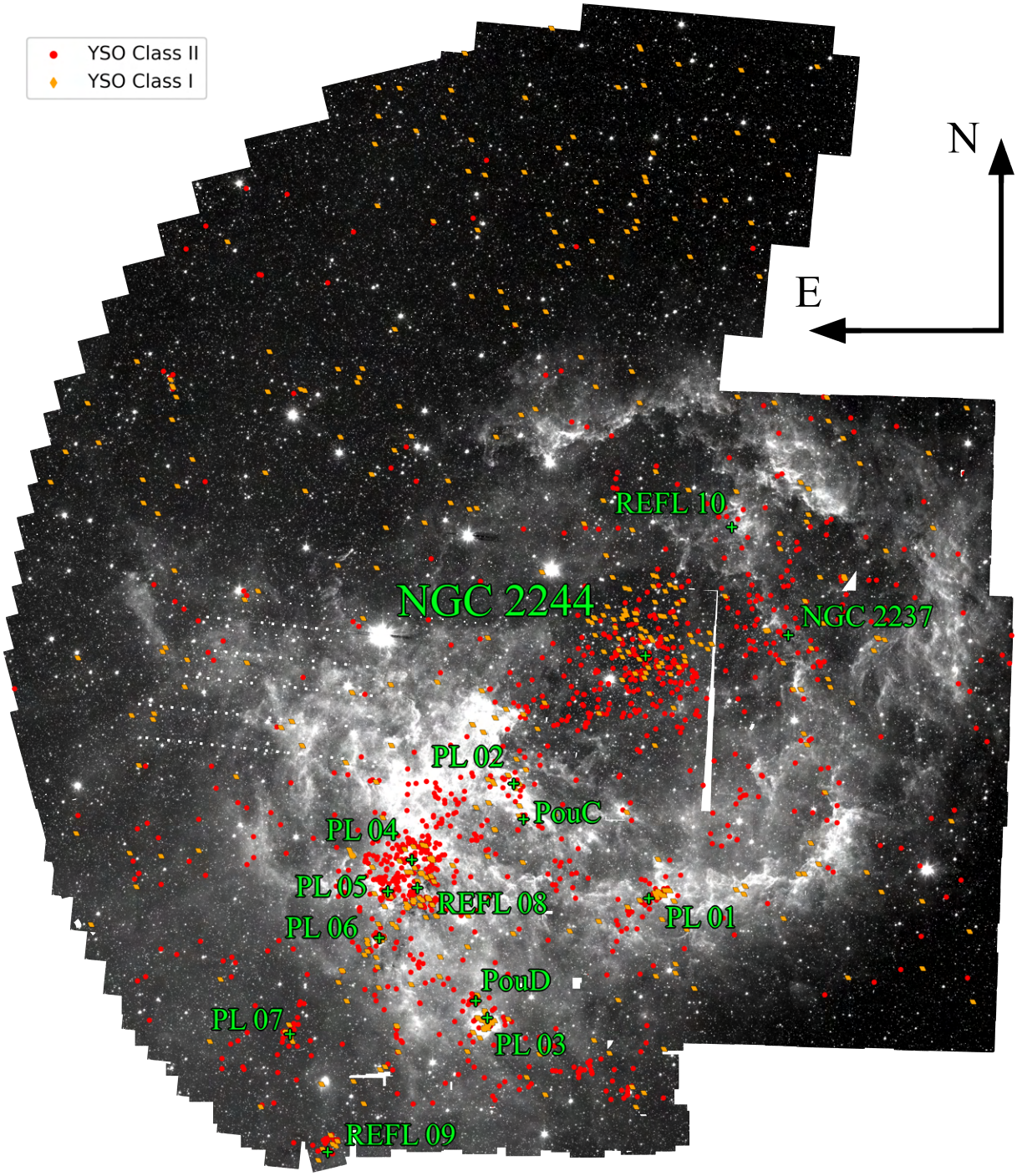

Figure 5.2: Rosette Nebula image overlyed with the locations of Tier 2 YSO candidates, with Class I YSOs marked in orange diamonds and Class II YSOs in red circles. Green crosses denote the positions of young clusters and groups previously identified in the studies by Phelps and Lada (1997); Roman-Zuniga (2006); Poulton et al. (2008); Cambrésy et al. (2013).

2244, contain the majority of YSO candidates. Despite being categorized as three distinct groups, they appear to be part of the same complex. This region has many notable structures, with the most important related to the YSO Class I and Class II distribution. Most Class I YSO candidates are found in dark, cold, dense molecular clouds where star formation is likely ongoing, as evidenced by the presence of a high proportion of Class I sources relative to Class II sources.

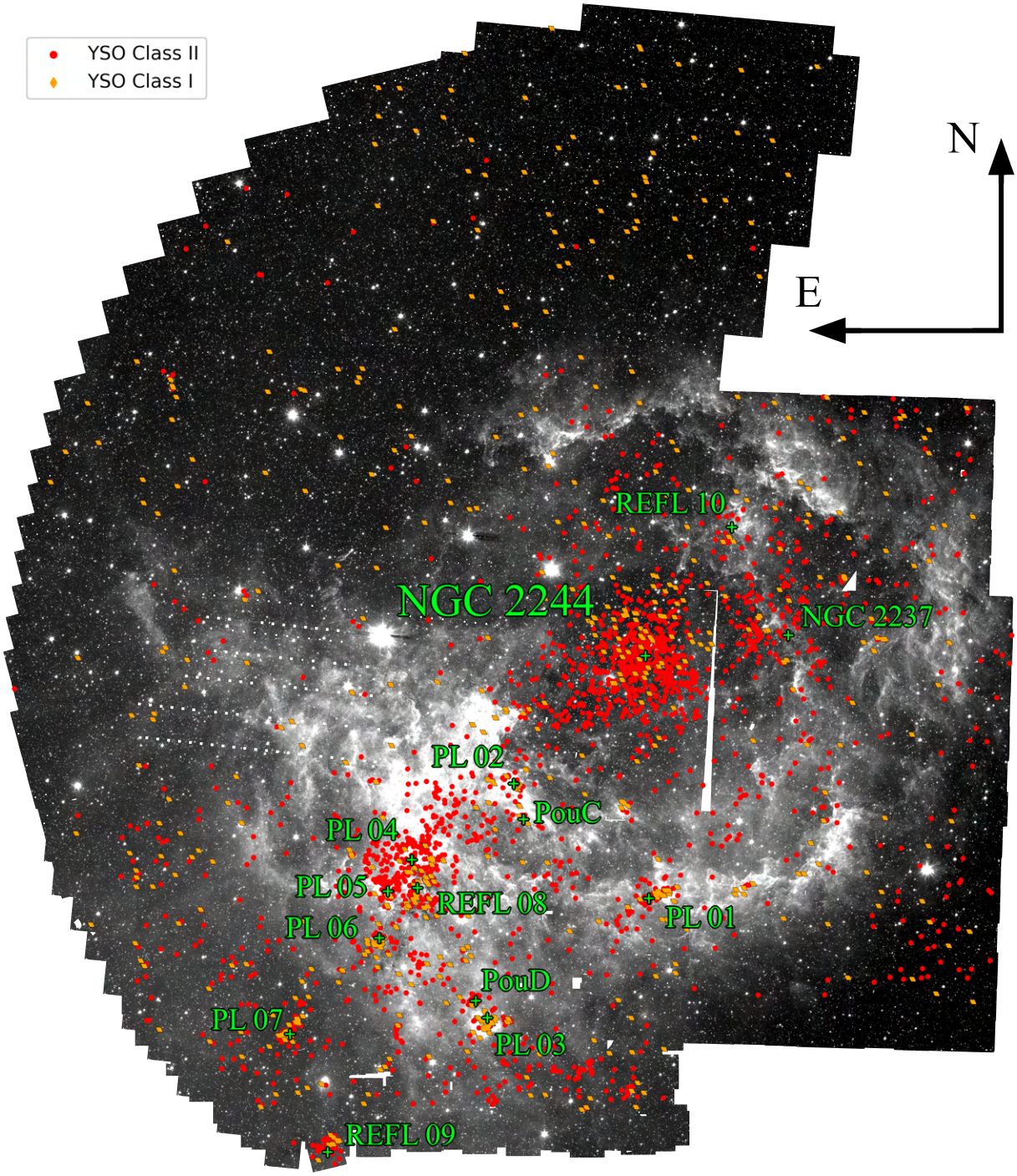

Figure 5.3: Rosette Nebula image overlyed with the locations of Tier 1 and Tier 2 YSO candidates, with Class I YSOs marked in orange diamonds and Class II YSOs in red circles. Green crosses denote the positions of young clusters and groups previously identified in the studies by Phelps and Lada (1997); Roman-Zuniga (2006); Poulton et al. (2008); Cambrésy et al. (2013).

Similar to the pillars shown in Figure 5.6, the YSO candidates hosted by the pillars on the left side of Figure 5.7 were likely formed due to the intense radiation from OB stars, which compressed the gas and triggered the star formation process. These pillars are shown in greater detail in Figure 5.8.

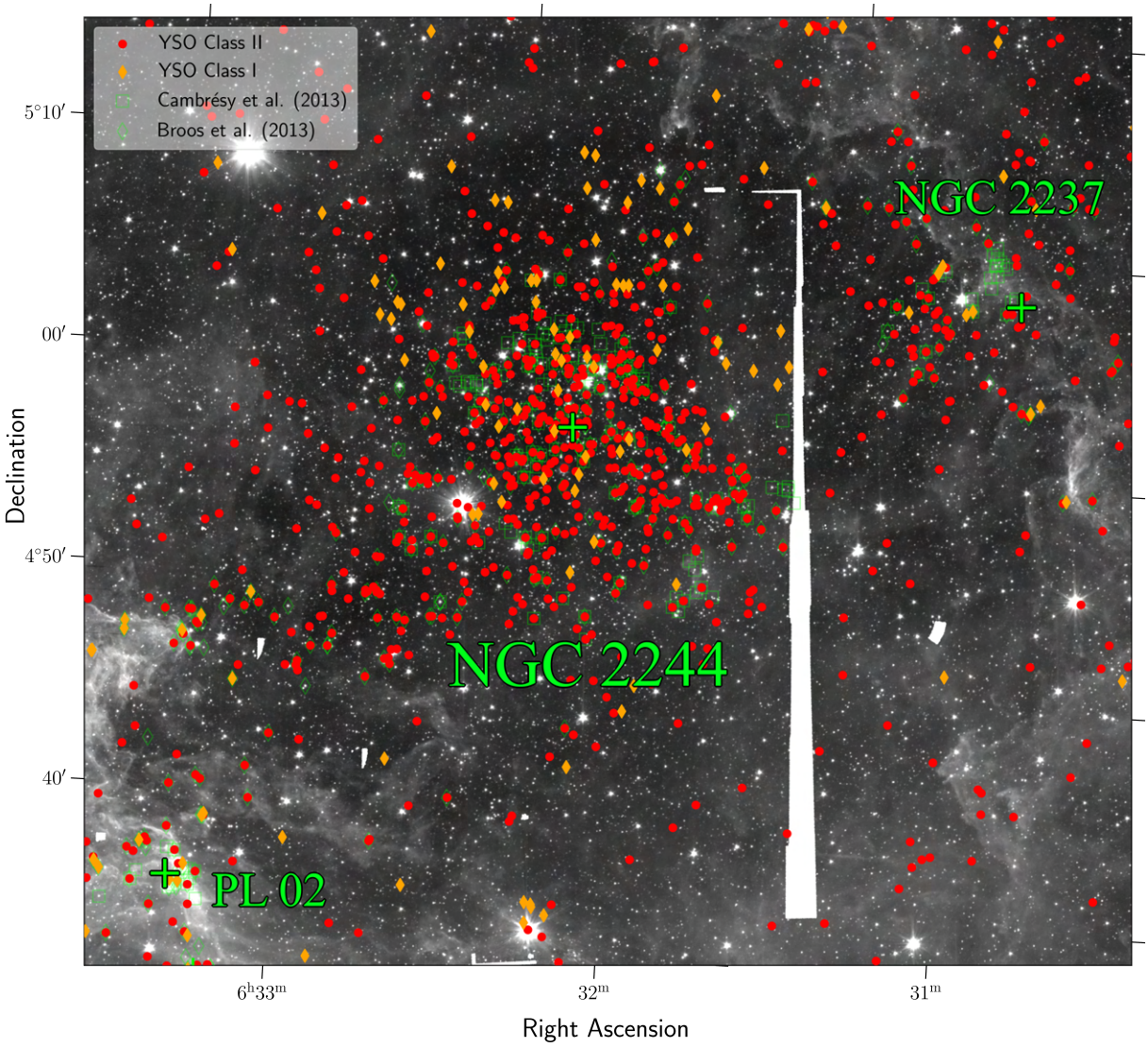

Figure 5.4: YSO candidates spatial distribution in the NGC 2244 region. Class I YSO candidates are marked with orange diamonds and Class II YSO candidates with red circles. Previously identified YSO candidates by Cambrésy et al. (2013); Broos et al. (2013) are highlighted with green squares and diamonds, respectively.

5.2 Comparison to previous works

In this section, we will compare our catalogue of YSO candidates with those from previous studies, particularly the works of Broos et al. (2013) and Cambrésy et al. (2013). Our focus will be on the number of YSO candidates that overlap with our catalogue. Additionally, we will examine the methods used in these earlier studies to identify YSOs and discuss how these approaches influence the degree of overlap between their catalogues and ours. Figures 5.4, 5.7, and 5.8 illustrate the distribution of YSO candidates within relevant clusters and groups. These figures also highlight the positions of YSO candidates identified by Broos et al. (2013) and Cambrésy et al. (2013), marked in green.

The work of Broos et al. (2013) is associated with the MYStIX (Massive Young Star-forming Complex Study in Infrared and X-rays) project, which aimed to identify and study young stars in star-forming regions. Their samples of YSO candidates are primarily derived from X-ray data, but they also incorporate NIR data from 2MASS and UKIRT, as well as MIR data from the Spitzer Space Telescope, similar to

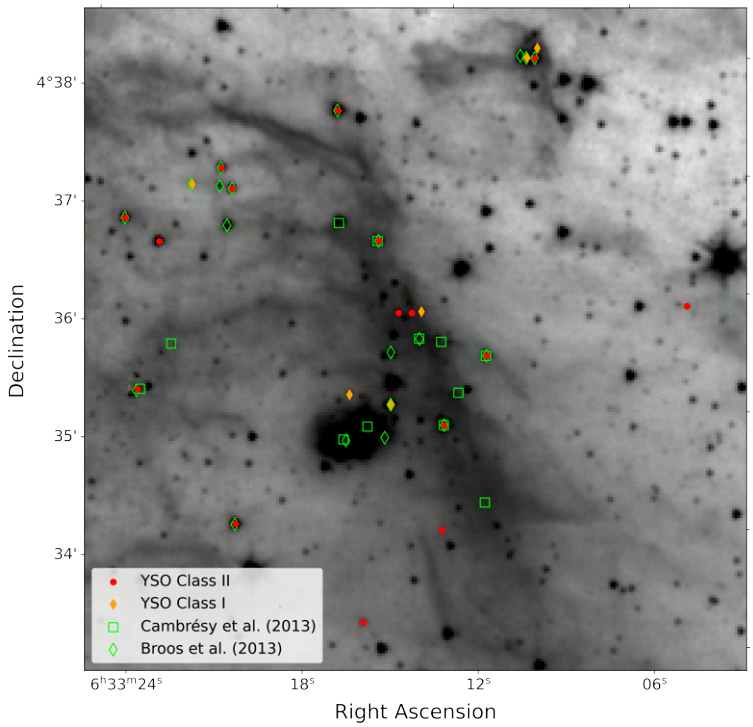

Figure 5.5: YSO candidates spatial distribution on the PL 02 interface region between the expanding HII-region and the molecular cloud. Class I YSO candidates are marked with orange diamonds and Class II YSO candidates with red circles. Previously identified YSO candidates by Cambrésy et al. (2013); Broos et al. (2013) are highlighted with green squares and diamonds, respectively.

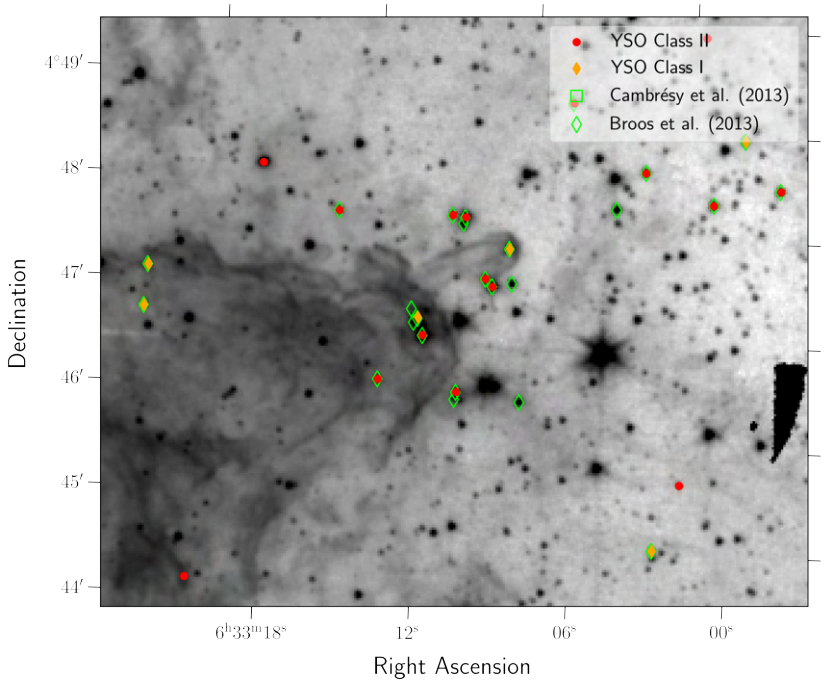

Figure 5.6: Cold molecular pillars adjacent to the PL 02 interface region. Class I YSO candidates are marked with orange diamonds and Class II YSO candidates with red circles. Previously identified YSO candidates by Cambrésy et al. (2013); Broos et al. (2013) are highlighted with green squares and diamonds, respectively.

our dataset. For comparison with the work of Broos et al. (2013), we will exclude sources categorized as YSO candidates based on X-ray data and focus solely on those identified through their IR-excess. Unlike

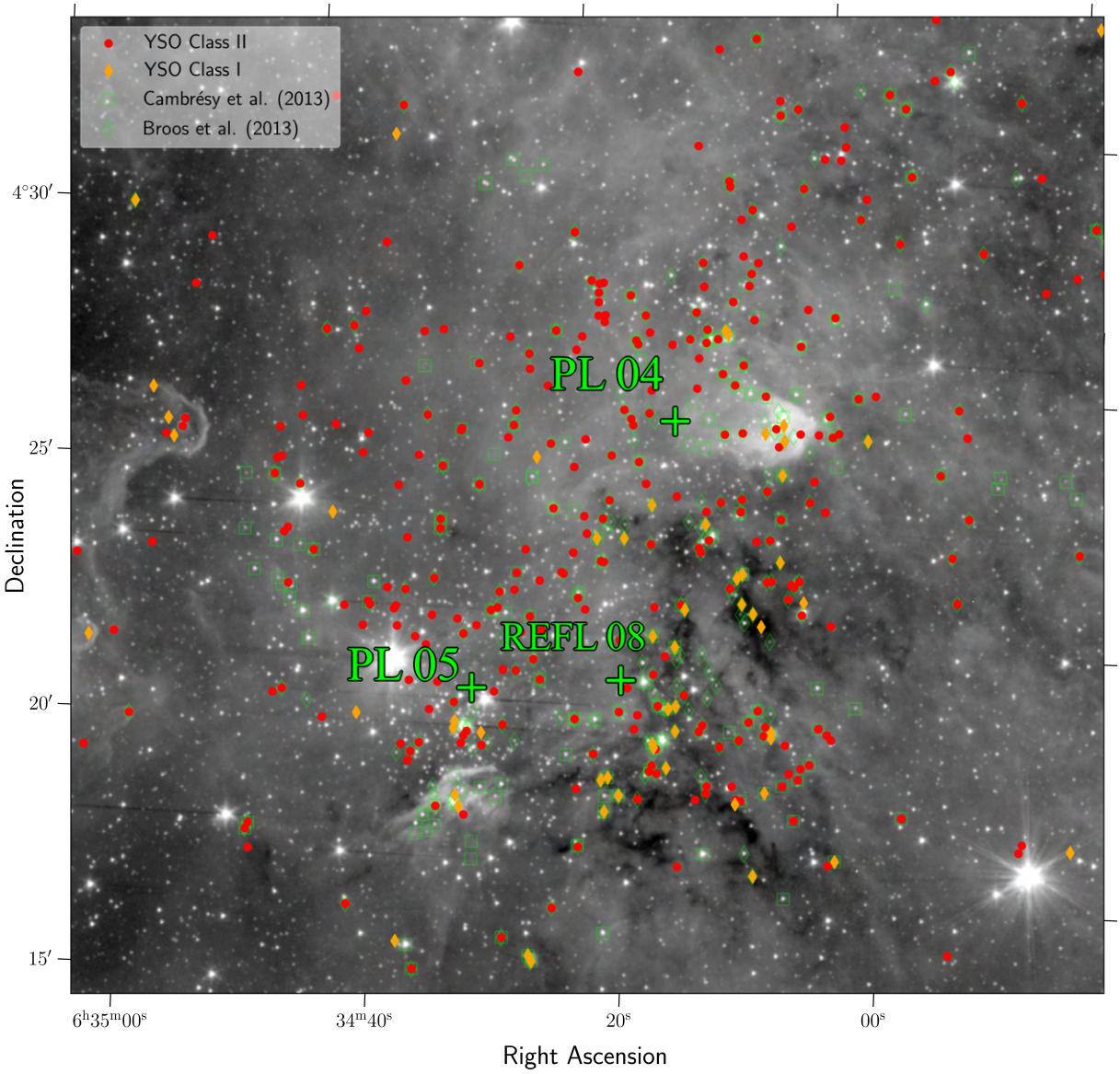

Figure 5.7: Close-up view of YSO candidates spatial distribution in the PL 04, PL 05, and REFL 08 region. Class I YSO candidates are marked with orange diamonds and Class II YSO candidates with red circles. Previously identified YSO candidates by Cambrésy et al. (2013); Broos et al. (2013) are highlighted with green squares and diamonds, respectively.

our catalogue of YSO candidates, which is primarily selected using colour-colour diagrams, the MYStIX project selects YSOs by identifying sources with IR-excess through SED fitting. This is followed by a series of colour cuts to eliminate contaminants (Povich et al., 2013). They identified a sample of 592 YSO candidates exhibiting IR-excess, with 586 of them including photometry in both the IRAC1 and IRAC2 bands. Of these, we recovered 457 candidates, achieving a 78% recovery rate. Our approach to selecting YSO candidates differs, but the primary reason for the overlap not being greater is likely due to their use of different SED models, which led to more candidates being flagged as having IR excess. The region studied by the MYStIX project overlaps with many clusters and groups that lack coverage in certain areas in IRAC4, as seen in Figure 5.10. For instance, a genuine Class II YSO located in the PL 02 interface region might miss IRAC4 coverage, causing it to fail the Tier 1 requirements. If only J, H, K_S, IRAC1, IRAC2, and IRAC3 data are available, it might not meet the criteria to be considered a Tier 2 YSO can-

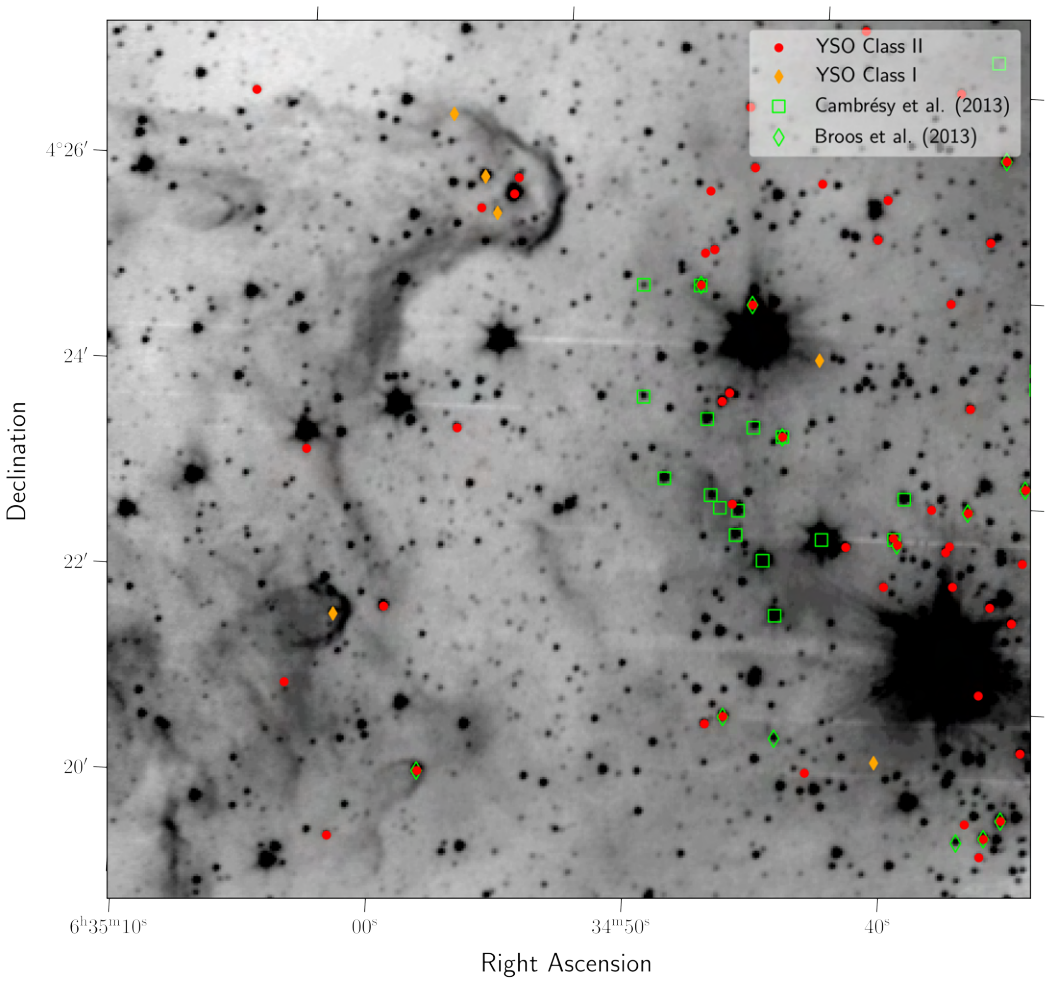

Figure 5.8: A zoomed-in view of the spatial distribution of the YSO candidates in the cold molecular pillars near the PL 04, PL 05, and REFL 08 complex. Class I YSO candidates are marked with orange diamonds and Class II YSO candidates with red circles. Previously identified YSO candidates by Cambrésy et al. (2013); Broos et al. (2013) are highlighted with green squares and diamonds, respectively.

didate, as there may be insufficient points without IR excess to construct a complete SED, leading to a failure of the Tier 2 requirements. In contrast, the MYStIX project might consider this data sufficient, as their method involves constructing SEDs to identify IR excess sources, followed by SED fitting with YSO models for some of the sources. Additionally, instead of excluding objects impacted by structured PAH aperture contamination, the MYStIX project reanalyzes them, discarding IRAC2 photometry but proceeding with SED fitting using YSO models, which may help them recover a few more YSOs.

Other research, such as that conducted by Cambrésy et al. (2013), also incorporates NIR data from 2MASS and UKIDSS. However, instead of utilizing MIR photometric data from the Spitzer Space Telescope, they used MIR photometric data from WISE (Wide-field Infrared Survey Explorer; Cutri et al. 2021). Their sample of YSO candidates was obtained by analyzing the density of sources in the NIR, which allowed them to map the spatial distribution of the molecular cloud and detect embedded clusters. Then sources within the projected cluster boundaries were classified based on their colour, following the methodology described by Koenig et al. (2012). Additionally, they employed a second classification method based on quadratic discriminant analysis, as outlined in the work of Marton et al. (2013). The work of Cambrésy et al. (2013) reports a sample of 508 YSO candidates, excluding sources from the CMFT10 and CMFT11 groups that were outside the FoV analyzed in our study. Of the 508 YSO

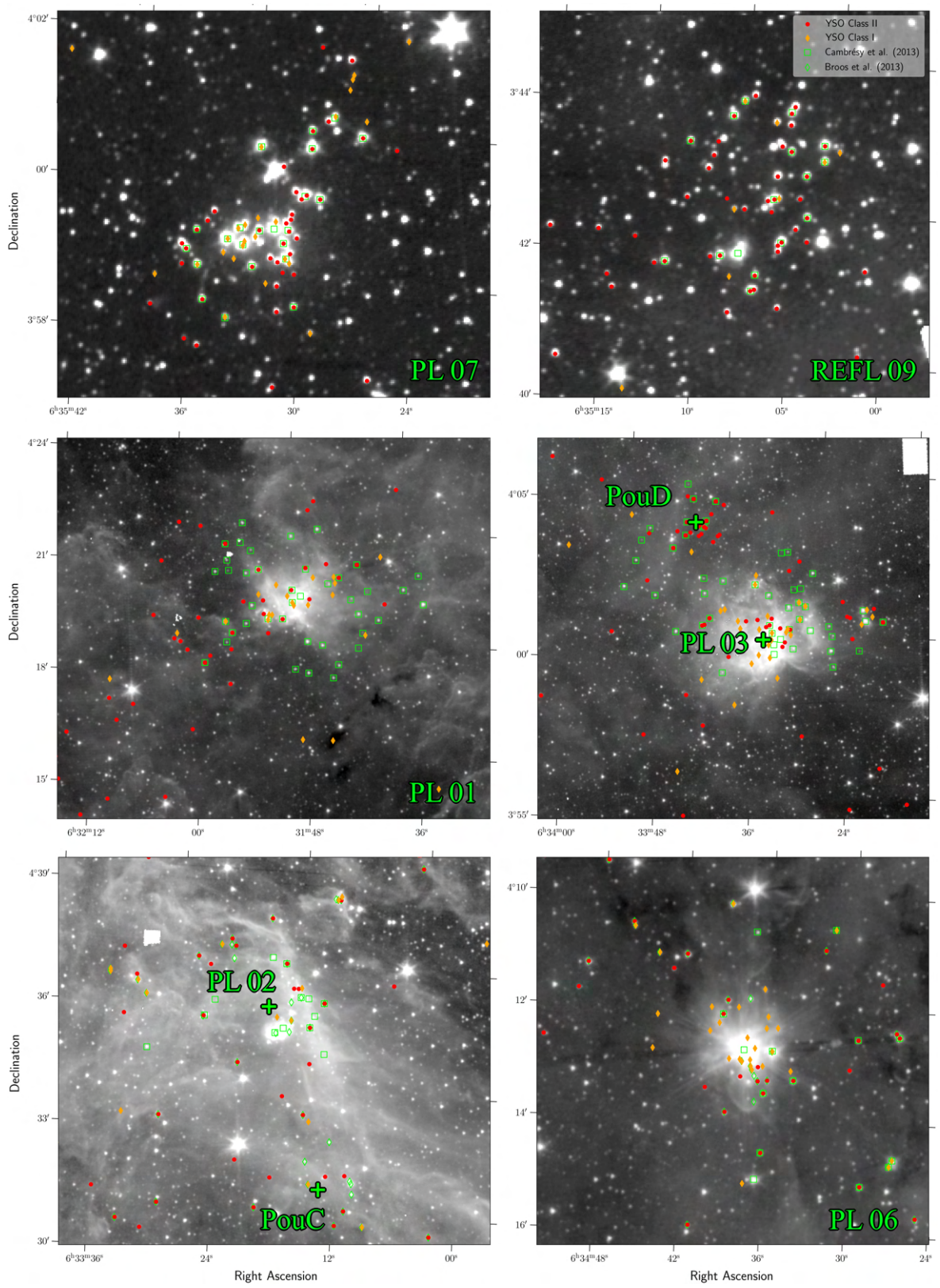

Figure 5.9: Distribution of YSO candidates in other groups and clusters. Class I YSO candidates are marked with orange diamonds and Class II YSO candidates with red circles. Previously identified YSO candidates by Cambrésy et al. (2013); Broos et al. (2013) are highlighted with green squares and diamonds, respectively.

candidates, we recovered 241, resulting in a recovery rate of 47%. This lower recovery rate is attributed to their use of MIR photometry from WISE. WISE has filters with wavelengths of 3.4, 4.6, 12, and 22

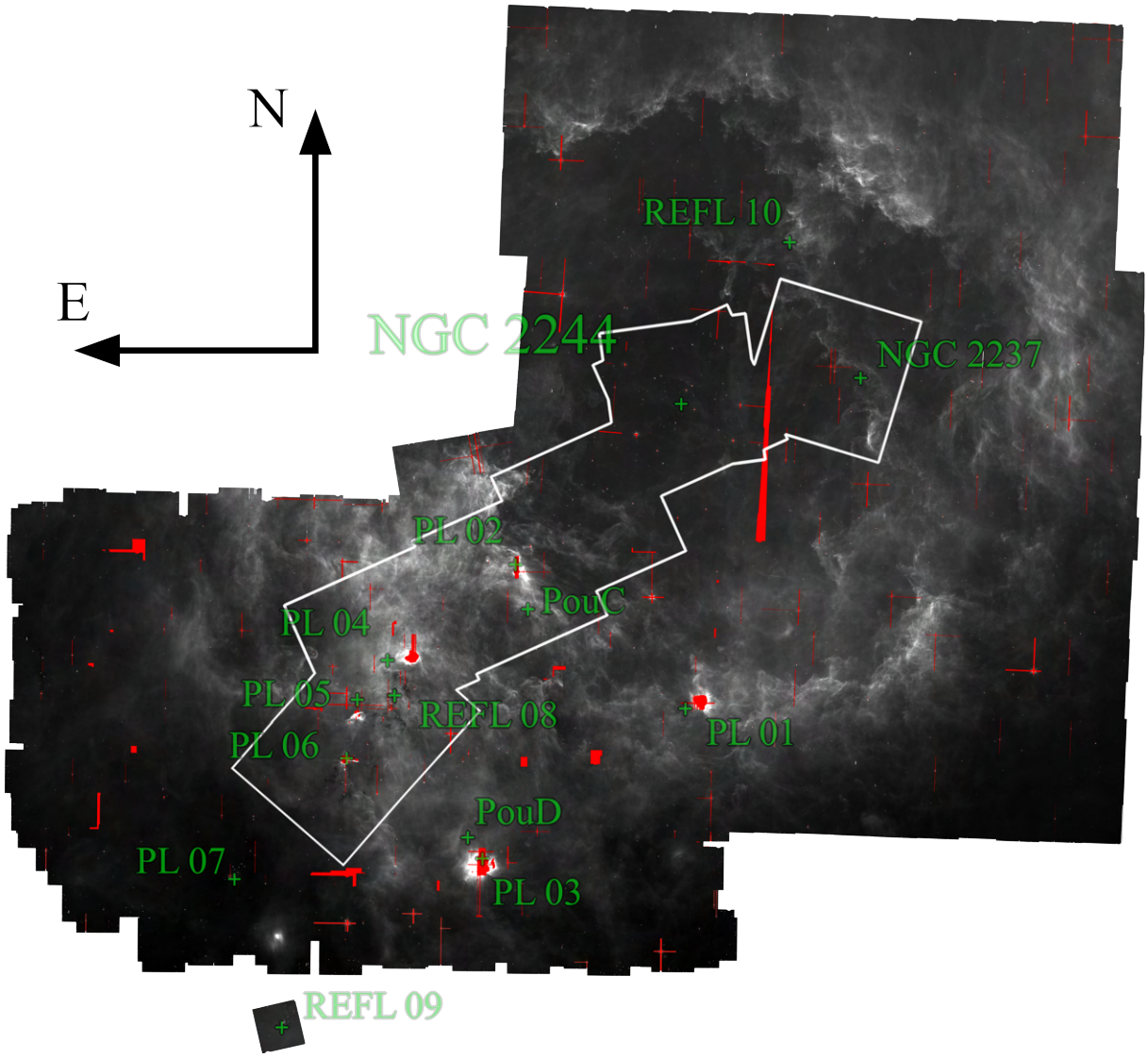

Figure 5.10: This figure shows the IRAC4 mosaic image, with regions lacking data highlighted in red. The names and locations of previously known groups and clusters are marked in green, while the areas analyzed in the MYStIX project are represented by the white outline.

µm, with the last two extending beyond the range of IRAC4. These longer wavelengths enable WISE to explore YSO populations with IR excess at these wavelengths, including Class 0 YSOs, which cannot be detected in any of the IRAC bands. Furthermore, WISE's spatial resolution is insufficient for some densely populated regions within the Rosette Nebula. IRAC bands, with a spatial resolution between 1 and 2″[1], provide higher resolution compared to WISE bands, which range from 6 to 12″[2]. This difference can cause the blending of emissions from multiple celestial sources that are distinguishable in IRAC data. Moreover, some YSO candidates identified by Cambrésy et al. (2013) appear blended with nebular emissions or are simply nebular emission resolved by IRAC. Examples of these instances can be observed in Figures 5.7 and 5.9.

[1]https://lweb.cfa.harvard.edu/ mmarengo/me/irac.html
[2]https://wise2.ipac.caltech.edu/docs/release/allsky/

5.3 Star formation chronology

The core of the Rosette Nebula houses the young star cluster NGC 2244, which contains a large OB association. These massive stars form an expanding HII region that interacts with nearby molecular clouds. This interaction may trigger star formation, leading to populations of YSOs (Dale et al., 2007). Evidence of this process has been observed in the PL 01 and PL 02 regions (Phelps and Lada, 1997; Poulton et al., 2008; Cambrésy et al., 2013). Poulton et al. (2008) noted that PouC, PL 01, and PL 02 are located at the interface, coinciding with clumps visible in ^{13}CO. According to Poulton et al. (2008), cluster formation in these regions is consistent with molecular cloud compression by the expanding HII region. Cambrésy et al. (2013) also noted that the youth of PL 01 and PL 02 supports the idea that compression effects could have triggered cluster formation in this interface. Schneider et al. (2010) reached the same conclusion based on the large number of dense cores found in this region.

However, in regions that are located further out from NGC 2244 such as PL 04, PL 05, REFL 08, PL 07, PouD, PL 03, and REFL 09, the star formation observed cannot be solely attributed to triggering by the ionization front. Previous research suggests that the cloud's dynamical evolution plays a more significant role in these areas, with minimal, if any, contribution from triggering effects (Heyer et al., 2006; Román-Zúñiga and Lada, 2008; Poulton et al., 2008; Schneider et al., 2010; Cambrésy et al., 2013). This suggests that the formation of NGC 2244 triggered or accelerated star formation in the PL 01, PL 02, and PouC interface region through gas compression, while star formation in other regions likely took place independently of NGC 2244's influence.

Based on the work of Mužić et al. (2022), the proper motions of matching YSO candidates relative to the mean proper motions of NGC 2244 members were obtained and are represented in Figure 5.11. This data reveals a clear interaction between the population of YSO candidates in PL 01 and the expanding HII bubble. The YSO candidates in the PL 01 region appear to be pushed away from the cavity occupied by NGC 2244. A similar conclusion can be drawn for the cold molecular pillar adjacent to PL 02, where most sources also appear to be moving in the same direction and orientation as the expanding HII front. This supports the triggered formation scenario, suggesting that the proper motions of young sources in these regions are influenced by their interaction with the HII front.

By comparing the proportions of Class I to Class II YSOs in Figures 5.9 and 5.12, we can compare the ages of the depicted regions. Regions with a low proportion of Class I relative to Class II YSOs are older, as Class II YSOs are generally older than Class I YSOs. For example, the east part of region of the PL 04, PL 05, and REFL 08 complex (the top-left section of the right panel in Figure 5.12) shows a very low density of Class I YSOs, similar to the central region of the NGC 2244 cluster. This suggests that both regions are of similar age. Likewise, PouD, NGC 2237, REFL 09, and REFL 10 have few Class I YSO candidates (less than 20%), indicating an older age. In contrast, the PL 01 cluster and the ridge region of PL 02 and PouC contain a moderate proportion of Class I YSOs (20 to 40%). The regions PL 03, PL 06, PL 07, and the west part of the PL 04, PL 05, and REFL 08 complex have a high proportion of Class I YSOs (over 40%), indicating they are younger. Moreover, the high density of Class I YSOs also indicates that these regions are likely still experiencing ongoing star formation. Cambrésy et al. (2013) analysis identified NGC 2244 as the oldest cluster, followed by REFL 09, NGC 2237, and the eastern part of the PL 04, PL 05, and REFL 08 complex. Furthermore, the age map produced by Mužić et al. (2022) confirms that the NGC 2244 and NGC 2237 clusters are also among the oldest regions, which is consistent with our findings. Cambrésy et al. (2013) also found the youngest regions to be PL 01, PL 02, PL 03, and the western part of the PL 04, PL 05, and REFL 08 complex. Mužić et al. (2022) concluded that the region southeast of NGC 2244 contains, on average, the youngest stars in the entire

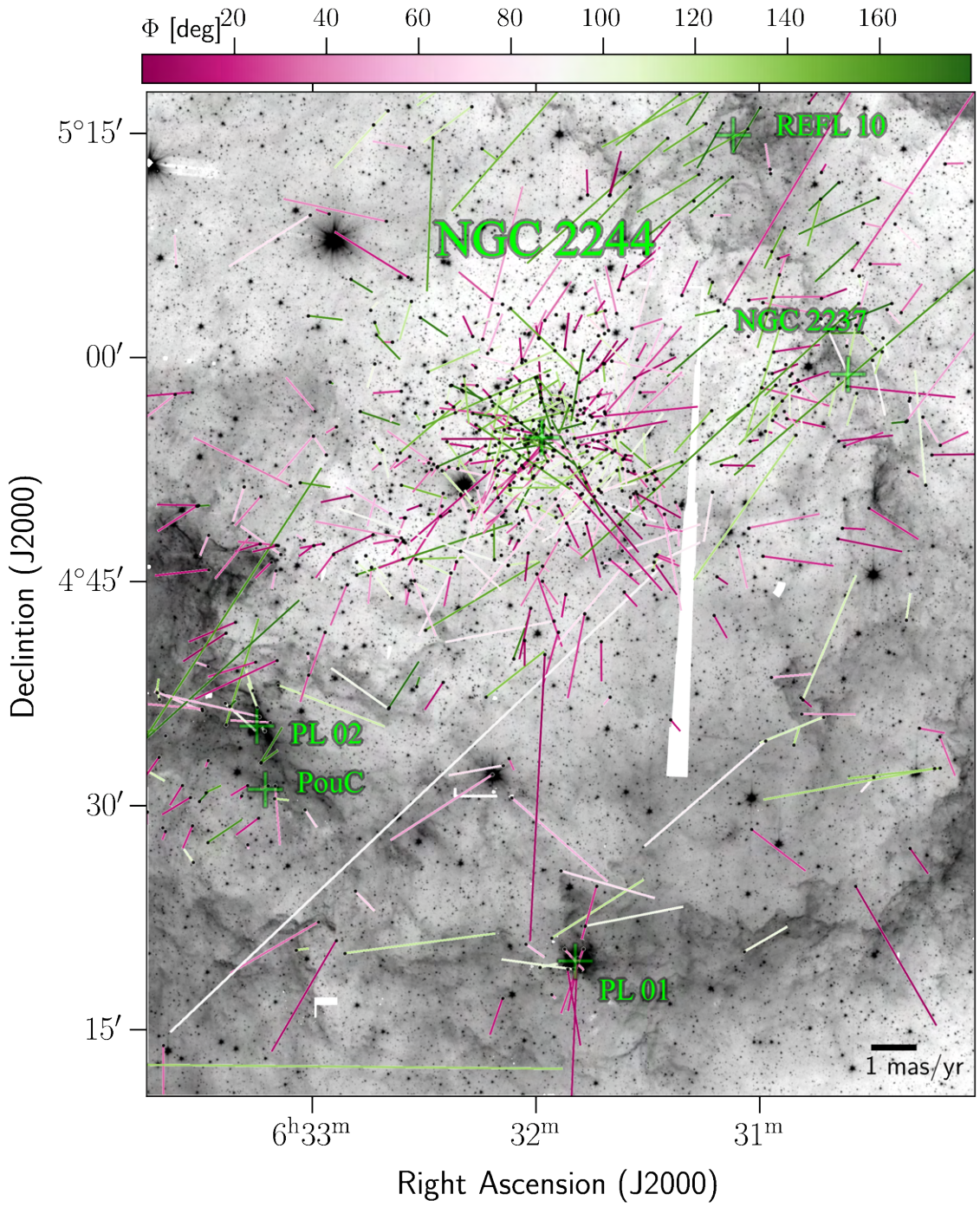

Figure 5.11: The proper motions of the YSO candidates relative to the mean proper motion of sources member of NGC 2244 based on the work by Mužić et al. (2022) are colour-coded according to the angle between each star's motion vector and the line connecting it to the cluster center. Stars moving predominantly away from the cluster center are marked in purple hues, while those moving towards it are in green. Near-white sources indicate motion nearly perpendicular to the line connecting them to the NGC 2244 cluster center, and these stars may be moving in opposite directions relative to each other. The background image used is the IRAC1 mosaic.

Rosette Nebula.The age map produced by Mužić et al. (2022) shows that PL 01 is the youngest known group, followed by the western part of the PL 04, PL 05, and REFL 08 complex, and PL 07. However, contrary to our results and the work of Mužić et al. (2022), Cambrésy et al. (2013) identified PL 07 and PL 06 as some of the oldest populations, suggesting they might have formed around the same time as NGC 2244. Cambrésy et al. (2013) argued that despite the presence of young protostars in these clusters,

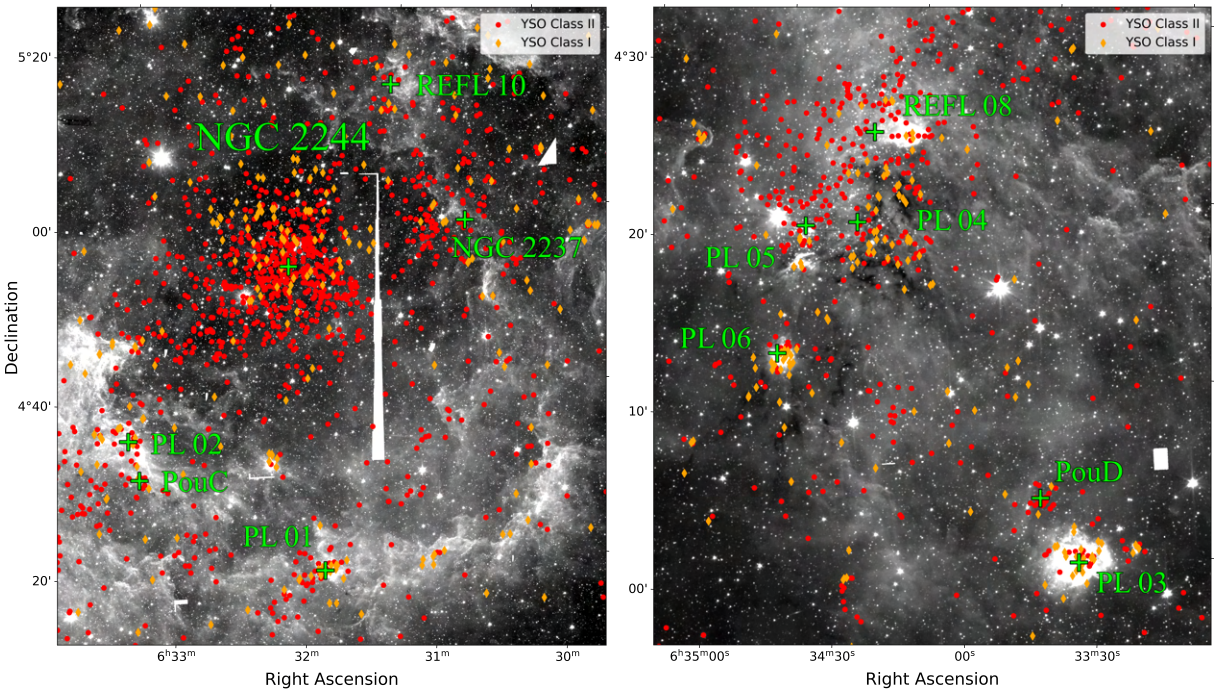

Figure 5.12: The spatial distribution of YSO candidates in the two most populated regions of the Rosette Nebula is shown. The left panel displays NGC 2244 and its surrounding areas, while the right panel shows the PL 04, PL 05, and REFL 08 complex, along with the PouD and PL 03 regions. Class I YSO candidates are marked with orange diamonds and Class II YSO candidates with red circles. Previously identified YSO candidates by Cambrésy et al. (2013); Broos et al. (2013) are highlighted with green squares and diamonds, respectively.

the significant age is that of the collapse, meaning that some YSOs in the cluster are older because they collapsed earlier. Cambrésy et al. (2013) analysis found old YSOs in these regions, indicating an early collapse and thus making these regions older.

The spatial distribution and relative proportions of our Class I and Class II YSO candidates align with the findings of Heyer et al. (2006); Román-Zúñiga and Lada (2008); Poulton et al. (2008); Schneider et al. (2010); Cambrésy et al. (2013), which highlight the significant role of the Rosette Nebula's dynamical evolution in its star formation history. While some clusters might have been triggered by the HII front, the presence of YSO populations well beyond the interface region demonstrates that star formation is occurring in the Rosette Nebula independently of NGC 2244 and its expanding HII region. Furthermore, our rough age estimates for most of the groups and clusters indicate variations that do not correlate with their positions within the Rosette Molecular Cloud or their distance from NGC 2244.

5.4 Substellar YSO candidates

To identify the substellar YSO candidates, we used the colour-magnitude diagram shown in Figure 5.13. Note that not all YSO candidates have photometry in the J- and K_S-bands. Therefore, out of 2,576 YSO candidates, only 2,205 (86%) are included. Although all 2,576 candidates have IRAC1 and IRAC2 bands, these were not used to construct a colour-magnitude diagram because MIR is affected by IR-excess. NIR is less affected, making it better for determining stellar properties.

In the left panel of Figure 5.13, we observe the sources selected using the Tier 1 method. A noticeable feature is that Class I YSO candidates tend to experience more reddening, which is expected as these

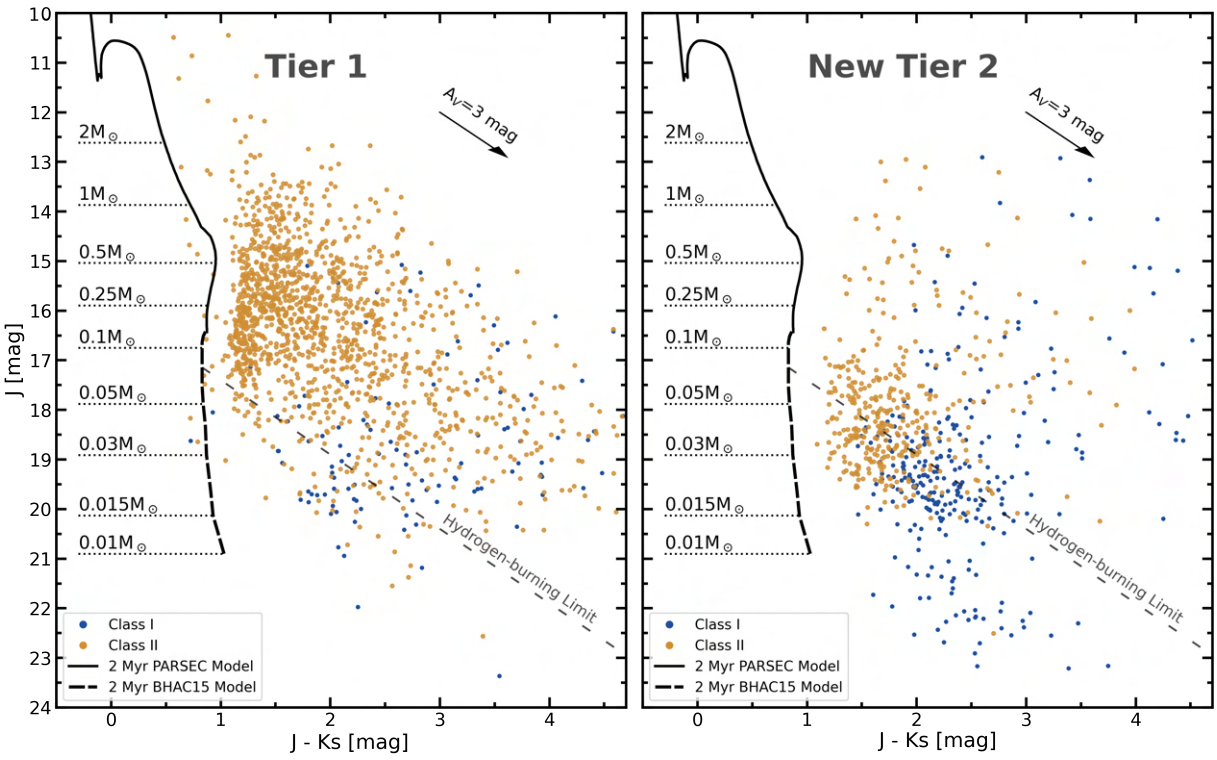

Figure 5.13: The left panel displays the colour-magnitude diagram for YSO candidates selected in Tier 1. The right panel presents the colour-magnitude diagram for new Tier 2 YSO candidates, which are those identified by the Tier 2 method that are not included in Tier 1. YSO candidates that are part of the Class I (blue dots) and Class II (orange dots) populations. The 2 Myrs PARSEC (Bressan et al., 2012b; Prisinzano et al., 2019) model isochrone is shown as a solid black line, and the 2 Myrs BHAC15 (Baraffe et al., 2015) model as a dashed black line. The gray dashed line indicates the hydrogen-burning limit, objects below this are classified as substellar. An A_V=3 mag reddening vector is represented.

objects are still surrounded by a dense envelope of gas and dust. The right panel shows the New Tier 2 sources, which are those selected by the Tier 2 method but not in Tier 1, ensuring no overlap between the two panels in Figure 5.13. In this panel, Class I YSO candidates generally exhibit more reddening. However, many of these sources appear to be less reddened than the Tier 1-selected Class I candidates. This suggests they may be misclassified and are more likely Class II YSOs or even extragalactic contaminants, as discussed in Section 5.1. Another notable remark is that the New Tier 2 sources tend to have lower masses. This is expected, as lower mass objects are fainter and likely went undetected in at least one of the IRAC3 or IRAC4 filters, which were the limiting filters due to their lower completeness magnitude compared to IRAC1 and IRAC2 (refer to Table 3.1). Additionally, the strict cutoff applied in the first colour-colour diagram of the Tier 2 selection method (Figure 4.14) may also be skewing the results.

Assuming an age of 2 Myrs, in our sample of 2,205 YSO candidates, 397 (18%) are below the hydrogen-burning limit of 0.075 $M_{\odot}$, indicating they are substellar objects. By selecting these sources in Figure 5.13 and fitting a linear regression with the same slope as the reddening vector, we determined the average mass of these substellar YSO candidates. The point where the linear regression fit intersects with the isochrone model indicates an average mass of just under 0.05 $M_{\odot}$. By analyzing the position of sources in the color-magnitude diagram (Figure 5.13) and the HRdiagrams (Figures 4.21 and 4.23), we find that the lowest mass object in Tier 1 has a mass of 0.015 $M_{\odot}$. Additionally, in Tier 2, we have 7 objects below the 0.012 $M_{\odot}$ limit. Below this limit, brown dwarfs cannot fuse deuterium in their cores

and are often called planetary-mass objects. The lowest mass object with a SED fit appears to have an age lower than 0.5 Myrs, with mass ranges from 0.010 to 0.015 $M_{\odot}$. This places it between a low-mass brown dwarf and a high-mass planetary mass object.

Researchers have been investigating the formation of brown dwarfs for decades, seeking to understand their origins. Our identification of substellar objects within our catalogue of YSO candidates supports the idea that brown dwarfs form through the same channels as stars. It is now widely accepted that most high-mass brown dwarfs form similarly to stars (Luhman, 2012). Furthermore, earlier studies in NGC 2244 have also reported the presence of disks around brown dwarfs (Balog et al., 2007; Almendros-Abad et al., 2023). Notably, we recovered seven spectroscopically confirmed young brown dwarfs from Almendros-Abad et al. (2023). However, despite growing evidence for the presence of disks, the early evolutionary stages of brown dwarfs, particularly during their embedded Class 0/I phases, remain poorly understood (Morata et al., 2015; Barrado et al., 2018). Our catlogue of YSO candidates provides 33 Tier 1 selected Class I YSO candidates with masses below the hydrogen burning limit. This offers an opportunity for future studies of these objects in the Rosette Nebula region. We should also note that our coverage in the lower mass regime is not complete, and we expect many more brown dwarfs in both Class I and Class II stages yet to be discovered.

Chapter 6

Summary and Conclusions

The Rosette Nebula is an emblematic star-forming region, located approximately 1.5 kpc from Earth (Mužić et al., 2019), and is home to a rich population of young stars. At its heart lies the young star cluster NGC 2244, which comprises a large OB association. These massive stars emit intense ultraviolet radiation that ionizes the surrounding gas, creating a bright, expanding HII region. These strong stellar winds drive an ionization front that is evacuating the central region of the nebula by dispersing its original molecular cloud. NGC 2244, estimated to be around 2 Myrs old (Mužić et al., 2022), is not the only stellar population in the Rosette Nebula. Additional stellar groups have been identified in previous studies (Phelps and Lada, 1997; Roman-Zuniga, 2006; Poulton et al., 2008; Cambrésy et al., 2013), contributing to the complex structure of this dynamic star-forming region.

We investigated the young stellar and, for the first time, the substellar (brown dwarf) populations over a wide region of the Rosette Nebula, well beyond the central cluster NGC 2244. Our study aimed to reveal the different evolutionary stages of the YSO population, map their spatial distribution, and reconstruct the star formation history in the region. To achieve this, we compiled a photometric catalogue spanning from optical to MIR wavelengths. The MIR photometric data from the IRAC instrument onboard the Spitzer Space Telescope, forms the foundation of our catalogue, as it is crucial for detecting the IR excess characteristic of YSOs. Through the process of data reduction and photometry applied to the retrieved NIR raw data from the NEWFIRM instrument, we complemented the existing MIR catalogue. Additionally, we incorporated optical and NIR photometric data from the catalogue described in the work by Mužić et al. (2022) and from public catalogues such as UKIDSS, 2MASS, and Pan-STARRS.

The YSO candidates were selected using two methods, referred to as Tier 1 and Tier 2 selection. The Tier 1 selection relies solely on sources detected in all four IRAC photometry bands. In this approach, YSO candidates are selected and classified based on the colour-colour diagrams outlined in the work of Gutermuth et al. (2009) *Phase 1* classification scheme. Additionally, where possible, we applied an improved version of the QSO cutoff criterion proposed by Bouy et al. (2009).

The Tier 2 selection process was designed to address the limited FoV and lower completeness magnitude of the IRAC3 and IRAC4 bands. It only utilized sources with photometric data in at least the H, J, K_S, IRAC1, and IRAC2 filters. The first phase of Tier 2 YSO identification and classification was carried out using customized constraints in the colour space, based on the positions of sources classified in Tier 1. As a result, the Tier 2 selection is biased by the Tier 1 criteria, and since it does not use IRAC3 and IRAC4 constraints, there is a higher number of contaminants that are more challenging to distinguish from genuine YSOs at shorter wavelengths. Tier 2, phase 1 YSO candidates proceed to a second phase, where we utilize VOSA (Bayo et al., 2008) to perform SED fitting. These SED fits allow for the construction of an HR diagram and, consequently, the estimation of ages. Sources younger than 10 Myr

and classified as Class II were retained. Additionally, Class I YSOs, which occupy distinct positions in colour-colour diagrams, were also retained, regardless of their position in the HR diagram. After the Tier 1 and Tier 2 selection process, we refined our sample of YSO candidates by removing sources located on the diffraction spikes of bright stars, that could distort their photometry readings. Additionally, we excluded sources identified in other studies as emission knots, despite our initial classification as potential YSOs.

We obtained a sample of 1,905 sources from the Tier 1 selection method and 671 from Tier 2, resulting in a catalogue of 2,576 YSO candidates. Of these, 1,972 are classified as Class II and 604 as Class I. The catalogue also includes 397 sources below the hydrogen-burning limit, assuming an age of 2 Myrs. Researchers have long investigated the formation of brown dwarfs, aiming to understand their origins. The identification of substellar objects in our YSO candidate catalogue supports the idea that brown dwarfs form through the same processes as stars. Additionally, our catalogue includes 33 Tier 1-selected Class I YSO candidates with masses below the hydrogen-burning limit. This provides an opportunity for future studies of these objects in the Rosette Nebula, as the early evolutionary stages of brown dwarfs, particularly their embedded Class 0/I phases, remain poorly understood (Morata et al., 2015; Barrado et al., 2018). It is also important to note that our coverage of the lower mass regime is incomplete, and we expect many more brown dwarfs in both Class I and Class II stages to exist.

We identified YSO candidates in all the young stellar groups highlighted by Phelps and Lada (1997); Roman-Zuniga (2006); Poulton et al. (2008); Cambrésy et al. (2013), with most located in NGC 2244 and the PL 04, PL 05, and REFL 08 complex. Comparing our findings with those of Broos et al. (2013), who also used MIR photometric data from IRAC and NIR photometric data from 2MASS and UKIDSS to identify YSOs, we recovered 457 out of the 586 YSO candidates they identified, yielding a high recovery rate of 78%. In contrast, other research, such as that by Cambrésy et al. (2013), used MIR data from WISE, which has lower spatial resolution, leading to issues in densely populated regions of the Rosette Nebula, where emissions from multiple sources blend, sources merge with nebular emissions, or simply nebular emissions that are not resolved by WISE but are resolved by IRAC. Despite these limitations, we were able to recover 241 of the 508 YSO candidates identified by Cambrésy et al. (2013), resulting in a recovery rate of 47%.

The OB star population in NGC 2244 drives the expansion of an HII region, which interacts with nearby molecular clouds, triggering star formation and leading to the formation of YSO populations. Our catalogue includes YSO candidates located in this interface region, including stellar groups like PL 01, PL 02, and PouC. This phenomenon has been observed in other studies as well, serving as evidence for triggered star formation, where the compression of gas by the expanding HII front leads to cluster formation (Phelps and Lada, 1997; Poulton et al., 2008; Schneider et al., 2010; Cambrésy et al., 2013). Additionally, YSO candidates found within cold molecular pillars appear to have formed due to the intense radiation from nearby OB stars. This radiation compresses the gas, further triggering star formation. However, in regions located farther from NGC 2244, beyond the interface region, star formation star formation cannot be fully explained by these triggering effects. Instead, the cloud's dynamical evolution plays a more significant role, with minimal influence from NGC 2244 (Heyer et al., 2006; Román-Zúñiga and Lada, 2008; Poulton et al., 2008; Schneider et al., 2010; Cambrésy et al., 2013). This indicates that while NGC 2244 has likely triggered star formation in PL 01, PL 02, and PouC, other areas, beyond the HII bubble, have formed independently of its influence. By integrating our YSO catalogue with the data from Mužić et al. (2022), we obtained the proper motions of YSO candidates relative to NGC 2244. The results show that YSOs in PL 01 and PL 02 are being pushed outward by the expanding HII front, lending further support to the triggered star formation hypothesis in the interface region.

We analyzed the distribution of YSOs at different evolutionary stages across various stellar structures within the complex and reconstructed the star formation history of the Rosette Nebula. The oldest stellar groups include NGC 2244 and others that likely formed around the same time or shortly after, such as the eastern part of the PL 04, PL 05, and REFL 08 complex, along with PouD, NGC 2237, REFL 09, and REFL 10. The younger regions, some of which are likely still forming stars, include areas occupied by PL 03, PL 06, PL 07, and the western part of the PL 04, PL 05, and REFL 08 complex. The interface region, containing stellar groups like PL 01, and the ridge formed by PL 02 and PouC, falls somewhere between these stages. These findings are consistent with previous studies by Heyer et al. (2006); Román-Zúñiga and Lada (2008); Poulton et al. (2008); Schneider et al. (2010); Cambrésy et al. (2013); Mužić et al. (2022).

While some stellar groups show evidence of star formation triggered by the HII front created by the OB population in the NGC 2244 cluster The presence of a YSO population beyond the interface region indicates that star formation in the Rosette Nebula occurs independently of NGC 2244 and its expanding HII bubble. Additionally, our age estimates for the stellar groups reveal variations that do not correlate with their positions within the Rosette Molecular Cloud or their distances from NGC 2244, indicating a dynamic evolution of the entire cloud.

References

Adobe Systems (2012). Adobe photoshop cs6. 23

Almendros-Abad, V., Mužić, K., Bouy, H., Bayo, A., Scholz, A., Peña Ramírez, K., Moitinho, A., Kubiak, K., Schöedel, R., Barač, R., Brčić, P., Ascenso, J., and Jayawardhana, R. (2023). Spectroscopic substellar initial mass function of NGC 2244. *Astronomy Astrophysics*, 677:A26. 6, 23, 24, 29, 71

Autry, R. G., Probst, R. G., Starr, B. M., Abdel-Gawad, K. M., Blakley, R. D., Daly, P. N., Dominguez, R., Hileman, E. A., Liang, M., Pearson, E. T., Shaw, R. A., and Tody, D. (2003). NEWFIRM: the widefield infrared imager for NOAO 4-m telescopes. In Iye, M. and Moorwood, A. F. M., editors, *Instrument Design and Performance for Optical/Infrared Ground-based Telescopes*, volume 4841, pages 525 – 539. International Society for Optics and Photonics, SPIE. 7, 9, 24

Balog, Z., Muzerolle, J., Rieke, G. H., Su, K. Y. L., Young, E. T., and Megeath, S. T. (2007). Spitzer/IRAC-MIPS Survey of NGC 2244: Protostellar Disk Survival in the Vicinity of Hot Stars. *Astrophysical Journal*, 660(2):1532–1540. 6, 71

Baraffe, I., Homeier, D., Allard, F., and Chabrier, G. (2015). New evolutionary models for pre-main sequence and main sequence low-mass stars down to the hydrogen-burning limit. *Astronomy Astrophysics*, 577:A42. 50, 51, 53, 70

Barrado, D., de Gregorio Monsalvo, I., Huélamo, N., Morales-Calderón, M., Bayo, A., Palau, A., Ruiz, M. T., Rivière-Marichalar, P., Bouy, H., Morata, Ó., Stauffer, J. R., Eiroa, C., and Noriega-Crespo, A. (2018). Early phases in the stellar and substellar formation and evolution. Infrared and submillimeter data in the Barnard 30 dark cloud. *Astronomy Astrophysics*, 612:A79. VI, 71, 74

Basu, S. and Vorobyov, E. I. (2012). A Hybrid Scenario for the Formation of Brown Dwarfs and Very Low Mass Stars. *Astrophysical Journal*, 750(1):30. 5

Bate, M. R. (2009). Stellar, brown dwarf and multiple star properties from hydrodynamical simulations of star cluster formation. *Monthly Notices of the Royal Astronomical Society*, 392(2):590–616. 5

Bayo, A., Rodrigo, C., Barrado Y Navascués, D., Solano, E., Gutiérrez, R., Morales-Calderón, M., and Allard, F. (2008). VOSA: virtual observatory SED analyzer. An application to the Collinder 69 open cluster. *Astronomy Astrophysics*, 492(1):277–287. V, 43, 47, 73

Bell, C. P. M., Naylor, T., Mayne, N. J., Jeffries, R. D., and Littlefair, S. P. (2013). Pre-main-sequence isochrones - II. Revising star and planet formation time-scales. *Monthly Notices of the Royal Astronomical Society*, 434(1):806–831. 5

Beroiz, M., Cabral, J., and Sanchez, B. (2020). Astroalign: A python module for astronomical image registration. *Astronomy and Computing*, 32:100384. 15

Bertin, E. (2006). Automatic Astrometric and Photometric Calibration with SCAMP. In Gabriel, C., Arviset, C., Ponz, D., and Enrique, S., editors, *Astronomical Data Analysis Software and Systems XV*, volume 351 of *Astronomical Society of the Pacific Conference Series*, page 112. 16

Bertin, E. (2011). Automated Morphometry with SExtractor and PSFEx. In Evans, I. N., Accomazzi, A., Mink, D. J., and Rots, A. H., editors, *Astronomical Data Analysis Software and Systems XX*, volume 442 of *Astronomical Society of the Pacific Conference Series*, page 435. 18

Bertin, E. and Arnouts, S. (1996). Sextractor: Software for source extraction. *Astronomy and Astrophysics Supplement*, 117:393–404. 16, 17

Bertin, E., Mellier, Y., Radovich, M., Missonnier, G., Didelon, P., and Morin, B. (2002). Astronomical data analysis software and systems xi. In *ASP Conf. Series*, volume 281, page 228. 16

Boulade, O., Vigroux, L. G., Charlot, X., Borgeaud, P., Carton, P.-H., de Kat, J., Rousse, J. Y., Mellier, Y., Gigan, P., Crampton, D., and Morbey, C. L. (1998). Megacam: the next-generation wide-field imaging camera for CFHT. In D'Odorico, S., editor, *Optical Astronomical Instrumentation*, volume 3355, pages 614 – 625. International Society for Optics and Photonics, SPIE. 24

Bouy, H., Huelamo, N., Barrado, D., Martin, E., Petr-Gotzens, M., Kolb, J., Marchetti, E., Morales-Calderon, M., Bayo, A., Artigau, □., Hartung, M., Marchis, F., Tamura, M., Sterzik, M., Köhler, R., Ivanov, V., and Nuernberger, D. (2009). A deep look into the core of young clusters. ii. lambda-orionis. *AA*, 504. V, 33, 36, 73

Bressan, A., Marigo, P., Girardi, L., Salasnich, B., Dal Cero, C., Rubele, S., and Nanni, A. (2012a). PARSEC: stellar tracks and isochrones with the PAdova and TRieste Stellar Evolution Code. *Monthly Notices of the Royal Astronomical Society*, 427(1):127–145. 39

Bressan, A., Marigo, P., Girardi, L., Salasnich, B., Dal Cero, C., Rubele, S., and Nanni, A. (2012b). PARSEC: stellar tracks and isochrones with the PAdova and TRieste Stellar Evolution Code. *Monthly Notices of the Royal Astronomical Society*, 427(1):127–145. 51, 53, 70

Broos, P. S., Getman, K. V., Povich, M. S., Feigelson, E. D., Townsley, L. K., Naylor, T., Kuhn, M. A., King, R. R., and Busk, H. A. (2013). Identifying Young Stars in Massive Star-forming Regions for the MYStIX Project. *Astrophysical Journal*, 209(2):32. VI, 57, 61, 62, 63, 64, 65, 69, 74

Caffau, E., Ludwig, H. G., Steffen, M., Freytag, B., and Bonifacio, P. (2011). Solar Chemical Abundances Determined with a CO5BOLD 3D Model Atmosphere. *Solar Physics*, 268(2):255–269. 48

Cambrésy, L., Marton, G., Feher, O., Tóth, L. V., and Schneider, N. (2013). Young stellar clusters in the Rosette molecular cloud. Arguments against triggered star formation. *Astronomy Astrophysics*, 557:A29. V, VI, VII, 5, 6, 40, 41, 42, 57, 58, 59, 60, 61, 62, 63, 64, 65, 66, 67, 68, 69, 73, 74, 75

Casali, M., Adamson, A., Oliveira, C., Almaini, O., Burch, K., Chuter, T., Elliot, J., Folger, M., Foucaud, S., Hambly, N., Hastie, M., Henry, D., Hirst, P., Irwin, M., Ives, D., Lawrence, A., Laidlaw, K., Lee, D., Lewis, J., and Woodward, B. (2007). The ukirt wide-field camera. *Astronomy and Astrophysics*, 467:777–784. 24

Casali, M., Ageorge, N., Alves de Oliveira, C., Biereichel, P., Delabre, B., Dorn, R., Esteves, R., Finger, G., Gojak, D., Huster, G., Jung, Y., Koch, F., Kiekebusch, M., Kissler-Patig, M., Le Louarn, M., Lizon,

J.-L., Mehrgan, L., Moorwood, A., Pirard, J., and Stegmeier, J. (2009). *HAWK-I and Infrared Imaging on the VLT*, pages 315–318. Springer. 24, 52

Chambers, K. C., Magnier, E. A., Metcalfe, N., Flewelling, H. A., Huber, M. E., Waters, C. Z., Denneau, L., Draper, P. W., Farrow, D., Finkbeiner, D. P., Holmberg, C., Koppenhoefer, J., Price, P. A., Rest, A., Saglia, R. P., Schlafly, E. F., Smartt, S. J., Sweeney, W., Wainscoat, R. J., Burgett, W. S., Chastel, S., Grav, T., Heasley, J. N., Hodapp, K. W., Jedicke, R., Kaiser, N., Kudritzki, R. P., Luppino, G. A., Lupton, R. H., Monet, D. G., Morgan, J. S., Onaka, P. M., Shiao, B., Stubbs, C. W., Tonry, J. L., White, R., Bañados, E., Bell, E. F., Bender, R., Bernard, E. J., Boegner, M., Boffi, F., Botticella, M. T., Calamida, A., Casertano, S., Chen, W. P., Chen, X., Cole, S., Deacon, N., Frenk, C., Fitzsimmons, A., Gezari, S., Gibbs, V., Goessl, C., Goggia, T., Gourgue, R., Goldman, B., Grant, P., Grebel, E. K., Hambly, N. C., Hasinger, G., Heavens, A. F., Heckman, T. M., Henderson, R., Henning, T., Holman, M., Hopp, U., Ip, W. H., Isani, S., Jackson, M., Keyes, C. D., Koekemoer, A. M., Kotak, R., Le, D., Liska, D., Long, K. S., Lucey, J. R., Liu, M., Martin, N. F., Masci, G., McLean, B., Mindel, E., Misra, P., Morganson, E., Murphy, D. N. A., Obaika, A., Narayan, G., Nieto-Santisteban, M. A., Norberg, P., Peacock, J. A., Pier, E. A., Postman, M., Primak, N., Rae, C., Rai, A., Riess, A., Riffeser, A., Rix, H. W., Röser, S., Russel, R., Rutz, L., Schilbach, E., Schultz, A. S. B., Scolnic, D., Strolger, L., Szalay, A., Seitz, S., Small, E., Smith, K. W., Soderblom, D. R., Taylor, P., Thomson, R., Taylor, A. N., Thakar, A. R., Thiel, J., Thilker, D., Unger, D., Urata, Y., Valenti, J., Wagner, J., Walder, T., Walter, F., Watters, S. P., Werner, S., Wood-Vasey, W. M., and Wyse, R. (2019). The pan-starrs1 surveys. 24

Cutri, R. M., Skrutskie, M. F., van Dyk, S., Beichman, C. A., Carpenter, J. M., Chester, T., Cambresy, L., Evans, T., Fowler, J., Gizis, J., Howard, E., Huchra, J., Jarrett, T., Kopan, E. L., Kirkpatrick, J. D., Light, R. M., Marsh, K. A., McCallon, H., Schneider, S., Stiening, R., Sykes, M., Weinberg, M., Wheaton, W. A., Wheelock, S., and Zacarias, N. (2003). VizieR Online Data Catalog: 2MASS All-Sky Catalog of Point Sources (Cutri+ 2003). *VizieR Online Data Catalog*, page II/246. 16, 24

Cutri, R. M., Wright, E. L., Conrow, T., Fowler, J. W., Eisenhardt, P. R. M., Grillmair, C., Kirkpatrick, J. D., Masci, F., McCallon, H. L., Wheelock, S. L., Fajardo-Acosta, S., Yan, L., Benford, D., Harbut, M., Jarrett, T., Lake, S., Leisawitz, D., Ressler, M. E., Stanford, S. A., Tsai, C. W., Liu, F., Helou, G., Mainzer, A., Gettngs, D., Gonzalez, A., Hoffman, D., Marsh, K. A., Padgett, D., Skrutskie, M. F., Beck, R., Papin, M., and Wittman, M. (2021). VizieR Online Data Catalog: AllWISE Data Release (Cutri+ 2013). *VizieR Online Data Catalog*, page II/328. 37, 64

Dale, J. E., Bonnell, I. A., and Whitworth, A. P. (2007). Ionization-induced star formation - I. The collect-and-collapse model. *Monthly Notices of the Royal Astronomical Society*, 375(4):1291–1298. 67

Dauphas, N. and Chaussidon, M. (2011). A perspective from extinct radionuclides on a young stellar object: The sun and its accretion disk. *Annual Review of Earth and Planetary Sciences - ANNU REV EARTH PLANET SCI*, 39. 4

Dent, W. R. F., Hovey, G. J., Dewdney, P. E., Burgess, T. A., Willis, A. G., Lightfoot, J. F., Jenness, T., Leech, J., Matthews, H. E., Heyer, M., and Poulton, C. J. (2009). A large-scale CO survey of the Rosette Molecular Cloud: assessing the effects of O stars on surrounding molecular gas. *Monthly Notices of the Royal Astronomical Society*, 395(4):1805–1821. 57

Dickinson, M. (2008). Newfirm linearity calibration and correction. Technical report, NOAO-DPP Doc. PL016, Tucson: NOAO. 11, 12

Dickinson, M. and Valdes, F. (2009). *A Guide to NEWFIRM Data Reduction with IRAF*. National Optical Astronomy Observatory. 11

Donley, J. L., Koekemoer, A. M., Brusa, M., Capak, P., Cardamone, C. N., Civano, F., Ilbert, O., Impey, C. D., Kartaltepe, J. S., Miyaji, T., Salvato, M., Sanders, D. B., Trump, J. R., and Zamorani, G. (2012). Identifying Luminous Active Galactic Nuclei in Deep Surveys: Revised IRAC Selection Criteria. *Astrophysical Journal*, 748(2):142. 37

Drążkowska, J., Bitsch, B., Lambrechts, M., Mulders, G. D., Harsono, D., Vazan, A., Liu, B., Ormel, C. W., Kretke, K., and Morbidelli, A. (2023). Planet Formation Theory in the Era of ALMA and Kepler: from Pebbles to Exoplanets. In Inutsuka, S., Aikawa, Y., Muto, T., Tomida, K., and Tamura, M., editors, *Protostars and Planets VII*, volume 534 of *Astronomical Society of the Pacific Conference Series*, page 717. 5

Elmegreen, B. G. (2011). On the Initial Conditions for Star Formation and the Initial Mass Function. *Astrophysical Journal*, 731(1):61. 5

Elston, R. (1998). FLAMINGOS: a multiobject near-IR spectrometer. In Fowler, A. M., editor, *Infrared Astronomical Instrumentation*, volume 3354 of *Society of Photo-Optical Instrumentation Engineers (SPIE) Conference Series*, pages 404–413. 24

Fazio, G. G., Hora, J. L., Allen, L. E., Ashby, M. L. N., Barmby, P., Deutsch, L. K., Huang, J. S., Kleiner, S., Marengo, M., Megeath, S. T., Melnick, G. J., Pahre, M. A., Patten, B. M., Polizotti, J., Smith, H. A., Taylor, R. S., Wang, Z., Willner, S. P., Hoffmann, W. F., Pipher, J. L., Forrest, W. J., McMurty, C. W., McCreight, C. R., McKelvey, M. E., McMurray, R. E., Koch, D. G., Moseley, S. H., Arendt, R. G., Mentzell, J. E., Marx, C. T., Losch, P., Mayman, P., Eichhorn, W., Krebs, D., Jhabvala, M., Gezari, D. Y., Fixsen, D. J., Flores, J., Shakoorzadeh, K., Jungo, R., Hakun, C., Workman, L., Karpati, G., Kichak, R., Whitley, R., Mann, S., Tollestrup, E. V., Eisenhardt, P., Stern, D., Gorjian, V., Bhattacharya, B., Carey, S., Nelson, B. O., Glaccum, W. J., Lacy, M., Lowrance, P. J., Laine, S., Reach, W. T., Stauffer, J. A., Surace, J. A., Wilson, G., Wright, E. L., Hoffman, A., Domingo, G., and Cohen, M. (2004). The Infrared Array Camera (IRAC) for the Spitzer Space Telescope. *Astrophysical Journal*, 154(1):10–17. 23

Gaia Collaboration (2021). Gaia Early Data Release 3. Summary of the contents and survey properties. *Astronomy Astrophysics*, 649:A1. 24, 41

Goodwin, S. P., Whitworth, A. P., and Ward-Thompson, D. (2004). An explanation for the unusual IMF in Taurus. *Astronomy Astrophysics*, 419:543–547. 5

Gritschneder, M., Burkert, A., Naab, T., and Walch, S. (2010). Detailed Numerical Simulations on the Formation of Pillars Around H II Regions. *Astrophysical Journal*, 723(2):971–984. 58

Gutermuth, R. A., Megeath, S. T., Myers, P. C., Allen, L. E., Pipher, J. L., and Fazio, G. G. (2009). A Spitzer Survey of Young Stellar Clusters Within One Kiloparsec of the Sun: Cluster Core Extraction and Basic Structural Analysis. *Astrophysical Journal*, 184(1):18–83. V, 33, 34, 37, 41, 42, 73

Gutermuth, R. A., Pipher, J. L., Megeath, S. T., Myers, P. C., Allen, L. E., and Allen, T. S. (2011). A Correlation between Surface Densities of Young Stellar Objects and Gas in Eight Nearby Molecular Clouds. *Astrophysical Journal*, 739(2):84. 2

Hennebelle, P. and Chabrier, G. (2008). Analytical Theory for the Initial Mass Function: CO Clumps and Prestellar Cores. *Astrophysical Journal*, 684(1):395–410. 5

Hensberge, H., Pavlovski, K., and Verschueren, W. (2000). The eclipsing binary V578 Mon in the Rosette nebula: age and distance to NGC 2244 using Fourier disentangled component spectra. *Astronomy Astrophysics*, 358:553–571. 5

Hester, J. J., Scowen, P. A., Sankrit, R., Lauer, T. R., Ajhar, E. A., Baum, W. A., Code, A., Currie, D. G., Danielson, G. E., Ewald, S. P., Faber, S. M., Grillmair, C. J., Groth, E. J., Holtzman, J. A., Hunter, D. A., Kristian, J., Light, R. M., Lynds, C. R., Monet, D. G., O'Neil, E. J., J., Shaya, E. J., Seidelmann, P. K., and Westphal, J. A. (1996). Hubble Space Telescope WFPC2 Imaging of M16: Photoevaporation and Emerging Young Stellar Objects. *The Astrophysical Journal*, 111:2349. 5

Heyer, M. H., Williams, J. P., and Brunt, C. M. (2006). Turbulent Gas Flows in the Rosette and G216-2.5 Molecular Clouds: Assessing Turbulent Fragmentation Descriptions of Star Formation. *Astrophysical Journal*, 643(2):956–964. VI, VII, 67, 69, 74, 75

Hodgkin, S., Irwin, M., Hewett, P., and Warren, S. (2008). The ukirt wide field camera zyjhk photometric system: calibration from 2mass. *Monthly Notices of the Royal Astronomical Society*, 394. 27

Honscheid, K. and DePoy, D. L. (2008). The dark energy camera (decam). 24

Ives, D. J., Tulloch, S., and Churchill, J. (1996). INT prime focus mosaic camera. In Anagnostopoulos, C. N., Blouke, M. M., and Lesser, M. P., editors, *Solid State Sensor Arrays and CCD Cameras*, volume 2654 of *Society of Photo-Optical Instrumentation Engineers (SPIE) Conference Series*, pages 266–276. 24

Kharchenko, N. V., Piskunov, A. E., Schilbach, E., Röser, S., and Scholz, R. D. (2013). Global survey of star clusters in the Milky Way. II. The catalogue of basic parameters. *Astronomy Astrophysics*, 558:A53. 5

Koenig, X. P. and Leisawitz, D. T. (2014). A classification scheme for young stellar objects using the wide-field infrared survey explorer allwise catalog: Revealing low-density star formation in the outer galaxy. *The Astrophysical Journal*, 791(2):131. 47

Koenig, X. P., Leisawitz, D. T., Benford, D. J., Rebull, L. M., Padgett, D. L., and Assef, R. J. (2012). Wide-field Infrared Survey Explorer Observations of the Evolution of Massive Star-forming Regions. *Astrophysical Journal*, 744(2):130. 64

Kratter, K. M., Matzner, C. D., Krumholz, M. R., and Klein, R. I. (2010). On the Role of Disks in the Formation of Stellar Systems: A Numerical Parameter Study of Rapid Accretion. *Astrophysical Journal*, 708(2):1585–1597. 5

Kron, R. G. (1980). Photometry of a complete sample of faint galaxies. *Astrophysical Journal*, 43:305–325. 29

Kuhn, M. A., Feigelson, E. D., Getman, K. V., Baddeley, A. J., Broos, P. S., Sills, A., Bate, M. R., Povich, M. S., Luhman, K. L., Busk, H. A., Naylor, T., and King, R. R. (2014). The Spatial Structure of Young Stellar Clusters. I. Subclusters. *Astrophysical Journal*, 787(2):107. 6

Kuhn, M. A., Getman, K. V., and Feigelson, E. D. (2015). The Spatial Structure of Young Stellar Clusters. II. Total Young Stellar Populations. *Astrophysical Journal*, 802(1):60. 6

Kuhn, M. A., Hillenbrand, L. A., Sills, A., Feigelson, E. D., and Getman, K. V. (2019). Kinematics in Young Star Clusters and Associations with Gaia DR2. *Astrophysical Journal*, 870(1):32. 5

Lada, C. J. and Lada, E. A. (2003). Embedded Clusters in Molecular Clouds. *Annual Review of Astronomy and Astrophysics*, 41:57–115. 1

Lawrence, A., Warren, S. J., Almaini, O., Edge, A. C., Hambly, N. C., Jameson, R. F., Lucas, P., Casali, M., Adamson, A., Dye, S., Emerson, J. P., Foucaud, S., Hewett, P., Hirst, P., Hodgkin, S. T., Irwin, M. J., Lodieu, N., McMahon, R. G., Simpson, C., Smail, I., Mortlock, D., and Folger, M. (2007). The UKIRT Infrared Deep Sky Survey (UKIDSS). *Monthly Notices of the Royal Astronomical Society*, 379(4):1599–1617. 24

Lim, B., Nazé, Y., Hong, J., Park, B.-G., Yun, H.-S., Yi, H.-W., Park, S., Hwang, N., and Lee, J.-E. (2021). A Kinematic Perspective on the Formation Process of the Stellar Groups in the Rosette Nebula. *The Astrophysical Journal*, 162(2):56. 5

Lomax, O., Whitworth, A. P., and Hubber, D. A. (2016). Forming isolated brown dwarfs by turbulent fragmentation. *Monthly Notices of the Royal Astronomical Society*, 458(2):1242–1252. 5

Lombardi, M., Alves, J., and Lada, C. J. (2011). 2MASS wide field extinction maps. IV. The Orion, Monoceros R2, Rosette, and Canis Major star forming regions. *Astronomy Astrophysics*, 535:A16. 5

Luhman, K. L. (2012). The formation and early evolution of low-mass stars and brown dwarfs. *Annual Review of Astronomy and Astrophysics*, 50(1):65–106. 71

Martins, F., Mahy, L., Hillier, D. J., and Rauw, G. (2012). A quantitative study of O stars in NGC 2244 and the Monoceros OB2 association. *Astronomy Astrophysics*, 538:A39. 5

Marton, G., Verebélyi, E., Kiss, C., and Smidla, J. (2013). Newly identified YSO candidates towards LDN 1188. *Astronomische Nachrichten*, 334(9):924. 64

Moorwood, A., Cuby, J.-G., and Lidman, C. (1998). Sofi sees first light at the ntt. *The Messenger*, 91:9–13. 24

Morata, O., Palau, A., González, R. F., de Gregorio-Monsalvo, I., Ribas, Á., Perger, M., Bouy, H., Barrado, D., Eiroa, C., Bayo, A., Huélamo, N., Morales-Calderón, M., and Rodríguez, L. F. (2015). First Detection of Thermal Radiojets in a Sample of Proto-brown Dwarf Candidates. *Astrophysical Journal*, 807(1):55. VI, 71, 74

Mužić, K., Almendros-Abad, V., Bouy, H., Kubiak, K., Peña Ramírez, K., Krone-Martins, A., Moitinho, A., and Conceição, M. (2022). Stellar population of the Rosette Nebula and NGC 2244. Application of the probabilistic random forest. *Astronomy Astrophysics*, 668:A19. V, VI, VII, 5, 6, 7, 23, 24, 29, 39, 40, 51, 52, 67, 68, 73, 74, 75

Mužić, K., Scholz, A., Peña Ramírez, K., Jayawardhana, R., Schödel, R., Geers, V. C., Cieza, L. A., and Bayo, A. (2019). Looking Deep into the Rosette Nebula's Heart: The (Sub)stellar Content of the Massive Young Cluster NGC 2244. *Astrophysical Journal*, 881(1):79. V, 1, 5, 6, 73

Ochsenbein, F. (1996). The vizier database of astronomical catalogues. 54

Ochsenbein, F., Bauer, P., and Marcout, J. (2000). The VizieR database of astronomical catalogues. *Astronomy Astrophysics*, 143:23–32. 54

Ogura, K. and Ishida, K. (1981). UBV photometry of NGC 2244. *Publications of the Astronomical Society of Japan*, 33:149–176. 5

Padoan, P. and Nordlund, Å. (2002). The Stellar Initial Mass Function from Turbulent Fragmentation. *Astrophysical Journal*, 576(2):870–879. 5

Padoan, P. and Nordlund, Å. (2004). The "Mysterious" Origin of Brown Dwarfs. *Astrophysical Journal*, 617(1):559–564. 5

Park, B.-G. and Sung, H. (2002). UBVI and Hα Photometry of the Young Open Cluster NGC 2244. *The Astrophysical Journal*, 123(2):892–904. 5

Pastorelli, G., Marigo, P., Girardi, L., Aringer, B., Chen, Y., Rubele, S., Trabucchi, M., Bladh, S., Boyer, M. L., Bressan, A., Dalcanton, J. J., Groenewegen, M. A. T., Lebzelter, T., Mowlavi, N., Chubb, K. L., Cioni, M.-R. L., de Grijs, R., Ivanov, V. D., Nanni, A., van Loon, J. T., and Zaggia, S. (2020). Constraining the thermally pulsing asymptotic giant branch phase with resolved stellar populations in the Large Magellanic Cloud. *Monthly Notices of the Royal Astronomical Society*, 498(3):3283–3301. 39

Perez, M. R., The, P. S., and Westerlund, B. E. (1987). On the distances to the young open clusters NGC 2244 and NGC 2264. *The Astronomical Society of the Pacific*, 99:1050–1066. 5

Phelps, R. L. and Lada, E. A. (1997). Spatial distribution of embedded clusters in the rosette molecular cloud: Implications for cluster formation. *The Astrophysical Journal*, 477(1):176. V, VI, 5, 7, 17, 40, 41, 57, 58, 59, 60, 67, 73, 74

Portegies Zwart, S. F., McMillan, S. L. W., and Gieles, M. (2010). Young Massive Star Clusters. *Annual Review of Astronomy and Astrophysics*, 48:431–493. 1

Poulton, C. J., Robitaille, T. P., Greaves, J. S., Bonnell, I. A., Williams, J. P., and Heyer, M. H. (2008). A Spitzer survey of young stellar objects in the Rosette Molecular Cloud. *Monthly Notices of the Royal Astronomical Society*, 384(4):1249–1262. V, VI, VII, 5, 6, 40, 41, 57, 58, 59, 60, 67, 69, 73, 74, 75

Povich, M. S., Kuhn, M. A., Getman, K. V., Busk, H. A., Feigelson, E. D., Broos, P. S., Townsley, L. K., King, R. R., and Naylor, T. (2013). The MYStIX Infrared-Excess Source Catalog. *Astrophysical Journal*, 209(2):31. 43, 63

Prialnik, D. (2000). *An Introduction to the Theory of Stellar Structure and Evolution*. Cambridge University Press. 1

Prisinzano, L., Damiani, F., Kalari, V., Jeffries, R., Bonito, R., Micela, G., Wright, N. J., Jackson, R. J., Tognelli, E., Guarcello, M. G., Vink, J. S., Klutsch, A., Jiménez-Esteban, F. M., Roccatagliata, V., Tautvaišienė, G., Gilmore, G., Randich, S., Alfaro, E. J., Flaccomio, E., Koposov, S., Lanzafame, A., Pancino, E., Bergemann, M., Carraro, G., Franciosini, E., Frasca, A., Gonneau, A., Hourihane, A., Jofré, P., Lewis, J., Magrini, L., Monaco, L., Morbidelli, L., Sacco, G. G., Worley, C. C., and Zaggia, S. (2019). The Gaia-ESO Survey: Age spread in the star forming region NGC 6530 from the HR diagram and gravity indicators. *Astronomy Astrophysics*, 623:A159. 51, 53, 70

Probst, R. G., Gaughan, N., Abraham, M., Andrew, J., Daly, P., Hileman, E., Hunten, M., Liang, M., Merrill, K. M., Repp, R., and Shaw, R. (2004). Program status of NEWFIRM, the wide-field infrared camera system for the NOAO 4-m telescopes. In Moorwood, A. F. M. and Iye, M., editors, *Ground-based Instrumentation for Astronomy*, volume 5492, pages 1716 – 1724. International Society for Optics and Photonics, SPIE. 7, 9

Probst, R. G., George, J. R., Daly, P. N., Don, K., and Ellis, M. (2008). First light with NEWFIRM. In McLean, I. S. and Casali, M. M., editors, *Ground-based and Airborne Instrumentation for Astronomy II*, volume 7014, page 70142S. International Society for Optics and Photonics, SPIE. 7, 9

Reid, I. Neilland Hawley, S. L. (2005). *The structure, formation and evolution of low-mass stars and brown dwarfs*, chapter 6. Springer Berlin Heidelberg, Berlin, Heidelberg. 4

Reipurth, B. and Clarke, C. (2001). The Formation of Brown Dwarfs as Ejected Stellar Embryos. *The Astrophysical Journal*, 122(1):432–439. 5

Rodrigo, C. and Solano, E. (2020). The SVO Filter Profile Service. In *XIV.0 Scientific Meeting (virtual) of the Spanish Astronomical Society*, page 182. 48

Rodrigo, C., Solano, E., and Bayo, A. (2012). SVO Filter Profile Service Version 1.0. IVOA Working Draft 15 October 2012. 48

Román-Zúñiga, C. G. and Lada, E. A. (2008). Star Formation in the Rosette Complex. In Reipurth, B., editor, *Handbook of Star Forming Regions, Volume I*, volume 4, page 928. Astronomical Society of the Pacific. VI, VII, 6, 67, 69, 74, 75

Roman-Zuniga, C. G. (2006). *Near infrared study of the star-forming properties of the Rosette Complex*. PhD thesis, University of Florida. V, VI, 5, 40, 41, 57, 58, 59, 60, 73, 74

Schneider, N., Motte, F., Bontemps, S., Hennemann, M., di Francesco, J., André, P., Zavagno, A., Csengeri, T., Men'shchikov, A., Abergel, A., Baluteau, J. P., Bernard, J. P., Cox, P., Didelon, P., di Giorgio, A. M., Gastaud, R., Griffin, M., Hargrave, P., Hill, T., Huang, M., Kirk, J., Könyves, V., Leeks, S., Li, J. Z., Marston, A., Martin, P., Minier, V., Molinari, S., Olofsson, G., Panuzzo, P., Persi, P., Pezzuto, S., Roussel, H., Russeil, D., Sadavoy, S., Saraceno, P., Sauvage, M., Sibthorpe, B., Spinoglio, L., Testi, L., Teyssier, D., Vavrek, R., Ward-Thompson, D., White, G., Wilson, C. D., and Woodcraft, A. (2010). The Herschel view of star formation in the Rosette molecular cloud under the influence of NGC 2244. *Astronomy Astrophysics*, 518:L83. VI, VII, 67, 69, 74, 75

Schulz, N. S. (2005). *From Dust To Stars: Studies of the Formation and Early Evolution of Stars*. Springer. 1, 3

Shaw, R. A., editor (2015). *NOAO Data Handbook*. National Optical Astronomy Observatory, Tucson, 2.2 edition. 9, 11, 12, 14

Stamatellos, D. and Whitworth, A. P. (2009). The properties of brown dwarfs and low-mass hydrogen-burning stars formed by disc fragmentation. *Monthly Notices of the Royal Astronomical Society*, 392(1):413–427. 5

Stamer, T. and Inutsuka, S.-i. (2019). Constraints on the formation of brown dwarfs by turbulent compression. *Monthly Notices of the Royal Astronomical Society*, 488(2):2644–2649. 4

Stern, D., Eisenhardt, P., Gorjian, V., Kochanek, C. S., Caldwell, N., Eisenstein, D., Brodwin, M., Brown, M. J. I., Cool, R., Dey, A., Green, P., Jannuzi, B. T., Murray, S. S., Pahre, M. A., and Willner, S. P. (2005). Mid-Infrared Selection of Active Galaxies. *Astrophysical Journal*, 631(1):163–168. 33, 34, 37

Suto, H., Mizutani, K., and Maihara, T. (1992). 3.3 micrometer Spectra of Four IRAS Sources. *The Astrophysical Journal*, 103:927. 16

Tenorio-Tagle, G. (1979). The gas dynamics of H II regions. I. The champagne model. *Astronomy Astrophysics*, 71:59–65. 1

UKIDSS Consortium (2012). VizieR Online Data Catalog: UKIDSS-DR6 Galactic Plane Survey (Lucas+ 2012). *VizieR Online Data Catalog*, page II/316. 26

Vorobyov, E. I. (2013). Formation of giant planets and brown dwarfs on wide orbits. *Astronomy Astrophysics*, 552:A129. 5

Wang, S. and Chen, X. (2019). The Optical to Mid-infrared Extinction Law Based on the APOGEE, Gaia DR2, Pan-STARRS1, SDSS, APASS, 2MASS, and WISE Surveys. *Astrophysical Journal*, 877(2):116. 33, 49, 53

Werner, M. W., Roellig, T. L., Low, F. J., Rieke, G. H., Rieke, M., Hoffmann, W. F., Young, E., Houck, J. R., Brandl, B., Fazio, G. G., Hora, J. L., Gehrz, R. D., Helou, G., Soifer, B. T., Stauffer, J., Keene, J., Eisenhardt, P., Gallagher, D., Gautier, T. N., Irace, W., Lawrence, C. R., Simmons, L., Van Cleve, J. E., Jura, M., Wright, E. L., and Cruikshank, D. P. (2004). The Spitzer Space Telescope Mission. *Astrophysical Journal*, 154(1):1–9. 23

Whitworth, A. P. and Zinnecker, H. (2004). The formation of free-floating brown dwarves and planetary-mass objects by photo-erosion of prestellar cores. *Astronomy Astrophysics*, 427:299–306. 5

Wilson, T. L. and Johnston, K. J., editors (1994). *The Structure and Content of Molecular Clouds 25 Years of Molecular Radioastronomy: Proceedings of a Conference Held at Schloss Ringberg, Tegernsee, Germany 14–16 April 1993*, volume 439 of *Lecture Notes in Physics*, Berlin, Heidelberg. Springer Berlin Heidelberg. 1

Wu, X.-B., Hao, G., Jia, Z., Zhang, Y., and Peng, N. (2012). Sdss quasars in the wise preliminary data release and quasar candidate selection with optical/infrared colors. *The Astronomical Journal*, 144(2):49. 37

Ybarra, J. E., Lada, E. A., Balog, Z., Fleming, S. W., and Phelps, R. L. (2010). Spitzer and near-infrared observations of a new bipolar protostellar outflow in the rosette molecular cloud. *The Astrophysical Journal*, 714(1):469. 16, 55

York, D. G. (2003). Interstellar matter. In Meyers, R. A., editor, *Encyclopedia of Physical Science and Technology (Third Edition)*, pages 45–54. Academic Press, New York, third edition edition. 1

Appendix A

In Figure A.1, we display the YSO candidates that were excluded during the manual cleaning process (Section 4.4) due to the likelihood that their photometry was distorted by their location on the diffraction spikes of bright stars. The YSO candidates presented in both Figure A.1 and Figure 4.25 represent all the sources removed due to contamination from diffraction spikes.

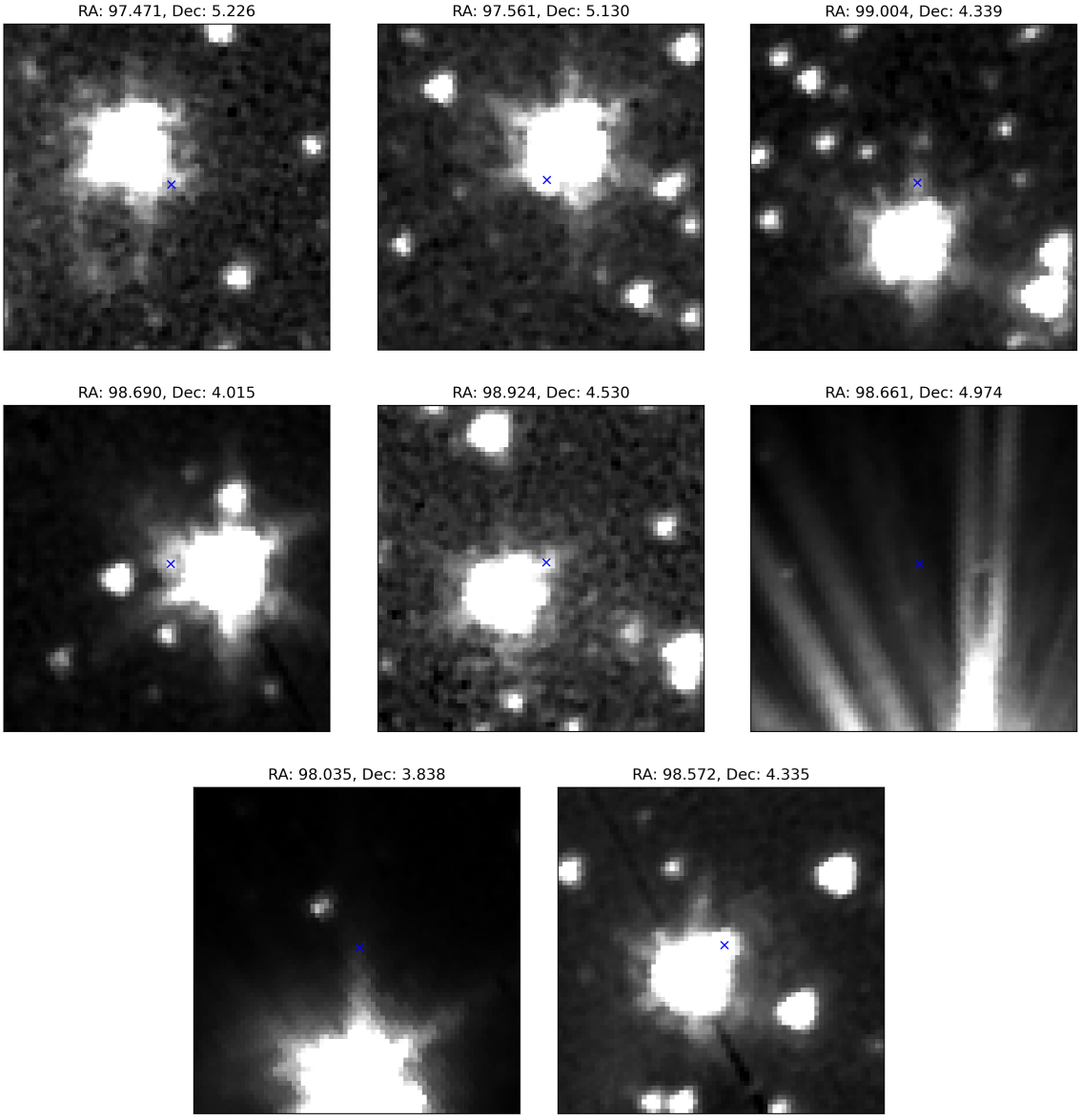

Figure A.1: IRAC1 images displaying the position of the contaminated YSO candidate (blue cross).